



# **BaTiO<sub>3</sub>-BiFeO<sub>3</sub> based lead-free ceramics for actuator applications**

By

SHUNSUKE MURAKAMI

Registration No: 150246772

Supervisors; Prof Ian M Reaney, Prof Derek C. Sinclair

A thesis submitted in partial fulfilment of the requirements for the degree

of

Doctor of Philosophy

Department of Materials Science and Engineering

Faculty of Engineering

The University of Sheffield

July 2018

## Acknowledgements

I would like to acknowledge my supervisor Prof. Ian M Reaney for his continuous support. He gave me the opportunity to study here and has kept guiding me in the appropriate direction in this project. Without his academic suggestions and experienced hypotheses, I would not be able to complete this project. I am also thankful to my co-supervisor Prof. Derek. C. Sinclair especially for his warm guidance on the analysis of electric properties of ceramics and all the fruitful discussions through this project. I am deeply grateful to Dr. Antonio Feteira at Sheffield Hallam University for giving me access to his ferroelectric testing system. The strain data measured were crucial for this project. I am really grateful to Prof. Xiaoli Tan and Zhongming Fan at Iowa State University in USA for cooperating TEM observation of my samples.

I would like to extend my gratitude to Dr. Dawei Wang for his help on ceramic processing work. His previous work on  $\text{BaTiO}_3\text{-BiFeO}_3$  based ceramics facilitated a rapid introduction to the topic. Also, I would like to Dr Amir Khesro for fruitful discussion about piezoelectricity. I would like to express my gratitude to Dr. Ali Mostaed for TEM observations. I would also like to thank Mr. Nihal Thafeem Ahmed Faheem Ahmed with whom I worked on the investigation on  $\text{BiScO}_3\text{-BaTiO}_3\text{-BiFeO}_3$  ceramics during his MSc. I am grateful to all the postdocs and PhD students in our group who helped me in everyday work; many discussions with them greatly contribute to this project. Thanks to Dr. Nik Maclaren for his daily efforts managing X-ray diffraction machines and guidance about Rietveld analysis.

I would like to express my sincere thanks to Prof. Oto at Chiba University and Dr. Miura from Canon Inc. in Japan for giving me this precious opportunity to study in the UK. This experience has made a great difference to my career as an engineer. Finally, I would like to thank my wife Eiko for coming to the UK together and her continuous support in our daily life and always enjoying our time in the UK.

## Publications:

**S. Murakami**, D. Wang, A. Mostaed, A. Khesro, A. Feteira, D. C. Sinclair<sup>1</sup>, Z. Fan, X. Tan and I. M. Reaney, “High strain (0.4%) Bi(Mg<sub>2/3</sub>Nb<sub>1/3</sub>)O<sub>3</sub>-BaTiO<sub>3</sub>-BiFeO<sub>3</sub> lead-free piezoelectric ceramics and multilayers”, *J. Am. Ceram. Soc.*, **101**, 5428-5442, (2018).

**S. Murakami**, N. T. A. Faheem Ahmed, D. Wang<sup>1</sup>, A. Feteira, D. C. Sinclair, and I. M. Reaney, “Optimising dopants and properties in BiMeO<sub>3</sub> (Me = Al, Ga, Sc, Y, Mg<sub>2/3</sub>Nb<sub>1/3</sub>, Zn<sub>2/3</sub>Nb<sub>1/3</sub>, Zn<sub>1/2</sub>Ti<sub>1/2</sub>) doped lead-free BaTiO<sub>3</sub>-BiFeO<sub>3</sub> based ceramics for actuator applications”, *J. Euro. Ceram. Soc.*, **38**, 4220-4231, (2018).

U. Obilora, C. Pascual-Gonzalez, **S. Murakami**, I. M. Reaney, A. Feteira, “Study of the temperature dependence of the giant electric field-induced strain in Nb-doped BNT-BT-BKT piezoceramics”, *Mater. Res. Bull.*, **97**, 385-392, (2018)

D. Wang, Z. Fan, D. Zhou, A. Khesro, **S. Murakami**, A. Feteira, Q. Zhao, X. Tan, and I. M. Reaney, “Bismuth ferrite-based lead-free ceramics and multilayers with high recoverable energy density”, *J. Mater. Chem. C*, **6**, 4133-4144, (2018).

C. Pascual-Gonzalez, G. Schileo, **S. Murakami**, A. Khesro, D. Wang, I. M. Reaney, and A. Feteira, “Continuously controllable optical band gap in orthorhombic ferroelectric KNbO<sub>3</sub>-BiFeO<sub>3</sub> ceramics”, *Appl. Phys. Lett.*, **110**, 17902, (2017).

D. Wang, A. Khesro, **S. Murakami**, A. Feteira, Q. Zhao, and I. M. Reaney, “Temperature dependent, large electromechanical strain in Nd-doped BiFeO<sub>3</sub>-BaTiO<sub>3</sub> lead-free ceramics”, *J. Euro. Ceram. Soc.*, **37**, [4], 1857-1860, (2017).

## Conference Presentations:

“Lead-free BaTiO<sub>3</sub>-BiFeO<sub>3</sub> based piezoelectric ceramics”, Sustainable Functional Materials 2016, Scarborough, UK, April 2016.

“Bi(Mg<sub>2/3</sub>Nb<sub>1/3</sub>)O<sub>3</sub>-BaTiO<sub>3</sub>-BiFeO<sub>3</sub> PbO-free piezoelectric ceramics”, 2017 IEEE International Symposium on Applications of Ferroelectrics (ISAF), Atlanta, USA, May 2017.

“High strain (0.4%) Bi(Mg<sub>2/3</sub>Nb<sub>1/3</sub>)O<sub>3</sub>-BaTiO<sub>3</sub>-BiFeO<sub>3</sub> lead-free piezoelectrics”, 2018 Conference on Electronic and Advanced Materials, Orlando, USA, January 2018.

“High strain (0.4%) Bi(Mg<sub>2/3</sub>Nb<sub>1/3</sub>)O<sub>3</sub>-BaTiO<sub>3</sub>-BiFeO<sub>3</sub> lead-free piezoelectrics”, 1-DRAC, Manchester, UK, April 2018.

“Predicting optimised piezoelectric properties in BiMeO<sub>3</sub> (Me = Al, Ga, Sc, Y, Mg<sub>2/3</sub>Nb<sub>1/3</sub>, Zn<sub>2/3</sub>Nb<sub>1/3</sub>, Zn<sub>1/2</sub>Ti<sub>1/2</sub>) doped lead-free BaTiO<sub>3</sub>-BiFeO<sub>3</sub> based ceramics”, Sustainable Functional

Materials 2018, Weston-Super-Mare, UK, May 2018.

“Optimising dopants and properties in  $\text{BiMeO}_3$ -doped ( $Me = \text{Al, Ga, Sc, Y, Mg}_{2/3}\text{Nb}_{1/3}, \text{Zn}_{2/3}\text{Nb}_{1/3}, \text{Zn}_{1/2}\text{Ti}_{1/2}$ ), lead-free  $\text{BaTiO}_3$ - $\text{BiFeO}_3$  based piezoelectrics”, Electroceramics XVI, Hasselt, Belgium, July 2018.

“Optimising dopants and properties in  $\text{BiMeO}_3$ -doped ( $Me = \text{Al, Ga, Sc, Y, Mg}_{2/3}\text{Nb}_{1/3}, \text{Zn}_{2/3}\text{Nb}_{1/3}, \text{Zn}_{1/2}\text{Ti}_{1/2}$ ), lead-free  $\text{BaTiO}_3$ - $\text{BiFeO}_3$  based piezoelectrics”, UK Ceramics Talent, London, UK, October 2018. (Invited)

## Abstract

A crystallochemical framework is proposed based on electronegativity difference ( $e_n$ ) and tolerance factor ( $t$ ) for  $\text{BiMeO}_3$  dopants to optimise the piezoelectric and electrostrictive response in  $\text{BaTiO}_3$ - $\text{BiFeO}_3$  based ceramics. Compositions in the series  $0.05\text{Bi}(\text{Me})\text{O}_3$ - $0.25\text{BaTiO}_3$ - $0.70\text{BiFeO}_3$  ( $\text{BMe-BT-BF}$ ,  $\text{Me}$ : Y,  $\text{Sc}_{1/2}\text{Y}_{1/2}$ ,  $\text{Mg}_{2/3}\text{Nb}_{1/3}$ , Sc,  $\text{Zn}_{2/3}\text{Nb}_{1/3}$ ,  $\text{Zn}_{1/2}\text{Ti}_{1/2}$ , Ga, and Al) were fabricated using solid state synthesis. Scanning electron microscopy (SEM) and X-ray diffraction (XRD) revealed that only  $\text{Bi}(\text{Mg}_{2/3}\text{Nb}_{1/3})\text{O}_3$  and  $\text{BiScO}_3$  dopants, which lie in a narrow range of  $e_n$  vs.  $t$ , form homogeneous ceramics, free from secondary phases reflected in their superior piezoelectric coefficients ( $d_{33} \sim 145$  pC/N).

The promising initial properties of  $\text{Bi}(\text{Mg}_{2/3}\text{Nb}_{1/3})\text{O}_3$  and  $\text{BiScO}_3$  doped compositions prompted further studies on  $0.05\text{Bi}(\text{Mg}_{2/3}\text{Nb}_{1/3})\text{O}_3$ - $(0.95-x)\text{BaTiO}_3$ - $(x)\text{BiFeO}_3$  ( $\text{BMN-BT-BF}$ ,  $x = 0.55, 0.60, 0.63, 0.65, 0.70$ , and  $0.75$ ) and  $0.05\text{BiScO}_3$ - $(0.95-x)\text{BaTiO}_3$ - $(x)\text{BiFeO}_3$  ( $\text{BS-BT-BF}$ ,  $x = 0.55, 0.60, 0.625, 0.65$ , and  $0.70$ ) ceramics. For  $\text{Me} = \text{Mg}_{2/3}\text{Nb}_{1/3}$ , SEM revealed a homogeneous microstructure for  $x < 0.75$ . XRD suggested a gradual structural transition from pseudocubic to rhombohedral for  $0.63 < x < 0.70$ , characterised by the coexistence of phases. The temperature dependence of relative permittivity, polarisation-electric field hysteresis loops, bipolar strain-electric field curves revealed that  $\text{BMN-BT-BF}$  transformed from relaxor-like to ferroelectric behaviour with an increase in  $x$  and the largest effective piezoelectric coefficient ( $d_{33}^*$ ) was 544 pm/V at 5 kV/mm for  $x = 0.63$  at 5 kV/mm, at the point of crossover from relaxor to ferroelectric which facilitates a macroscopic field induced transition to a ferroelectric state. For  $\text{Me} = \text{Sc}$ , the trends were similar but Sc-doped samples retained ferroelectric behavior to slightly lower values of  $x$  than  $\text{Mg}_{2/3}\text{Nb}_{1/3}$  samples.

The potential for  $\text{BMN-BT-BF}$  compositions to be used as high strain actuators is demonstrated by the fabrication of a prototype multilayer which achieved similar % strain to monolithic ceramics and up to 3  $\mu\text{m}$  displacement with good temperature stability up to 150°C.

# Contents

<b>Chapter 1: Introduction</b> .....	1
<b>Chapter 2: Literature Review</b> .....	2
<b>2.1 Basic theory</b> .....	3
<b>2.1.1 Dielectrics</b> .....	3
<b>2.1.2 Piezoelectrics</b> .....	7
<b>2.1.3 Ferroelectrics</b> .....	9
<b>2.1.4 Relaxors</b> .....	14
<b>2.1.5 Morphotropic phase boundary (MPB) and electromechanical properties</b> .....	16
<b>2.2 Piezoelectric materials</b> .....	19
<b>2.2.2 Lead-free piezoelectric materials</b> .....	20
<b>2.2.3 BaTiO<sub>3</sub>-BiFeO<sub>3</sub> based piezoelectric materials</b> .....	21
<b>2.2.4 Dopants in BaTiO<sub>3</sub>-BiFeO<sub>3</sub> based materials</b> .....	22
<b>Chapter 3: Experimental techniques</b> .....	24
<b>3.1 Particle size analysis</b> .....	24
<b>3.1.1 Archimedes' density</b> .....	25
<b>3.1.2 Theoretical density</b> .....	25
<b>3.1.3 Relative density</b> .....	25
<b>3.3 Structural and microstructural analysis</b> .....	26
<b>3.3.1 X-ray diffraction (XRD)</b> .....	26
<b>3.3.2 Scanning electron microscopy (SEM)</b> .....	27
<b>3.3.3 Transmission electron microscope (TEM)</b> .....	28
<b>3.4 Piezoelectric and Polarization measurements</b> .....	29
<b>3.4.1 Low field measurements (Resonance method)</b> .....	29
<b>3.4.2 Low field measurements (Berlincourt method)</b> .....	32
<b>3.4.3 High field method</b> .....	32
<b>3.5 Electrical measurements</b> .....	33
<b>3.5.1 Relative permittivity (<math>\epsilon_r</math>) and dielectric loss (<math>\tan\delta</math>)</b> .....	33
<b>3.5.2 Impedance spectroscopy</b> .....	35

<b>Chapter 4: Processing of Materials</b> .....	39
<b>4.1 Introduction</b> .....	39
<b>4.2 Raw materials</b> .....	39
<b>4.2.1 Raw materials</b> .....	39
<b>4.2.2 Drying of raw materials</b> .....	40
<b>4.2.3 Phase analysis of raw materials</b> .....	41
<b>4.2.4 Particle size analysis of raw materials</b> .....	42
<b>4.3 Ceramic processing</b> .....	43
<b>4.3.1 Powder weighing</b> .....	43
<b>4.3.2 Mixing and milling of powder</b> .....	43
<b>4.3.3 Calcination</b> .....	45
<b>4.3.4 Pressing into green compact</b> .....	47
<b>4.3.5 Sintering</b> .....	47
<b>Chapter 5: Optimising dopants in BiMeO<sub>3</sub> doped lead-free BaTiO<sub>3</sub>-BiFeO<sub>3</sub> based ceramics</b> .....	51
<b>5.1 Introduction</b> .....	51
<b>5.2 Results and Discussion</b> .....	51
<b>5.2.1 XRD Analysis and microstructure</b> .....	51
<b>5.2.2 Temperature dependence of <math>\epsilon_r</math> and <math>\tan\delta</math></b> .....	58
<b>5.2.3 Ferroelectric and Piezoelectric properties</b> .....	59
<b>5.2.4 Crystallochemical Considerations</b> .....	61
<b>5.3 Conclusion</b> .....	62
<b>Chapter 6: 0.05Bi(Mg<sub>2/3</sub>Nb<sub>1/3</sub>)O<sub>3</sub>-(0.95-x)BaTiO<sub>3</sub>-(x)BiFeO<sub>3</sub> based ceramics</b> .....	63
<b>6.1 Introduction</b> .....	63
<b>6.2 Results and discussion</b> .....	63
<b>6.2.1 XRD Analysis</b> .....	63
<b>6.2.2 Microstructure</b> .....	65
<b>6.2.3 Temperature dependence of relative permittivity (<math>\epsilon_r</math>) and <math>\tan\delta</math></b> .....	73
<b>6.2.4 Ferroelectric and Piezoelectric properties</b> .....	76
<b>6.2.5 Effect of quenching on 0.05Bi(Mg<sub>2/3</sub>Nb<sub>1/3</sub>)O<sub>3</sub>-0.20BaTiO<sub>3</sub>-0.75BiFeO<sub>3</sub></b> .....	79
<b>6.3 Conclusions</b> .....	82

<b>Chapter 7: <math>0.05\text{BiScO}_3-(0.95-x)\text{BaTiO}_3-(x)\text{BiFeO}_3</math> based ceramics</b> .....	83
<b>7.1 Introduction</b> .....	83
<b>7.2 Results and Discussion</b> .....	83
<b>7.2.1 XRD Analysis</b> .....	83
<b>7.2.2 Microstructure</b> .....	84
<b>7.2.3 Temperature dependence of relative permittivity (<math>\epsilon_r</math>) and <math>\tan\delta</math></b> .....	89
<b>7.2.4 Ferroelectric and piezoelectric properties</b> .....	91
<b>7.3 Conclusion</b> .....	96
<b>Chapter 8: Multilayer Actuator (MLA) for <math>0.05\text{Bi}(\text{Mg}_{2/3}\text{Nb}_{1/3})\text{O}_3-0.63\text{BaTiO}_3-0.32\text{BiFeO}_3</math></b> .....	98
<b>8.1 Introduction</b> .....	98
<b>8.2 MLA processing</b> .....	99
<b>8.2.1 Slurry formation</b> .....	99
<b>8.2.2 Tape Casting</b> .....	100
<b>8.2.3. Electrode printing</b> .....	100
<b>8.2.4 Cutting and lamination</b> .....	101
<b>8.2.5 Binder burning out and sintering</b> .....	102
<b>8.2.6 Termination of electrodes</b> .....	102
<b>8.3 Results and Discussion</b> .....	102
<b>8.4 Conclusions</b> .....	105
<b>Chapter 9: Conclusions and Future work</b> .....	107
<b>9.1 Conclusions</b> .....	107
<b>9.1.1 Optimising properties in <math>\text{BiMeO}_3</math> doped lead-free <math>\text{BaTiO}_3\text{-BiFeO}_3</math> based ceramics</b> .....	107
<b>9.1.2 <math>0.05\text{Bi}(\text{Mg}_{2/3}\text{Nb}_{1/3})\text{O}_3-(0.95-x)\text{BaTiO}_3-(x)\text{BiFeO}_3</math> based ceramics</b> .....	107
<b>9.1.3 <math>0.05\text{BiScO}_3-(0.95-x)\text{BaTiO}_3-(x)\text{BiFeO}_3</math> based ceramics</b> .....	108
<b>9.1.4 Multilayer actuator (MLA) for <math>0.05\text{Bi}(\text{Mg}_{2/3}\text{Nb}_{1/3})\text{O}_3-0.63\text{BaTiO}_3-0.32\text{BiFeO}_3</math></b> .....	108
<b>9.2 Future work</b> .....	108
<b>References</b> .....	111

## List of figures and tables

Fig. 2. 1 .....	4
Fig. 2. 2 .....	4
Fig. 2. 3 .....	5
Fig. 2. 4 .....	6
Fig. 2. 5 .....	7
Fig. 2. 6 .....	8
Fig. 2. 7 .....	9
Fig. 2. 8 .....	10
Fig. 2. 9 .....	10
Fig. 2. 10 .....	13
Fig. 2. 11 .....	14
Fig. 2. 12 .....	15
Fig. 2. 13 .....	16
Fig. 2. 14 .....	17
Fig. 2. 15 .....	18
Fig. 2. 16 .....	18
Fig. 2. 17 .....	19
Fig. 3. 1 .....	24
Fig. 3. 2 .....	28
Fig. 3. 3 .....	29
Fig. 3. 4 .....	30
Fig. 3. 5 .....	30
Fig. 3. 6 .....	31
Fig. 3. 7 .....	32
Fig. 3. 8 .....	34
Fig. 3. 9 .....	36
Fig. 3. 10 .....	37
Fig. 4. 1 .....	41
Fig. 4. 2 .....	42
Fig. 4. 3 .....	43
Fig. 4. 4 .....	44
Fig. 4. 5 .....	45
Fig. 4. 6 .....	46
Fig. 4. 7 .....	48
Fig. 4. 8 .....	48
Fig. 5. 1 .....	52
Fig. 5. 2 .....	54
Fig. 5. 3 .....	55
Fig. 5. 4 .....	57

Fig. 5. 5 .....	59
Fig. 5. 6 .....	60
Fig. 5. 7 .....	61
Fig. 6. 1 .....	64
Fig. 6. 2 .....	66
Fig. 6. 3 .....	67
Fig. 6. 4 .....	68
Fig. 6. 5 .....	70
Fig. 6. 6 .....	72
Fig. 6. 7 .....	72
Fig. 6. 8 .....	74
Fig. 6. 9 .....	75
Fig. 6. 10 .....	76
Fig. 6. 11 .....	77
Fig. 6. 12 .....	78
Fig. 6. 13 .....	79
Fig. 6. 14 .....	80
Fig. 6. 15 .....	80
Fig. 7. 1 .....	84
Fig. 7. 2 .....	85
Fig. 7. 3 .....	87
Fig. 7. 4 .....	89
Fig. 7. 5 .....	90
Fig. 7. 6 .....	91
Fig. 7. 7 .....	92
Fig. 7. 8 .....	92
Fig. 7. 9 .....	93
Fig. 7. 10 .....	94
Fig. 7. 11 .....	95
Fig. 7. 12 .....	95
Fig. 7. 13 .....	96
Fig. 7. 14 .....	96
Fig. 8. 1 .....	98
Fig. 8. 2 .....	99
Fig. 8. 3 .....	100
Fig. 8. 4 .....	101
Fig. 8. 5 .....	101
Fig. 8. 6 .....	102
Fig. 8. 7 .....	103
Fig. 8. 8 .....	104
Fig. 8. 9 .....	104

Fig. 8. 10.....	105
Fig. 8. 11.....	105
Table 4. 1.....	39
Table 4. 2.....	40
Table 4. 3.....	41
Table 4. 4.....	46
Table 4. 5.....	47
Table 4. 6.....	50
Table 5. 1.....	56
Table 5. 2.....	58
Table 6. 1.....	65
Table 6. 2.....	71
Table 6. 3.....	78
Table 7. 1.....	84
Table 7. 2.....	88
Table 8. 1.....	100

## Chapter 1: Introduction

Piezoelectric materials convert electrical energy to mechanical strain and vice versa and have applications such as actuators, sensors, generators and acoustic transducers. Recently, piezoelectric applications have emerged for extreme environment within the high temperature ( $>200^{\circ}\text{C}$ ) regions of automotive engines, oil well drilling and aerospace. Consequently, there has been significant interest to improve the temperature range and performance of piezoelectrics and an acceptance that compositions with higher Curie temperature ( $T_C$ ) than  $\text{Pb}(\text{Zr},\text{Ti})\text{O}_3$  (PZT) ( $250\text{-}320^{\circ}\text{C}$ ) are required to achieve this ambition<sup>1, 2</sup>

PZT has been widely applied in piezoelectric devices because of the superior piezoelectric performances over the past few decades.<sup>3</sup> However, not only are there limitations in its operating temperature,<sup>1, 2</sup> but there are also environment and health issues due to the toxicity of lead.<sup>4, 5</sup> Rödel *et al.*<sup>6</sup> summarized how lead affects the human body, noting that  $\text{PbO}$  is less toxic than metallic  $\text{Pb}$ . The majority of potential problems for PZT are linked not to the stable room temperature compound but during production when lead oxide is vaporized at high temperature.<sup>7-9</sup> To restrict using hazardous materials including lead in electronic devices, the Restriction of Hazardous Substances Directive (RoHS) was adopted by the European Union in 2003<sup>10</sup>, which led to intensive worldwide research in alternative materials for PZT.

After two decades of research, several representative lead-free piezoelectric candidates emerged:  $(\text{K},\text{Na})\text{NbO}_3$  (KNN);  $\text{Na}_{1/2}\text{Bi}_{1/2}\text{TiO}_3$  (NBT);  $(\text{Ba},\text{Ca})(\text{Zr},\text{Ti})\text{O}_3$  (BCZT) and  $\text{BaTiO}_3\text{-BiFeO}_3$  (BT-BF) based materials. Each  $\text{PbO}$ -free alternative has strengths and weaknesses. KNN based materials nominally have a high  $T_C$  and high piezoelectric coefficient ( $d_{33} > 300$ )<sup>11</sup> but they exhibit a strong temperature dependence from room temperature (RT) to  $100^{\circ}\text{C}$ .<sup>12-14</sup> NBT based materials need a high driving electric field, undergo depolarization at relative low temperatures ( $\sim 150^{\circ}\text{C}$ ) and are highly hysteretic for compositions with high strain ( $>0.35\%$ ).<sup>15</sup> BCTZ based materials show high piezoelectric performances at the expense of a low  $T_C$  ( $<100^{\circ}\text{C}$ ).<sup>16</sup> BT-BF based materials are also promising candidates and some authors have reported good piezoelectric properties and high temperature reliability<sup>17</sup> but high leakage currents are a concern. Many researchers (e.g. refs 18, 19) have suggested that the leakage current in  $\text{BiFeO}_3$  containing systems originates from either the loss of  $\text{Bi}$  or from the formation of  $\text{Fe}^{2+}$  as

opposed to  $\text{Fe}^{3+}$  during sintering. They have also proposed that various dopants alleviate these problems.<sup>20, 21</sup>

BT-BF ceramics are considered to exhibit a morphotropic phase boundary (MPB) like PZT.<sup>18, 22-24</sup> However, in general, there have been reported some different results about crystal structure, suggesting that multiple factors such as sintering conditions, quenching, and dopants affect the phase assemblage.<sup>18, 19, 22, 23, 25, 57, 75</sup> In addition, there have been very few reports about the homogeneity of the microstructure of BT-BF based ceramics so far.<sup>26</sup> Further work is thus required to design the composition and dopants in BT-BF based ceramics to understand and optimise structure-property relations. Therefore, in this project, the relation between the structure, nano/microstructure and the piezoelectric properties in BT-BF systems as a function of dopant concentration and type are investigated. This project consists of following four sub sections:

- i) investigation of optimal dopants in BT-BF ceramics explained through crystallochemical considerations such as tolerance factor and electronegativity difference.
- ii) and iii) investigation of relationships of the structure/microstructure and the piezoelectric properties for  $0.05\text{Bi}(Me)\text{O}_3-(1-x)\text{BaTiO}_3-x\text{BiFeO}_3$  ( $Me = \text{Mg}_{2/3}\text{Nb}_{1/3}, \text{Sc}$ ) ceramics to determine optimum strain in BT-BF systems.
- iv) demonstration of their potential for scale-up to commercial production through the manufacture of prototype multilayer actuators using the representative composition,  $0.05\text{BiMg}_{2/3}\text{Nb}_{1/3}\text{O}_3-0.32\text{BaTiO}_3-0.63\text{BiFeO}_3$ .

## Chapter 2: Literature Review

In this chapter, the basic theory of electroceramics is explained with consideration given to dielectrics, piezoelectrics, and ferroelectrics and relaxors. In addition, representative piezoelectric materials such as  $\text{Pb}(\text{Zr},\text{Ti})\text{O}_3$  (PZT), lead-free piezoelectric materials, and  $\text{BiFeO}_3 - \text{BaTiO}_3$  (BT-BF) based materials are discussed.

## 2.1 Basic theory

### 2.1.1 Dielectrics

Dielectrics are defined as insulators with high polarization and may be gas, liquid or solid. Here, we will only consider solid dielectrics. When a dielectric material is placed between two metal plates and an electric field is applied, current does not pass through the material but both surfaces become charged positive and negative, respectively. This effect is termed polarization and defined as the dipole moment per unit volume. The metric which determines the ability of a material to polarize is called permittivity,  $\epsilon$ . In practice the permittivity relative to that of a vacuum ( $\epsilon_0$ ) often termed the relative permittivity or dielectric constant ( $\epsilon_r$ ) is used to describe the dielectric performance of a material. Polarization occurs over several scale lengths and is generally categorized into four types, as shown in Fig. 2.1.<sup>27</sup> Atomic (or electronic) polarization is a small displacement of the electrons in an atom relative to the nucleus, which occurs in all materials. Ionic polarization is the relative displacement of cations and anions in ionic crystals. Dipolar polarization is a polarization based on the orientations of dipole moment in polar molecules and unit cells such as water and  $\text{BaTiO}_3$ , respectively. Space charge polarization is caused by limited transport of charge carriers which behave like free electrons until they are stopped at a potential barrier such as a grain or phase boundary. Polarization is time dependent and depolarization can occur either after the electric field is removed or if an opposite field is applied in the case of ferroelectrics. The time dependent character of polarization results in relaxation and frequency dependence in alternating applied electric fields. The frequency range of the relaxation depends on the scale length of the polarization with the lowest frequencies associated with space charge. Fig. 2.2 shows the frequency dependences of several kinds of polarization.<sup>27</sup> Space charge and dipolar polarization are strongly temperature dependent but atomic and to a lesser extent ionic polarization are temperature independent.

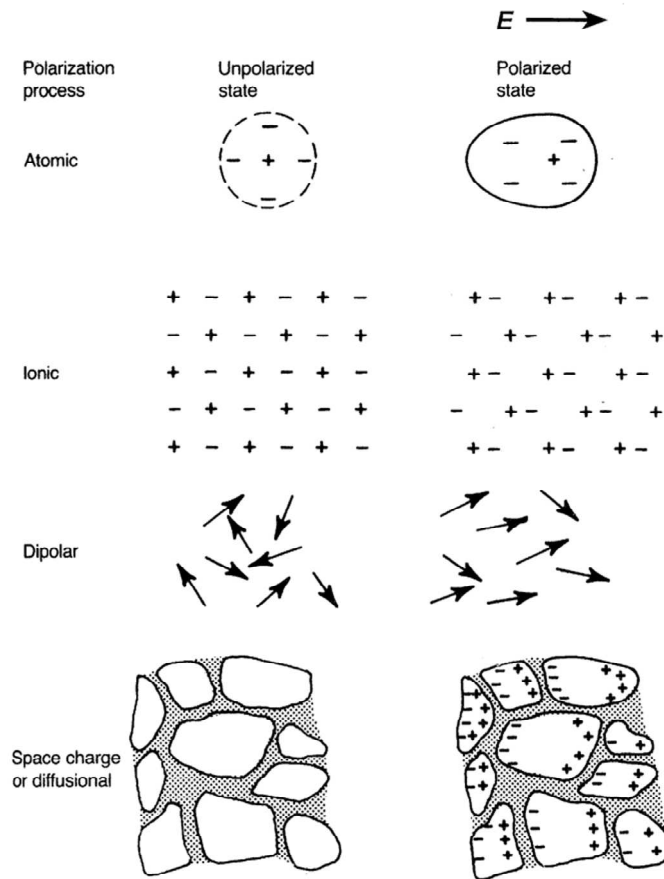


Fig. 2. 1 Schematic of several kinds of polarization

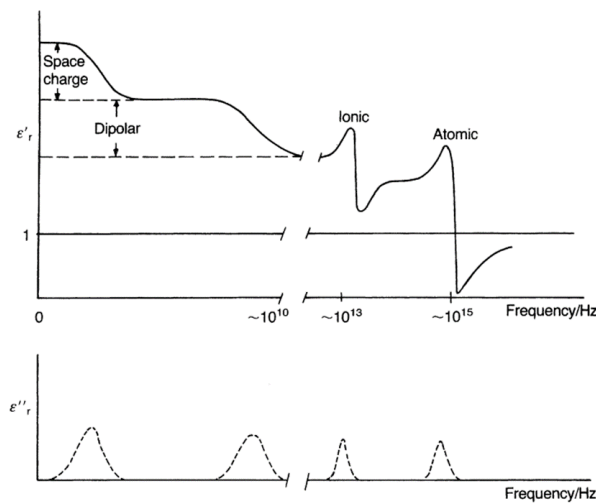


Fig. 2. 2 Frequency dependence of various kinds of polarization.<sup>1</sup>

In an ideal dielectric, the current can lead the applied voltage by  $90^\circ$  phase difference. However, for real dielectric materials, heat is generated when the materials are driven by an AC electric field which gives rise a phase difference of  $90^\circ - \delta$  between the applied electric field and the

resulting polarization. Complex numbers are thus introduced to express actual relative permittivity, which is given by,

$$\epsilon_r^* = \epsilon_r' + j\epsilon_r'' \quad \text{Equation 2.14}$$

where  $\epsilon_r^*$  is the complex relative permittivity,  $\epsilon_r'$  and  $\epsilon_r''$  are the real and imaginary parts of the relative permittivity.  $\epsilon_r^*$  is illustrated as shown in Fig. 2.3 and the dielectric loss of the material is often expressed in terms of the dielectric loss angle  $\delta$ ,

$$\tan \delta = \frac{\epsilon_r''}{\epsilon_r'} \quad \text{Equation 2.2}$$

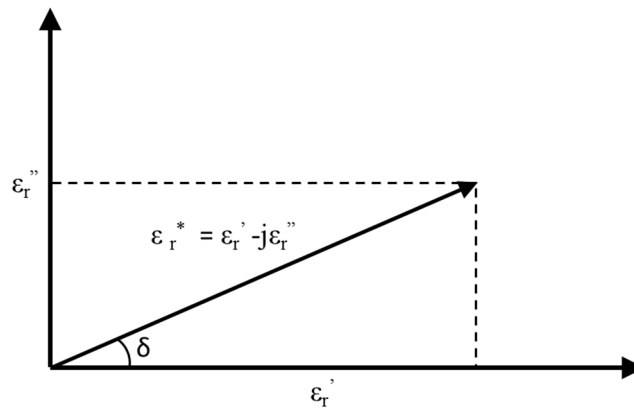


Fig. 2.3 Complex relative permittivity in the complex plane.

Typical dielectric loss values for so-called soft piezoelectric ceramics are 2%, while for hard piezoelectric materials  $\tan\delta$  is much lower and typically  $<1\%$ .<sup>28</sup> Power loss in dielectrics is composed of the relaxation and the conduction in the dielectrics. Therefore, the time average power loss  $P$  is given by,

$$P = \frac{1}{2} U_0^2 \omega C \tan \delta \quad \text{Equation 2.3}$$

Where  $U_0$ ,  $\omega$ , and  $C$  are the voltage, angular frequency, and the capacitance, respectively.

Dielectrics include piezoelectrics, pyroelectrics, and ferroelectrics as shown in Fig. 2.4. Dielectrics are defined as materials that polarise by application of an electric field but for piezoelectrics, polarization can be generated by application of stress and vice versa. Pyroelectrics have a spontaneous electric polarization ( $P_s$ ) and which may be changed by

cooling or heating. In ferroelectrics  $P_S$  can be reversed by an electric field. This classification of materials by the phenomena is related to the symmetry of the crystal system, as shown in Fig. 2.5.<sup>29</sup> All materials can be classified into 32 point groups, 11 of which are centrosymmetric and therefore not piezoelectric. Since all other classes are non-centrosymmetric, they exhibit piezoelectricity, except for the cubic point group 432, where the piezoelectric charges that develop along the 111 polar axes cancel each other.<sup>30</sup> In 10 out of 21 non-centrosymmetric point groups polarization is induced by a mechanical stress, while a further 10 are permanently polar and thus can have piezoelectric as well as pyroelectric effects. Ferroelectric materials are a subgroup of pyroelectrics. Their polarization may be reversed by application of an electric field and as a result, are simultaneously piezoelectric, pyroelectric, and ferroelectric.

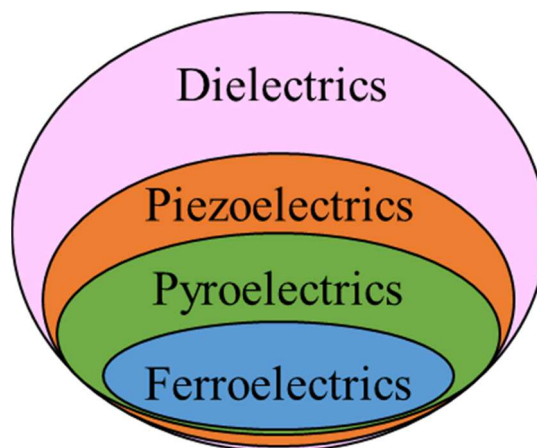


Fig. 2. 4 Subdivision of dielectrics.

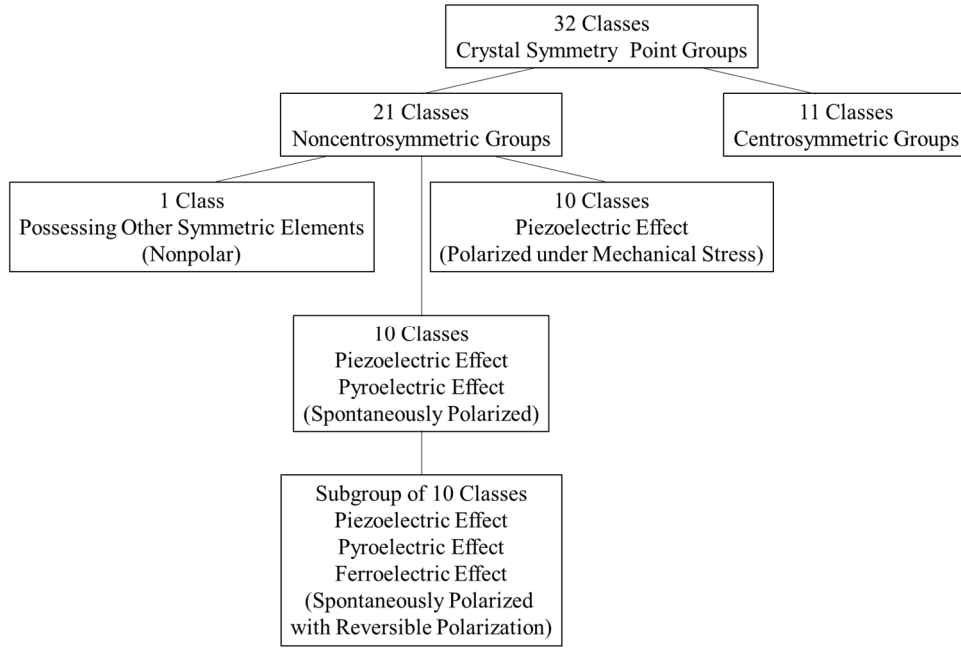


Fig. 2. 5 Classification of crystals showing classes (point groups) with piezoelectric, pyroelectric, and ferroelectric effects.<sup>3</sup>

## 2.1.2 Piezoelectrics

Piezoelectricity is a conversion of mechanical to electric energy. Generally, application of mechanical stress induces the surface charge numerically equal to the change in dielectric displacement, which is called the direct piezoelectric effect. On the other hand, if an electric field causes mechanical strain in the material, it is termed the inverse piezoelectric effect. The behaviour of piezoelectric materials is expressed by the following matrix notation,<sup>28</sup>

$$\begin{pmatrix} \mathbf{S} \\ \mathbf{D} \end{pmatrix} = \begin{bmatrix} s^E & d^{tr} \\ d & \epsilon^T \end{bmatrix} \begin{pmatrix} \mathbf{T} \\ \mathbf{E} \end{pmatrix} \quad \text{Equation 2.4}$$

with :

$\mathbf{S}$ : strain, i.e. relative deformation

$\mathbf{D}$ : Electric displacement (the electric charge per unit area) [C/m<sup>2</sup>]

$\mathbf{T}$ : stress [N/m<sup>2</sup>], i.e. force per unit area

$\mathbf{E}$ : electric field [V/m]

$s^E$ : compliance (strain per unit stress) for constant electric field  $\mathbf{E}$  [m<sup>2</sup>/N]

$d$ : piezoelectric charge constant [C/N] (= [m/V])

$d^{tr}$ : transpose of  $d$

$\epsilon^T$ : permittivity under constant stress  $\mathbf{T}$

In practice, when we describe piezoelectric phenomenon in ceramics, the piezoelectric constant is expressed by tensor quantities because the materials are anisotropic. Piezoelectric *ceramics*, e.g. BaTiO<sub>3</sub> (4mm), exhibit cylindrical symmetry around the poling axis, leaving only three independent  $d_{ij}$  components, and five non-zero components in total. By convention, the direction of polarization is referred to as the ‘3’-direction, and all directions perpendicular to the poling direction are considered as direction ‘1’.<sup>28</sup>

$$\begin{bmatrix} 0 & 0 & 0 & 0 & d_{15} & 0 \\ 0 & 0 & 0 & d_{15} & 0 & 0 \\ d_{31} & d_{31} & d_{33} & 0 & 0 & 0 \end{bmatrix} \quad \text{Equation 2.5}$$

As a result, three piezoelectric ceramics operation modes: longitudinal operation ( $d_{33}$ ); transverse operation ( $d_{31}$ ) and shear operation ( $d_{15}$ ) are necessary to understand the behaviour of piezoelectric ceramics, as shown in Fig. 2.6. In  $d_{33}$ -mode, the direction of the deformation is the same as the applied electric field. In  $d_{31}$ -mode, the direction of the deformation is perpendicular to the applied electric field. These two modes are often considered to be coupled with the following relation:

$$d_{31} \approx -\nu d_{33} \quad \text{Equation 2.6}$$

where  $\nu$  is the Poisson’s ratio. Unlike  $d_{33}$ - and  $d_{31}$ -mode, in  $d_{15}$ -mode the direction of applied field is perpendicular to the direction of the polarization, and the deformation is shear deformation around the other perpendicular axis. In contrast to  $d_{33}$  and  $d_{31}$  operation, for shear mode operation the ceramics can be used with both positive and negative voltages, thus allowing for larger actuation stroke.<sup>28</sup>

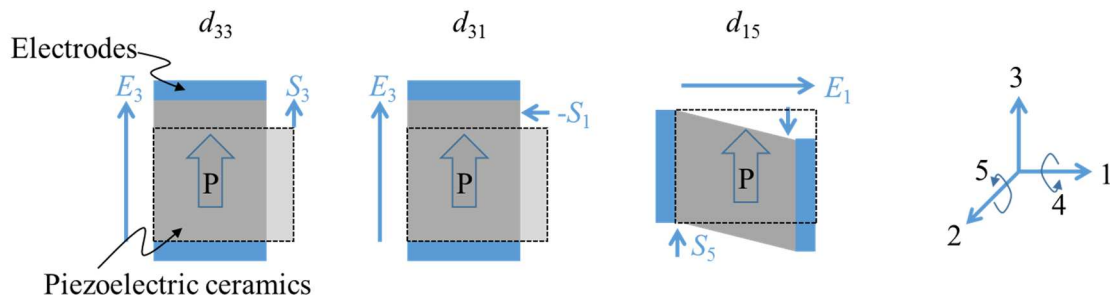


Fig. 2. 6 Modes of operation for a piezoelectric ceramic component.<sup>2</sup>

### 2.1.3 Ferroelectrics

As referred to in the section of 2.1.1, ferroelectrics are dielectrics that exhibit spontaneous polarization which can be reoriented by an electric field. In normal dielectrics, when an electric field is applied, the polarization increases linearly and returns to zero when the field is removed, as shown in Fig. 2.7. In ferroelectrics, the polarization does not return to zero giving rise to remanent polarization ( $P_r$ ) at  $E = 0$ . At the coercive electric field ( $E_c$ ), the polarization is reoriented simultaneously (Fig. 2.7), giving rise to a PE hysteresis loop which for an ideal ferroelectric is square shaped. This phenomenon was first discovered in Rochelle Salt ( $\text{NaKC}_4\text{O}_6 \cdot 4\text{H}_2\text{O}$ ) by J. Valasek in 1920. Since several features of this behaviour were analogous to ferromagnetics, they were named “ferroelectrics.”

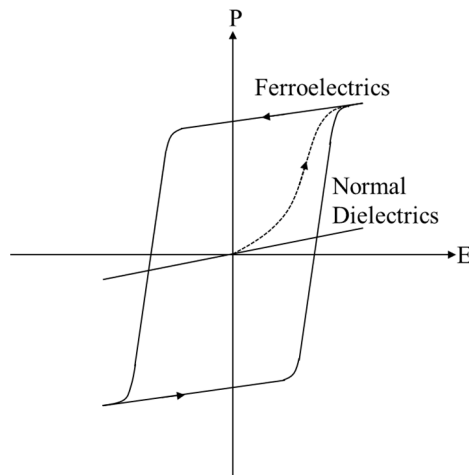


Fig. 2. 7 Polarization (P) vs electric field (E) curve for normal dielectrics and ferroelectrics.

Ferroelectrics behaviour vanishes at the Curie temperature ( $T_C$ ) due to the phase transition from low to high symmetry crystal structure, e.g. cubic. For most ferroelectrics  $\epsilon_r$  reaches a peak at  $T_C$  and falls off at higher temperatures in accordance with the Curie-Weiss law,

$$\epsilon_r - 1 = \frac{A}{T - \theta_C} \quad \text{Equation 2.7}$$

where  $A$  is a constant for a given material and  $\theta_C$  is a temperature near to but not identical with  $T_C$ . In ferroelectrics,  $\epsilon_r - 1 \approx \epsilon_r$  and since  $\epsilon_r \gg 1$ , the Curie-Weiss law can be approximated to a direct relation between  $1/\epsilon_r$  and temperature ( $T$ ). A schematic representation of  $\epsilon_r$  and  $P_s$  for first order transition as a function of temperature is shown in Fig. 2.8. Generally, the temperature region lower than  $\theta_C$  is called the ferroelectric state and the temperature region

higher than  $\theta_C$  is paraelectric.

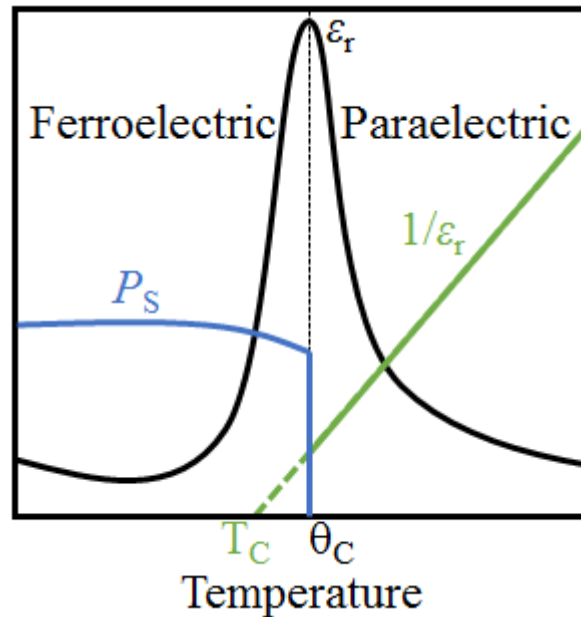


Fig. 2. 8 Schematic of polarization and relative permittivity as a function of temperature.

Ferroelectric materials are classified into four groups based on their crystal structures: layered (e.g.  $\text{Bi}_4\text{Ti}_3\text{O}_{12}$ ); perovskite (e.g.  $\text{BaTiO}_3$ ,  $\text{PbTiO}_3$ ); pyrochlore group (e.g.  $\text{CdNb}_2\text{O}_7$ ) and tungsten bronze ( $\text{PbNb}_2\text{O}_6$ ,  $\text{SrNb}_2\text{O}_6$ ). Among these groups, perovskites are the most important economically and BT-BF based materials (the subject of this thesis) belong to this group.<sup>31</sup> Perovskite oxide are described with the chemical formula  $\text{ABO}_3$  where A and B are metallic cations and O is the anion. An ideal perovskite structure is illustrated in Fig. 2.9 where A and B site cations are coordinated to 12 and 6 oxygens, respectively.<sup>31</sup>

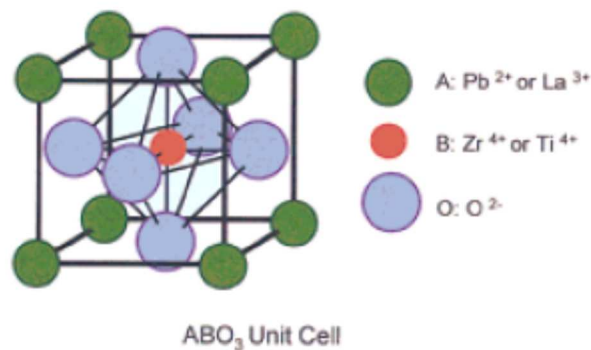


Fig. 2. 9 Ideal perovskite structure,  $\text{ABO}_3$ .<sup>31</sup>

To estimate the stability of perovskite ceramics with respect to ion size and bonding energy

between ions, the tolerance factor and electronegativity difference are commonly used and referred to in this thesis. The tolerance factor ( $t$ ) was introduced by Goldschmidt<sup>32</sup> in 1926 and was used to describe the local strain and stability of a perovskite phase by Megaw.<sup>33</sup> It has been used many times to predict/explain properties. It is defined as:

$$t = \frac{r_A + r_O}{\sqrt{2}(r_B + r_O)} \quad \text{Equation 2.8}$$

where  $r_A$ ,  $r_B$ ,  $r_O$  denote the radius of the A-site, B-site and oxygen ion, respectively.<sup>3, 34</sup> Compounds in perovskite family exist over the range of  $0.78 < t < 1.05$ .<sup>35</sup> When the tolerance factor of a crystal is close to 1.0, the crystal structure is more stable and given a matrix composed of highly polarisable ionic species, ferroelectric properties are encouraged.

To understand further what happens in a perovskite crystal as a function of tolerance factor, we can take advantage of the mechanism of octahedral tilting that Glazer classified in 1972.<sup>36</sup> An ideal perovskite ( $t \sim 1.0$ ) does not undergo octahedral tilting but occurs for  $t < 1$ . Octahedral tilting or rotations occurs in a cogwheel motion to effectively reduce the pseudocubic lattice parameters and cell volume. If, around a given pseudocubic axis, all sheets of octahedra rotate in the same sense (e.g. all clockwise) they are said to have tilted in phase. If each sheet of octahedra rotate in alternate senses (clockwise/anticlockwise) they are said to be tilted in antiphase. When octahedral tilting occurs, the volume of the A-site interstice is reduced and the structural stability is improved for a given system

Reaney et al. demonstrated the dependence of tilting on tolerance factor in Ba and Sr based complex perovskites.<sup>37</sup> At room temperature, for  $0.985 < t < 1.06$  perovskites are expected to have untilted structures. Perovskites with  $0.964 < t < 0.985$  are tilted in antiphase and perovskites with  $t < 0.964$  are expected to show in-phase and antiphase tilting. Woodward and Reaney investigated the relationships between the tilting and the superstructure reflections in electron diffraction in perovskites in more detail.<sup>38</sup>

Electronegativity difference,  $e_n$ , can also indicate the stability of the crystal structure and is expressed as:

$$e_n = \frac{X_{a-o} + X_{b-o}}{2} \quad \text{Equation 2.9}$$

where  $X_{a-o}$  is the difference between the electronegativity of the A ion and the oxygen ion,  $X_{b-o}$  is the difference between the electronegativity of the B ion and the oxygen ion. When  $e_n$  is

large, the bonding energy between the cation and oxygen ion increases and the crystal structure becomes more stable.<sup>39, 40</sup>

In the field of ferroelectrics, the region where the neighbouring dipoles align with each other are called domains. Domains are normally separated by a domain wall which has been reported to be from 2-3 unit cells to several nanometers wide.<sup>136</sup> Domains and the domain walls are formed when the materials pass through the phase transition temperature. BaTiO<sub>3</sub> changes from cubic to tetragonal at  $T_C$ . There are six possible directions for the polar tetragonal axis in the crystal, which causes complicated domain pattern. The domain patterns separated by domain walls are formed as a result of the stresses created at  $T_C$ , uncompensated surface charges, and physical imperfections.<sup>41</sup> The domain patterns that appear depend on the crystal system. In tetragonal BaTiO<sub>3</sub>, the polarization direction is  $\langle 001 \rangle$  and hence 180° and 90° domain are generated, whereas rhombohedral BaTiO<sub>3</sub> shows 180°, 109°, and 71° domains because the direction of the polarization is  $\langle 111 \rangle$ .<sup>42</sup> Net polarization of ferroelectric ceramics is zero because the directions of polarization are random. However, this domain patterns can be changed by application of either an electric field or a mechanical stress. Application of a static electric field to ferroelectrics to align the directions of polarization is called poling, as shown in Fig. 2.10.<sup>27</sup>

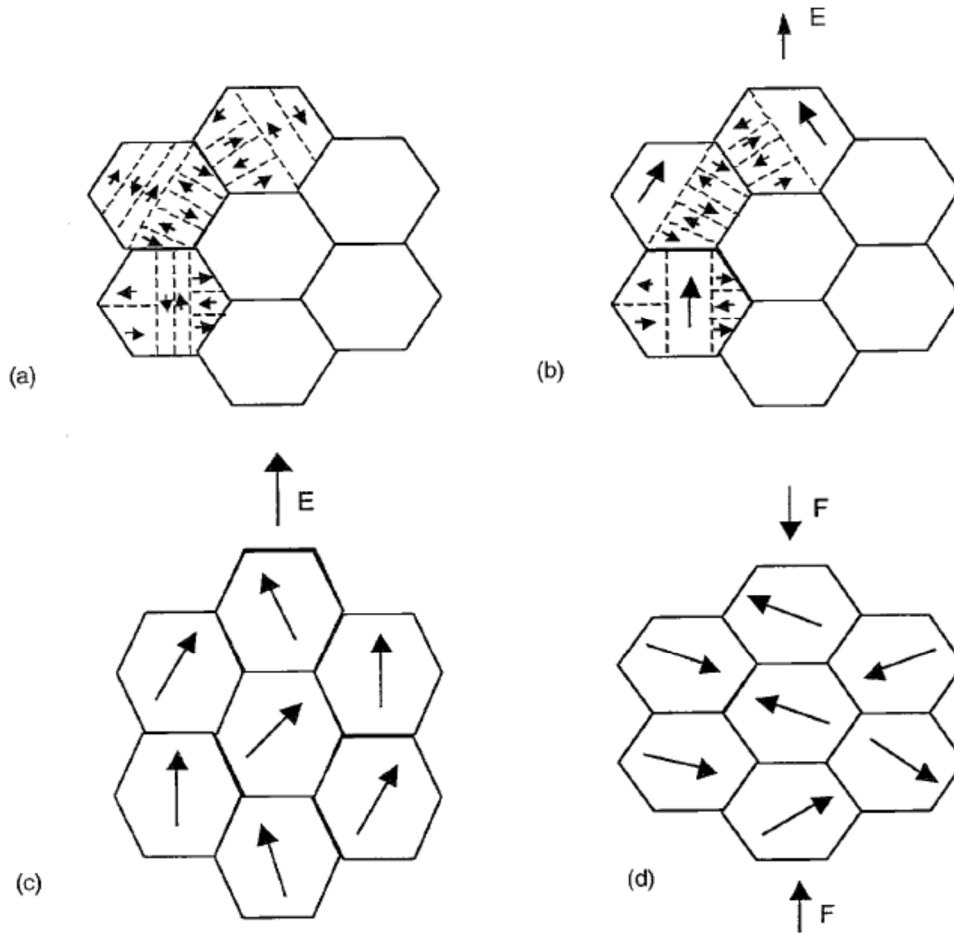


Fig. 2. 10 Schematic of domain changes in ceramics by application of an electric and a mechanical stress: (a) stress free, (b) with applied electric field, (c) with further increased applied electric field and (d) with mechanical stress.

Since the remnant polarization can be reversed by an electric field in ferroelectrics, they show a distinct strain behaviour in bipolar strain measurement, the so-called butterfly curve, as shown in Fig. 2.11. Strain increases as applied electric field increases, reaching a maximum strain ( $S_{max}$ ) at  $E_{max}$  where all possible domains are aligned in one direction. Here, an important figure of merit for actuators known as a large signal piezoelectric coefficient  $d_{33}^*$  can be calculated by the following equation,

$$d_{33}^* = \frac{S_{max}}{E_{max}} \quad \text{Equation 2.10}$$

When the applied electric field decreases to zero, the strain does not return to zero because of the remnant polarization in the ceramics, giving rise to the remanent strain ( $S_{rem}$ ). The remanent

polarization makes the strain negative until the applied electric field reaches  $-E_C$ . This is because the polarization direction is opposite to the applied electric field and the ceramic is compressed. When the strain reaches a minimum ( $S_{\min}$ ) at  $-E_C$ , the polarization (i.e. domains) begin to reverse and the strain turns positive and reaches to  $S_{\max}$  at  $-E_{\max}$  where the direction of the polarization is opposite to that at  $E_{\max}$ . When the applied electric field goes to zero, the strain decreases through  $S_{\text{rem}}$  at  $E = 0$  and reaches  $S_{\min}$  at  $E_C$  followed by the strain reaching  $S_{\max}$  at  $E_{\max}$  again. In ideal ferroelectrics, this strain curve and also PE hysteresis loop are perfectly symmetric but the symmetry can be disturbed by many factors including the presence of charged defects and residual mechanical stresses resulted from sample preparations and thermal treatments.

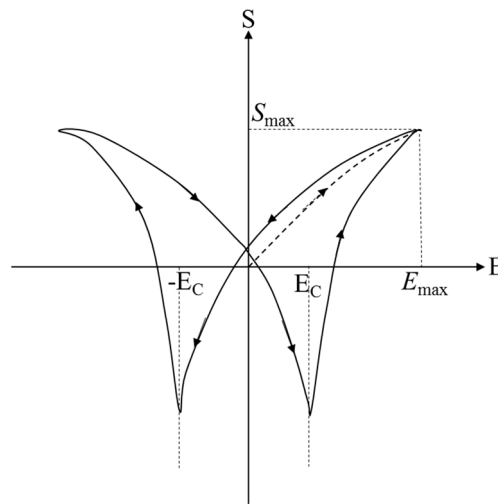


Fig. 2. 11 Schematic of bipolar strain curve of ferroelectrics along the polarisation axis.

## 2.1.4 Relaxors

Relaxors are a ferroelectric group which shows apparently different dielectric behaviour from normal ferroelectrics such as  $\text{BaTiO}_3$  and  $\text{Pb}(\text{Zr}, \text{Ti})\text{O}_3$ , with abroad frequency dependent dielectric anomalies as a function of temperature. G.A. Smolenskii was a pioneering researcher and at the time relaxors were being intensively studied in Russia.<sup>43, 44</sup>  $\text{Pb}(\text{Mg}_{1/2}\text{Nb}_{1/2})\text{O}_3$  (PMN),  $(\text{Pb},\text{La})(\text{Zr}, \text{Ti})\text{O}_3$  (PLZT), and  $(\text{Bi}_{1/2}\text{Na}_{1/2})\text{TiO}_3$  (BNT) are well known relaxors. As shown in Fig. 2.12, the temperature where  $\epsilon_r$  reaches a maximum ( $T_m$ )

shifts to higher temperature and  $\epsilon_r$  decreases as frequency increases.<sup>1</sup> These trends are not observed in normal ferroelectrics where the dielectric anomaly around  $T_C$  is sharp and there is no frequency dependence of  $\epsilon_r$  vs. temperature.

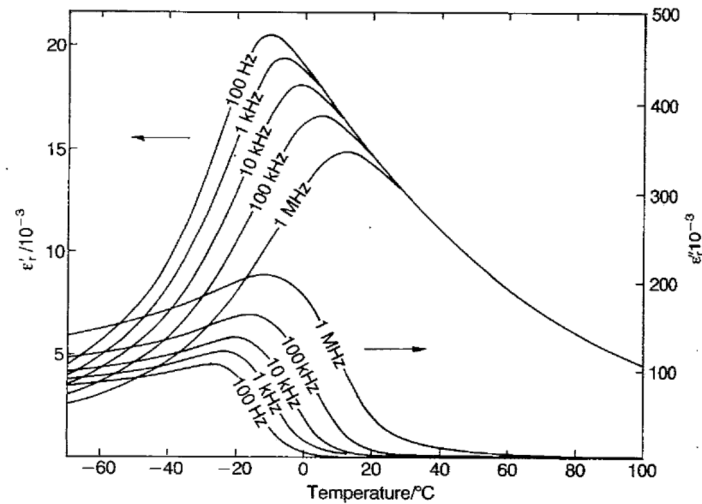


Fig. 2. 12 Dielectric properties of  $\text{Pb}(\text{Mg}_{1/2}\text{Nb}_{1/2})\text{O}_3$  (PMN).<sup>1</sup>

Also, relaxors show distinct features in PE hysteresis loop and bipolar strain curve which are quite different from those of ferroelectrics. Fig. 2.13 shows PE hysteresis loop and bipolar strain curve for a normal ferroelectric and slim-loop ferroelectric (SFE) relaxor ceramic.<sup>45</sup> Unlike ferroelectric ceramics, SFE relaxors show no remnant polarization and hysteresis in PE loops. In addition, the bipolar SE curve shows a parabolic curve without negative strain, and not a butterfly curve. These means that relaxors can generate high strain by application of electric field but cannot generate a voltage by application of mechanical stress. Relaxors, therefore, due to their high relative permittivity and negligible hysteresis strain, are used applications such as capacitors and actuators. Additionally, the broad dielectric anomaly in relaxors renders greater intrinsic temperature stable.<sup>46</sup>

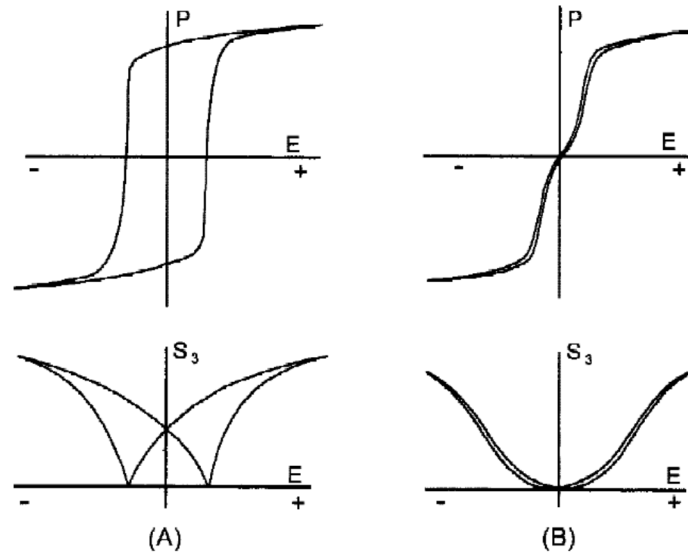


Fig. 2. 13 PE hysteresis loop and bipolar SE curve for (A) ferroelectric memory ceramic and (B) SFE (Slim-loop ferroelectric) nonmemory relaxor ceramic.<sup>45</sup>

Several models<sup>47-53</sup> about the origin of the peculiar features of relaxors have been proposed and discussed. The consensus suggests that relaxor behaviour relates to a nanoscale domain structure, called polar nanoregions (PNRs), typically 2-10 nm. Since there are several sizes of PNR reported by many researchers, the dielectric anomaly is relaxed and the peak becomes broad and shows frequency dependence. As the PNRs are small, the polarization in each domain cannot keep pace with the direction of the applied field as *ac* frequency increases. Hence,  $\epsilon_m$  is frequency dependent. For PE loops and SE curves, the PNRs align readily with field due to their small size, hence  $E_c$  is negligible and there is little negative strain. Relaxor behavior will be discussed later in the thesis in the light of experimental data.

### 2.1.5 Morphotropic phase boundary (MPB) and electromechanical properties

The most extensively used strategy to enhance the electromechanical properties is the concept of a morphotropic phase boundary (MPB). It has been well known that many piezoelectric/dielectric materials show a divergence of the properties in the phase transition region which are driven by stress, electric field, temperature, and composition. Fig. 2.14 shows

temperature-composition diagram and dependence of electromechanical properties on composition for PZT.<sup>56, 57</sup> Shirane et al.<sup>54</sup>, Sawaguchi,<sup>55</sup> and Jaffe et al.<sup>57</sup> in the early 1950s reported that PZT shows divergence of the properties at compositions separating rhombohedral and tetragonal phase. Since this compositionally driven phase transition is nearly independent of temperature, PZT has been widely applied to many applications. The tetragonal phase has six spontaneous polarization directions along  $\langle 001 \rangle$  and rhombohedral eight along  $\langle 111 \rangle$ . Therefore, at the MPB, there exists many possible polarization directions and high piezoelectric properties are generated. In addition to this, Noheda<sup>58</sup> reported a monoclinic phase between the rhombohedral and tetragonal phase in PZT in 2000, as shown in Fig. 2.15.<sup>33</sup> Monoclinic phase has 24 possible polarization direction which can make it easier to enhance electromechanical properties. The enhancement of electromechanical properties at MPB is explained using polarization rotation. In particular, extrinsic effects relating to domain wall motion are optimized at the MPB and contribute hugely to the piezoelectric response. Jones et al.<sup>137</sup> reported that approximately 34% of measured piezoelectric coefficient  $d_{33}$  in PZT is caused by extrinsic components such as non-180° domain switching.

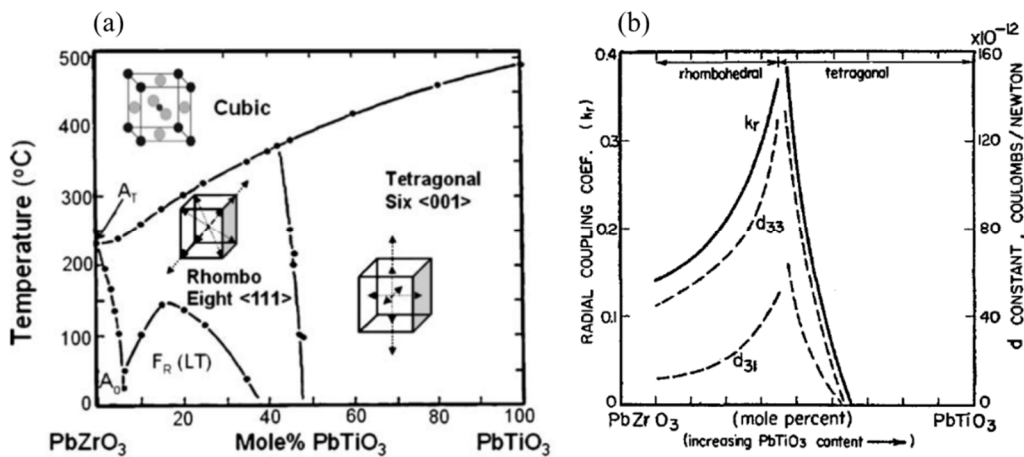


Fig. 2. 14 (a) Phase diagram<sup>56</sup> and (b) electromechanical properties<sup>57</sup> of PZT.

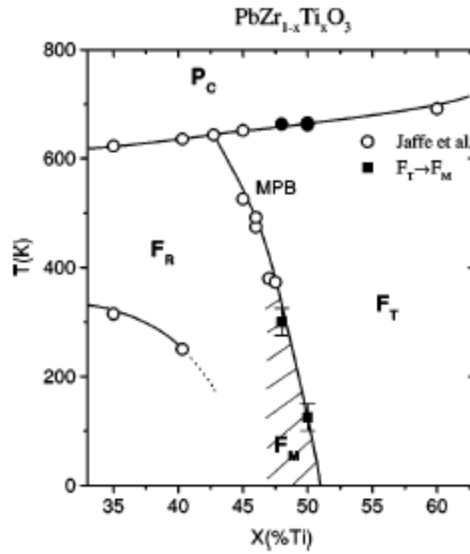


Fig. 2. 15 Phase diagram of PZT with monoclinic phase.<sup>58</sup>

The structural transformations in  $\text{BaTiO}_3$  can be considered as a temperature-driven ferroelectric-paraelectric phase transition (sometimes referred to as an MPB but not temperature independent as in the case of PZT) around  $T_C$  where the dielectric properties are enhanced between the ferroelectric (below  $T_C$ ) and paraelectric phase (above  $T_C$ ), as shown in Fig. 2.15. When  $\text{BaTiO}_3$  transform from cubic to tetragonal at  $T_C$ , the polarization direction is changed in one-dimension along  $[001]_C$ . This is termed polarization extension. Damjanovic suggested that the ideal compositionally-driven MPB is where there are polarization rotation and polarization extension regions, as shown in Fig. 2.17.

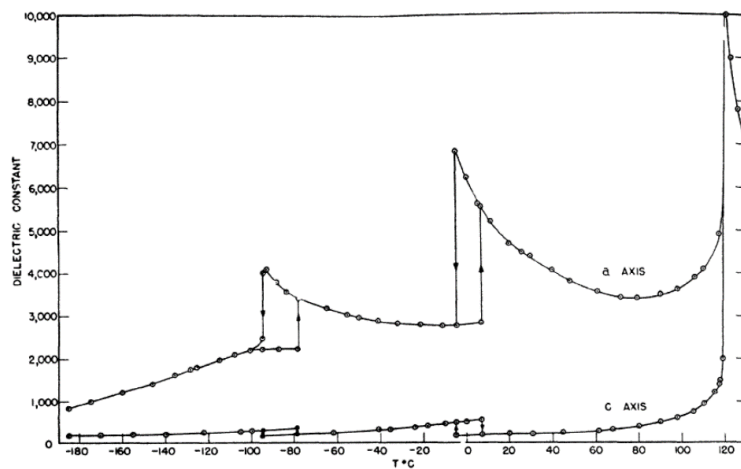


Fig. 2. 16 Phase diagram of single-crystal  $\text{BaTiO}_3$ .<sup>59</sup>

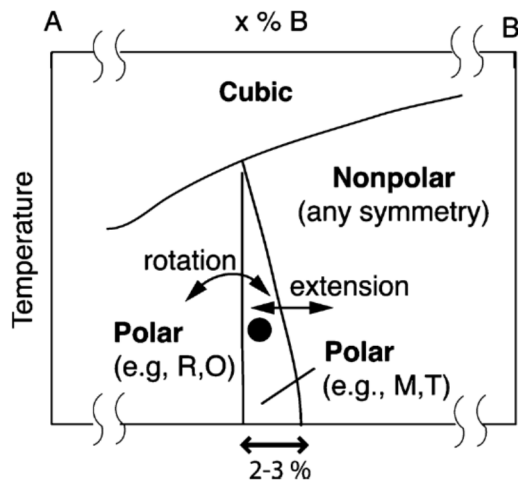


Fig. 2. 17 A hypothetical phase diagram exhibiting an MPB region where both polarization rotation and polarization extension may be strong.<sup>60</sup>

## 2.2 Piezoelectric materials

### 2.2.1 Introduction

The piezoelectric phenomenon was first discovered in quartz by Pierre and Jacques Curie in 1880.<sup>61</sup> They found that application of mechanical stress generates electric charge on the surface of quartz which is now referred to as the direct piezoelectric effect. The inverse piezoelectric effect was mathematically deduced from fundamental thermodynamic principles by Gabriel Lippmann in 1881<sup>62</sup> which was later experimentally confirmed by the Curie brothers. Over the next few decades, 20 natural crystals were found to show piezoelectricity and their properties rigorously defined using tensor analysis.

The first application using piezoelectric material was conducted by Paul Lengvin in 1917 during World War I when quartz was used as ultrasonic submarine detectors, so-called sonar. During World War II, BaTiO<sub>3</sub> was simultaneously discovered in the USA, Russia, and Japan. Since BaTiO<sub>3</sub> has much higher dielectric and piezoelectric properties than natural materials the development of piezoelectric materials was accelerated, leading to the discovery of Pb(Zr,Ti)O<sub>3</sub> (PZT) after World War II.<sup>54, 55, 57</sup> PZT has a MPB and hence shows high piezoelectric properties with high Curie temperature. Also, the properties can be controlled by dopants, categorizing PZT into soft PZT (donor doped) and hard PZT (acceptor doped).<sup>64, 65</sup>

These features have made PZT the most widely used piezoelectric material to date.

Following increased environmental awareness during the second half of 20<sup>th</sup> century, lead has become subject to increasing legal restraints that prohibit its usage, alongside mercury, cadmium and hexavalent chromium in electronic devices. The Restriction of Hazardous Substances Directive (RoHS) was adopted in 2003 by the European Union<sup>66</sup> and has effectively driven the development of lead-free material substitutes. However, to date there no lead free piezoelectric able to fully replace PZT.

### 2.2.2 Lead-free piezoelectric materials

Two decades of study on lead-free piezoelectrics has led to the development of a range of lead-free materials based on (K,Na)NbO<sub>3</sub> (KNN), Na<sub>1/2</sub>Bi<sub>1/2</sub>TiO<sub>3</sub> (NBT), and (Ba,Ca)(Zr,Ti)O<sub>3</sub> (BCZT). Each PbO-free alternative has strong and weak points. Extensive research on KNN based materials was triggered by Saito et al. in 2004<sup>67</sup> when textured (K<sub>0.44</sub>Na<sub>0.52</sub>Li<sub>0.04</sub>)(Nb<sub>0.86</sub>Ta<sub>0.10</sub>Sb<sub>0.04</sub>)O<sub>3</sub> at an MPB between tetragonal and rhombohedral phases achieved  $d_{33} = 416$  pC/N and strain 0.15% at 2 kV/mm ( $d_{33}^* = 750$  pm/V) and  $T_C = 253^\circ\text{C}$ .  $d_{33}$  is comparable to that of PZT but the orthorhombic to tetragonal phase transition temperature between room temperature and  $T_C$ , induces changes in the properties and piezoactivity decreases with increase in temperature.<sup>68, 69</sup> Wang et al.<sup>14, 70</sup> reported the composition, 0.92(Na<sub>0.5</sub>K<sub>0.5</sub>)NbO<sub>3</sub>-0.06(Bi<sub>1/2</sub>Li<sub>1/2</sub>)TiO<sub>3</sub>-0.02BaZrO<sub>3</sub> with  $d_{33} = 348$  pC/N at RT but which decreased to around 200 pC/N at 200°C. Giant strain in NBT has also been reported by Zhang et al. (2007)<sup>71</sup> with the ternary system of (0.94-x)Bi<sub>0.5</sub>Na<sub>0.5</sub>TiO<sub>3</sub>-(0.06)BaTiO<sub>3</sub>-(x)K<sub>0.5</sub>Na<sub>0.5</sub>NbO<sub>3</sub> ceramics exhibiting 0.45% strain at 8 kV/mm ( $d_{33}^* = 562$  pm/V). Since then many researchers have studied NBT based materials and recently Liu et al. (2016)<sup>72</sup> reported that polycrystalline ceramics with [Bi<sub>1/2</sub>(Na<sub>0.8</sub>K<sub>0.2</sub>)<sub>1/2</sub>](Ti<sub>0.985</sub>Ta<sub>0.015</sub>)O<sub>3</sub> 0.62% strain under a moderate bipolar field of 5 kV/mm ( $d_{33}^* = 1240$  pm/V) which is comparable to lead-free ferroelectric single crystals. However, BNT based materials undergo depolarization ( $T_d$ ) at ~ 100°C.<sup>72, 73</sup> and it is thus difficult to utilize them for high temperature applications.

BCTZ based materials are another representative lead-free piezoelectric material. Liu and Ren (2009)<sup>74</sup> reported 0.50Ba(Zr<sub>0.2</sub>Ti<sub>0.8</sub>)O<sub>3</sub>-0.50(Ba<sub>0.7</sub>Ca<sub>0.3</sub>)TiO<sub>3</sub> with a high piezoelectric

coefficient of  $d_{33}$  ~620 pC/N and a strain of 0.057% at 0.5 kV/mm ( $d_{33}^* = 1140$  pm/V), purportedly due to an MPB (not temperature independent as in PZT) at a tricritical point (TCP) consisting of tetragonal, rhombohedral, and cubic phases which gives a low energy barrier for polarization rotation and lattice distortion. However, BCTZ cannot be used at high temperature due to the low  $T_C$  (<100 °C) but compositions do not contain volatile, endangered raw materials and hence the processing is comparatively easy.

### 2.2.3 BaTiO<sub>3</sub>-BiFeO<sub>3</sub> based piezoelectric materials

BaTiO<sub>3</sub>-BiFeO<sub>3</sub> (BT-BF) based materials are also promising candidate for lead-free piezoelectrics. BaTiO<sub>3</sub> is tetragonal and BiFeO<sub>3</sub> rhombohedral at room temperature with high  $T_C$ . Solid solutions therefore, are expected to show strong piezoelectric properties. Lee et al. (2015)<sup>17</sup> reported quenched 0.67Bi<sub>1.05</sub>(Fe<sub>0.97</sub>Ga<sub>0.03</sub>)O<sub>3</sub>-0.33BaTiO<sub>3</sub> with  $d_{33} = 402$  pC/N and high  $T_C = 454^\circ\text{C}$ . They suggested that optimum compositions lie at an MPB between rhombohedral and tetragonal phases. Although there are significant challenges to apply quenching within an industrial process, this result shows the potential of BT-BF ceramics for piezoelectric applications.

PZT is known to have an optimised  $d_{33}$  and electromechanical coupling coefficient ( $k$ ) at the MPB. BT-BF ceramics have also been reported to exhibit an MPB (between rhombohedral and cubic and thus unlike PZT).<sup>18, 19, 22, 23, 25, 26, 75</sup> Wei et al.<sup>23</sup> recorded that 0.30BT-0.70BF (MPB composition) shows the highest  $d_{33}$  of 134 pC/N whereas Kumar and co-workers<sup>18</sup> suggested that (1- $x$ )BT-( $x$ )BF ceramics transform from tetragonal to rhombohedral at  $0.5 < x < 0.6$ , at which compositions the structure appears to be pseudocubic. In general, there is no clear consensus concerning the changes in crystal structure as a function of composition within the BT-BF system,<sup>57, 18, 19, 22, 23, 25, 75</sup> suggesting that multiple factors such as sintering conditions, quenching and dopants affect the phase assemblage. The same is true of microstructure. Yabuta et al.<sup>26</sup> reported about the compositional inhomogeneity of (1- $x$ )(0.33BaTiO<sub>3</sub>-0.67BiFeO<sub>3</sub>)-( $x$ )Bi(Mg<sub>1/2</sub>Ti<sub>1/2</sub>)O<sub>3</sub> ( $x = 0, 0.05, 0.10, \text{ and } 0.15$ ) ceramics but there have been few papers referring to the relationships between the microstructure and the properties in a systematic investigation of BT-BF. Further work is thus required to design the

composition and dopants of the BT-BF system to understand and optimise structure-property relations.

The biggest drawback of BiFeO<sub>3</sub> containing systems is the high leakage current from either the loss of Bi or from the formation of Fe<sup>2+</sup> as opposed to Fe<sup>3+</sup> during sintering. Since Bi is a volatile element, it can easily volatilize at high sintering temperature. The loss of Bi can result in oxygen vacancies, V<sub>O</sub>, leading to a high leakage current. The valence of Fe is known to easily change as seen in the complex phase diagram of iron oxides. Valence fluctuations between Fe<sup>3+</sup> and Fe<sup>2+</sup> induce electron hopping between defect trap centers and contribute to the leakage current.<sup>138</sup> To resolve these problems in BT-BF, either excess Bi<sub>2</sub>O<sub>3</sub> is added to compensate for volatilisation<sup>20</sup> or dopants are used to accommodate changes in defect chemistry associated with the multiple valence state of Fe.

#### 2.2.4 Dopants in BaTiO<sub>3</sub>-BiFeO<sub>3</sub> based materials

As alluded to above, many researchers have pointed out the drawbacks of a BiFeO<sub>3</sub> containing system for high field applications in which, either the loss of Bi or the formation of mixed valence Fe ions results in large leakage currents.<sup>76-92</sup> Various dopants however, have been shown to alleviate these problems. Rare earth ions are reported to substitute on the A site of BiFeO<sub>3</sub> and improve  $d_{33}$  but there are conflicting reports as to whether they improve breakdown strength/ $d_{33}$  of BT-BF ceramics.<sup>85-91</sup> Most dopants reported to improve the resistivity and enhance piezoelectric activity reside on the B-site of BiFeO<sub>3</sub>.<sup>76-84</sup> In BT-BF ceramics, many researchers suggest that dopants should be chosen to enhance tetragonality.<sup>20, 76, 77</sup> Zhou *et al.*<sup>76</sup> reported that Al<sup>3+</sup> promotes the coexistence of rhombohedral and orthorhombic phases in 0.725BiFe<sub>1-x</sub>Al<sub>x</sub>O<sub>3</sub>-0.275BaTiO<sub>3</sub> + 1 mol% MnO<sub>2</sub> ceramics ( $x = 0.01-0.03$ ) and improves  $d_{33}$  from 126 pC/N ( $x = 0$ ) to 138 pC/N ( $x = 0.02$ ). Zhou *et al.*<sup>81</sup> reported that for 0.71BiFe<sub>1-x</sub>(Ni<sub>1/2</sub>Ti<sub>1/2</sub>)<sub>x</sub>O<sub>3</sub>-0.29BaTiO<sub>3</sub> ( $x = 0-0.09$ ) + 0.6 wt% MnO<sub>2</sub> ceramics, the lattice parameter of the pseudocubic structure increases as  $x$  increases and that  $x = 0.03$  showed the highest  $d_{33} = 156$  pC/N. On the other hand, Luo *et al.* [30] reported the piezoelectric properties for both A and B site doped BT-BF, (0.75-x)BiFeO<sub>3</sub>-0.25BaTiO<sub>3</sub>-xLa(Co<sub>0.5</sub>Mn<sub>0.5</sub>)O<sub>3</sub> + 1 mol% MnO<sub>2</sub> ceramics, which they reported to show an MPB of rhombohedral and

orthorhombic structures ( $0.01 \leq x \leq 0.03$ ) with  $d_{33} \sim 108$  pC/N ( $x = 0.02$ ). As evidenced in the brief literature presented above, doped BT-BF ceramics exhibit the coexistence of crystal structures, which are reputed to give rise to a large piezoelectric response but there are no crystallochemical trends that have been shown to predict the optimum dopant types in BT-BF ceramics. The most comprehensive study to date by Zheng *et al.*<sup>77</sup> investigated the piezoelectric properties for  $0.70\text{Bi}_{1.05}\text{Fe}_{0.97}\text{A}_{0.03}\text{O}_3\text{-}0.30\text{BaTiO}_3$  (A: Sc, Ga, Al, In, Ni, Co) ceramics and reported the ceramics with Sc, Ga, and Al showed large  $d_{33}$  (160-180 pC/N) but piezoelectric properties in these samples were optimised with a quenching technique not suitable for industrial scale-up. There is still therefore, a need to synthesise and investigate non-quenched BF-BT ceramics with high strain/piezoelectric performance but it is clear from previous studies that suitable dopants need to be determined.

Dopants in the field of piezoelectric materials are classified into three groups; donor (higher valence), acceptor (lower valence) and self-compensated (average valence number remains the same). All the above-mentioned dopant strategies improve the resistivity of BT-BF ceramics as reported in the literature.<sup>54, 57, 78, 81, 85, 92-102</sup> Wang *et al.*<sup>94</sup> reported that Nb (donor) improves the resistivity of BT-BF while it gives rise to a decrease in the grain size. Curiously, acceptor dopants also improve the resistivity of BT-BF.<sup>98, 99</sup> For instance, as Yao and co-workers<sup>81</sup> reported, Mn increases the resistivity and decreases the dielectric loss of 0.8BF-0.2BT ceramics. However, the most successful dopants are stoichiometric or self-compensated (e.g. Cr, Co, Al, Ga,  $\text{Mg}_{1/2}\text{Ti}_{1/2}$ ,  $\text{Zn}_{1/2}\text{Ti}_{1/2}$  and  $\text{Ni}_{1/2}\text{Ti}_{1/2}$ ) which not only improve the resistivity of furnace cooled ceramics but also their piezoelectric properties.<sup>17, 99-103</sup> Nonetheless, the  $d_{33}$  of furnace-cooled doped BF-BT compositions is typically much smaller (163 pC/N) than that of quenched samples.<sup>74, 100</sup>

## Chapter 3: Experimental techniques

This chapter details the experimental techniques used in this project for the fabrication and characterisation of BT-BF based ceramics and multilayers.

### 3.1 Particle size analysis

Particle size is critical to control the packing of particles during pressing and improve final ceramic density. In this project, therefore, particle size analysis was conducted on raw materials, before and after drying and attrition milling, calcined powders and attrition milled calcined powders. A Mastersizer 3000 (Malvern Instrument Ltd.) was used to measure the particle size distribution which uses a laser diffraction measurement to take advantage of how particles scatter the incident laser light. When the particle size is large, the beam scattering angle is small, while small particles scatter more greatly the incident light as shown in Fig. 3.1.<sup>104</sup> The intensity of the angular scattering is analysed to calculate the particle size which creates the pattern of scattering using Mie theory. The particle size is reported as a volume equivalent sphere diameter. The range of particle size which can be measured is from 0.1 to 1000  $\mu\text{m}$ .

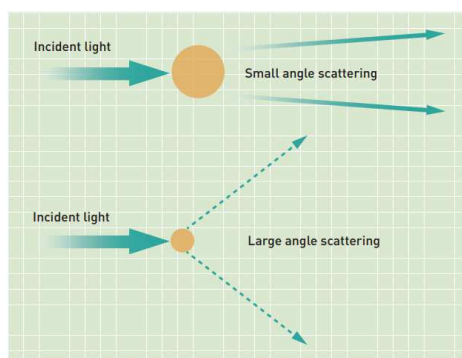


Fig. 3. 1 Concept of a laser diffraction measurement.<sup>1</sup>

### 3.2 Density measurements

Density of substance is defined as its mass per unit volume. In this project, the assessment of apparent density was conducted using the Archimedes' principle to enable

calculation of the relative density of ceramics.

### 3.2.1 Archimedes' density

Density measurement was conducted using a digital densitometer (Mettler Toledo, MS104S). The equipment calculated the apparent density using the weight of samples in air and the weight of samples in water, according to the following equation:

$$\rho_m = \frac{A}{A-B}(\rho_L - d) + d \quad \text{Equation 3.1}$$

where  $\rho_m$ ,  $\rho_L$ ,  $d$ ,  $A$ , and  $B$  are measured density of a sample, density of water, density of air ( $\sim 0.001 \text{ g/cm}^3$ ), weight of a sample in air, and weight of a sample in water, respectively. The Archimedes' method gives us precise results when the sample is  $>92\%$  dense but is inaccurate less dense samples.

### 3.2.2 Theoretical density

Theoretical density is calculated when it is presumed that atoms/ions in the solid body are packed ideally. Theoretical densities in this project were calculated using the following equation:

$$\rho_{th} = \frac{Mn}{N_A V_{cell}} \quad \text{Equation 3.2}$$

where  $\rho_{th}$  is theoretical density,  $M$  is molecular weight of the substance,  $n$  is number of formula units per unit cell,  $N_A$  is Avogadro number ( $6.022141 \times 10^{23} \text{ mol}^{-1}$ ),  $V_{cell}$  is volume of unit cell. In this project,  $V_{cell}$  was calculated using the lattice parameters extracted from X-ray diffraction data set.

### 3.2.3 Relative density

Relative density is the ratio of measured to the theoretical density. It can be used as an indicator to know well ceramics are sintered. The relative density used in this project was calculated by the following equation:

$$\% \rho = \frac{\rho_m}{\rho_{th}} \times 100 \quad \text{Equation 3.3}$$

where  $\rho_p$  is relative density of a substance and  $\rho_m$  and  $\rho_{th}$  are a measured and theoretical density, respectively.

### 3.3 Structural and microstructural analysis

#### 3.3.1 X-ray diffraction (XRD)

XRD techniques has been used to determine or confirm crystal structure of target substances for over 100 years since Max Theodor Felix von *Laue* discovered the phenomenon. The wavelength of X-radiation is  $\sim 0.1$  nm which is on the same order as the spacing of atoms within typical crystal structures. The relationship between the incident wavelength and atomic spacings is given by Bragg's Law:

$$n\lambda = 2d \sin \theta \quad \text{Equation 3.4}$$

where  $n$  is a positive integer,  $\lambda$  is the wavelength of the incident wave,  $d$  is the inter planer spacing, and  $\theta$  is the angle of the diffraction.

X-rays are generated when matter is bombarded by high energy particles/photons. Cr, Fe, Cu, Mo, and Ag are often used as the source of X-rays. Continuous characteristic radiation (specific wavelength) is produced in this manner and it is the latter which is used to generate the X-rays in diffractometers. In this project, all measurements were carried out on powder (finely ground in a pestle and mortar) using a D2 Phaser (Bruker) equipped with  $\text{CuK}_\alpha$  ( $\lambda = 1.5418 \text{ \AA}$ ) source operated at 40 kV and 30 mA.  $\text{K}_\beta$  was filtered using Ni plate.

Phase analysis was conducted initially by comparison with standard traces in the International Center for Diffraction Data (ICDD) base. Lattice parameters were calculated using WinXpow software, utilizing a least square method and measured data were calibrated against standard Si powder. For more precise determination of the phase assemblage, Rietveld method was carried out using the software, the General Structure Analysis System (GSAS) package. In the Rietveld method, the least square refinements are carried out until the best fit is acquired between the measured powder diffraction pattern and calculated pattern based on the simultaneously refined models for the crystal structure, diffraction optics effects, instrumental factors, and other specimen characteristics.<sup>105</sup>

### 3.3.2 Scanning electron microscopy (SEM)

Scanning electron microscopes make use of the interaction between highly accelerated electron beam and the atoms within the specimen.<sup>106</sup> There are several types of signal emitted from the interaction including: secondary electrons (SE); back scattering electrons (BSE) and characteristic X-ray as shown in Fig. 3.2. The intensity of signals is affected by the weight averaged atomic number of the dwell point. The larger the weight averaged atomic number the brighter the contrast at the dwell point and vice versa. In addition, the intensity of the signal is strongly affected by the shape of the dwell point such as edges or points where the intensity of the signal emitted is greatly enhanced. Therefore, the surface of the samples needs to be as flat as possible to qualitatively determine the composition of the target area using image contrast. Accelerating voltage of electron beam can be increased to excite a greater volume of materials but the depth of penetration also increases which can obscure surface features. While secondary electrons are low energy (50 eV) electrons formed by inelastic scattering, backscattered electrons are high energy electrons (>50 eV) from the primary incident beam ejected back out from the sample. As the intensity of BSE is affected by the weight of atoms more strongly than that of SE, BSE images are often used to determine qualitative compositional information. In addition, the intensity of BSE are influenced by crystal orientation. Therefore, BSE can be used to study the domain structure of ferroelectric materials. Energy dispersive X-ray Spectroscopy (EDS or EDX) is quantitative chemical analysis available on most SEMs.<sup>107</sup> Characteristic X-rays are generated when an ejected electron in the inner shell of an atom is replaced by an electron from an outer shell. Elements with atomic number 4 (Be) to 92 (U) can be detected but the data reliability of light elements ( $Z < 10$ ) is debatable. For heavier elements, a precision (defined as  $2\sigma$  confidence level) of better than  $\pm 1\%$  (relative) is achieved provide adequate standards are available and the necessary corrections for absorption and fluorescence carried out. Spatial resolution depends on the condition of the incident beam, working distance between the electron gun and the sample, and the kinds of material and the density which controls the electron penetration, typically 3 to 10  $\mu\text{m}$  in bulk samples.

Ceramic microstructures were investigated using a Phillips, XL30 SEM equipped with

a BSE and EDS detector (Oxford instruments). The surfaces of the samples were ground and mirror polished using wet abrasive paper. Samples were further polished using diamond abrasives in a water based Diamond lubricant (MetPrep Ltd.). The polished samples were coated by carbon using a carbon coater (“SpeediVac”™, Coating Unit, Model: 12E6/1598, Edwards High Vacuum Ltd.) to prevent the sample from being charged.

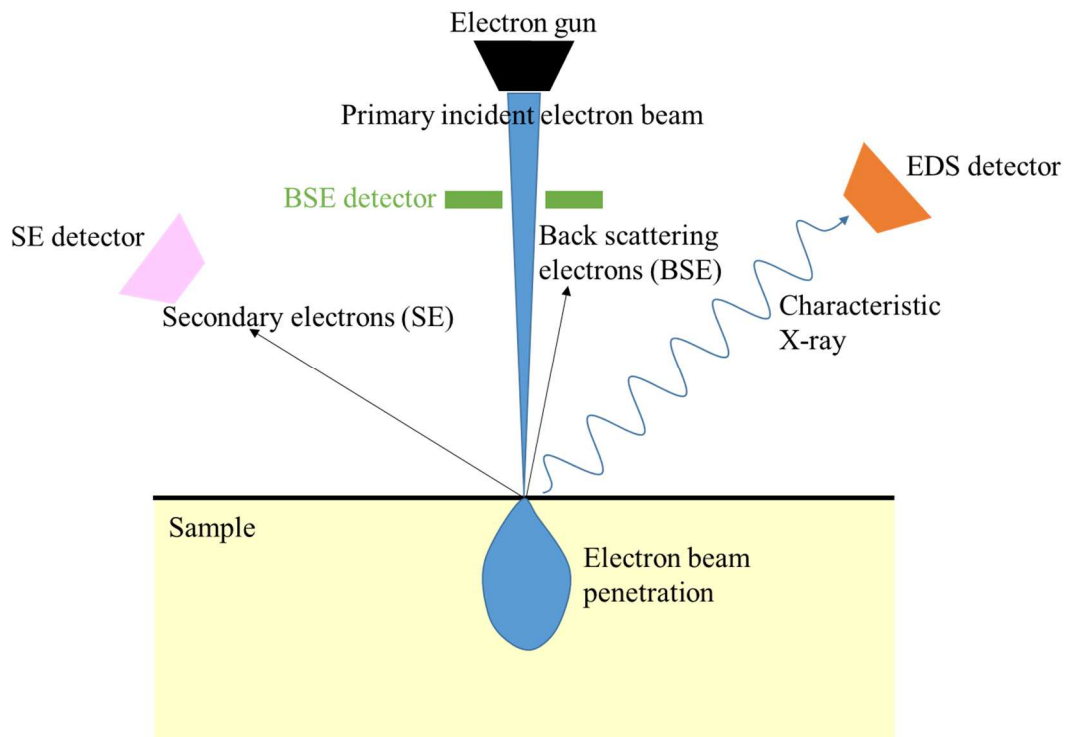


Fig. 3. 2 Schematic of scanning electron microscope.

### 3.3.3 Transmission electron microscope (TEM)

Transmission electron microscope (TEM) has higher spatial resolution than SEM.<sup>106</sup> due to the high accelerating voltages ( $\geq 100$  kV) wavelength and the commensurately smaller electron wavelength ( $0.0370 \text{ \AA}$  at 100 keV), which is smaller than the space between atoms and hence atomic columns can be resolved. Within this study only conventional microscopy has been used, exploiting bright field imaging dark field imaging techniques In bright field imaging mode, the directly transmitted (un-diffracted) electron beam is used to form an image but an objective aperture blocks strongly diffracting beams and contrast is induced between weakly and strongly diffracting regions (diffraction contrast).

In dark field imaging mode, a diffracted beam is used (highlighted by the objective aperture) to form the image and hence strongly diffracting regions appear bright.

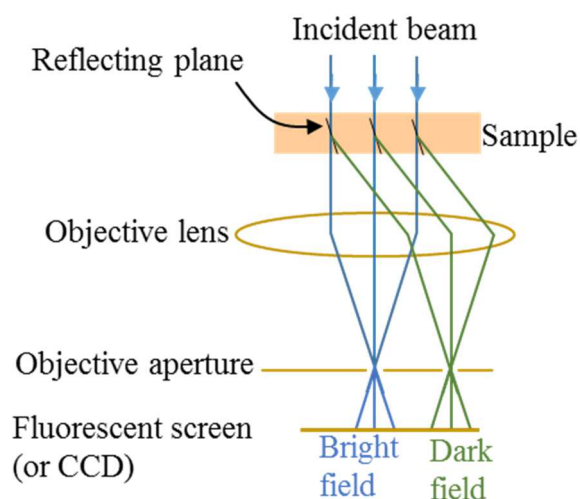


Fig. 3. 3 Schematic of transmission electron microscope.

In this project, TEM were performed using a either a JEOL 2010 or R005 TEM (JEOL) operating at 200 and 300 kV, respectively. The samples were prepared by grinding and polishing the ceramic to  $<30 \mu\text{m}$  followed by ion beam milling using a GATAN precision ion polishing system (PIPS) II (GATAN) to electron transparency. All the data acquired were conducted by Dr. Ali Mostaed.

### 3.4 Piezoelectric and Polarization measurements

Piezoelectric and polarization characterisations can be classified by the magnitude of application of electric field. Low field measurements include planar electromechanical coupling factor ( $k_p$ ), mechanical quality factor ( $Q_m$ ), and piezoelectric coefficients  $d_{33}$  whereas high field measurements are typically associated with strain and polarization.

#### 3.4.1 Low field measurements (Resonance method)

$\epsilon_r$  does not vary much from dc to microwave frequencies in good linear dielectrics. However, there is a strong frequency dependence of the  $\epsilon_r$  in ferroelectrics, especially in poled

piezoelectric materials, which is called mechanical resonance. At resonance, the material can be viewed as an equivalent circuit which consists of the following electric components, reactance ( $L_1$ ), capacitance ( $C_0$  and  $C_1$ ), and resistance ( $R_1$ ) as shown in Fig. 3.4.  $C_0$  is the capacitance in the absence of mechanical deformation at the frequency of the resonance under consideration.<sup>16</sup>

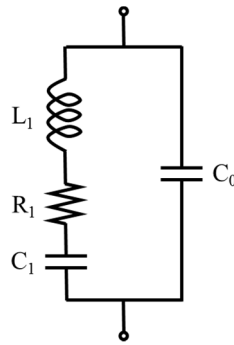


Fig. 3. 4 Equivalent circuit for a piezoelectric body near a fundamental resonance.

Although resistance is independent of frequency, reactance of inductor ( $X_L$ ) and capacitor ( $X_C$ ) depend on frequency.  $X_L$  and  $X_C$  are defined by:

$$X_L = 2\pi fL \quad \text{Equation 3.5}$$

$$X_C = \frac{1}{2\pi fC} \quad \text{Equation 3.6}$$

When  $X_L = X_C$ , the impedance shows a minimum value, the state is resonance and the frequency  $f_r$  is called resonant frequency. In addition, there is an anti-resonant frequency  $f_a$  where the impedance shows maximum at higher frequency than  $f_r$  as shown in Fig. 3.5. Anti-resonance is opposite phenomenon to resonance and therefore the vibration of the body becomes minimum.

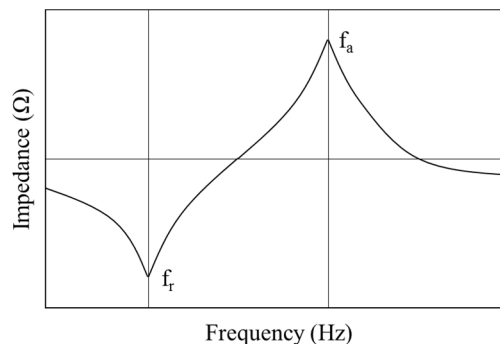


Fig. 3. 5 Typical impedance curve for piezoelectric vibrator.

The values of  $f_r$  and  $f_a$  are strongly related to piezoelectric properties. Several different piezoelectric vibrational mode are shown in Fig. 3.6. In this project,  $k_p$  (radial mode) and  $d_{33}$

(longitudinal length mode) were evaluated as piezoelectric parameters.

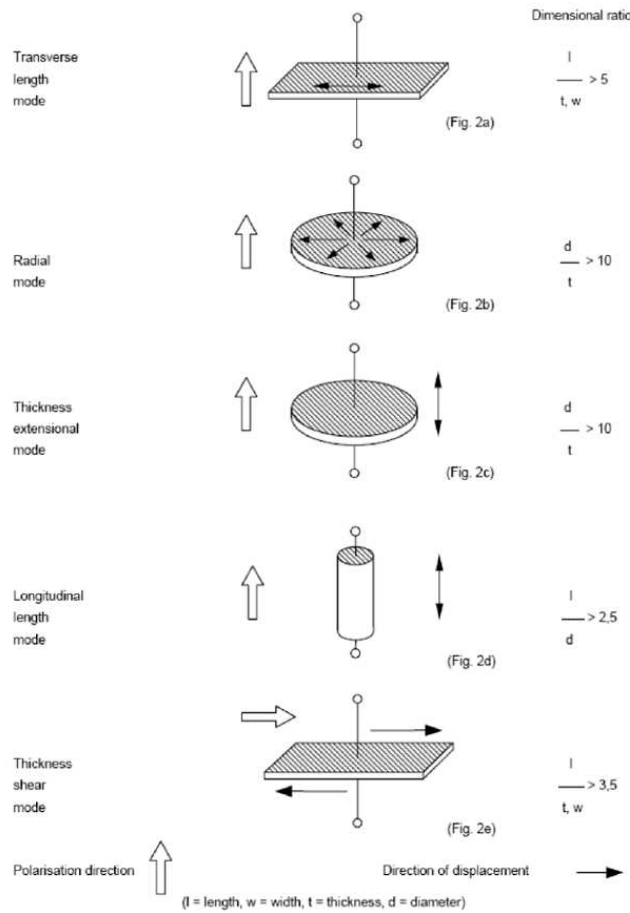


Fig. 3. 6 Typical vibration modes in various piezoelectric components.

Coupling coefficients of a piezoelectric material ( $k$ ) are an indicator of the effectiveness with which piezoelectric materials convert electrical energy into mechanical energy, or vice versa. Typical values of  $k$  are 0.10 for quartz, 0.4 for barium titanate ceramics, 0.5-0.7 for PZT ceramics, and as much as 0.9 for Rochelle salt at its  $T_C$  (24 °C).<sup>16</sup> Planar electromechanical coupling factor  $k_p$  used in this project were calculated from the following equation,<sup>28</sup>

$$\frac{1}{k_p^2} = 0.395 \times \frac{f_r}{f_a - f_r} + 0.574 \quad \text{Equation 3.7}$$

$Q$  is a dimensionless parameter that indicates the energy losses within a resonant element. For piezoelectric components in resonance, the mechanical quality factor  $Q_m$  characterises the amplitude and the sharpness of the resonance peaks. In ferroelectric ceramics,  $Q_m$  is related to the motion of domain walls. In this project, mechanical quality factor  $Q_m$  was calculated from the following equation,<sup>108</sup>

$$Q_m = \frac{1}{2\pi f_r C_1 R_1} \quad \text{Equation 3.8}$$

The values of  $f_a$ ,  $f_r$ ,  $C_1$ , and  $R_1$  were measured using an impedance analyser (Agilent, 4294A, 40 Hz to 110 MHz).

### 3.4.2 Low field measurements (Berlincourt method)

$d_{33}$  was measured by Berlincourt method which is a relatively simple measuring technique. The sample is clamped by the metal rods and a varying force is applied ( $<1$  N) at a frequency of  $\sim 100$  Hz and the voltage output measured, which is then used to calculate  $d_{33}$ . Although the testing frequency is much lower than resonance method, it is high enough to complete the test within few seconds.<sup>28</sup> In this project,  $d_{33}$  was measured using a  $d_{33}$  meter (Piezotest, Model PM300) with a dynamic force of 0.25 N with frequency of 110 Hz shortly after samples were poled under optimal DC electric field at optimal temperature for 20 min.

### 3.4.3 High field method

Polarization was measured by  $D/E$  hysteresis loops, where  $D$  is electric displacement and  $E$  is an applied electric field. A uniform piezoelectric material is considered to lie between two metal plates under some electric field as shown in Fig. 3.7.

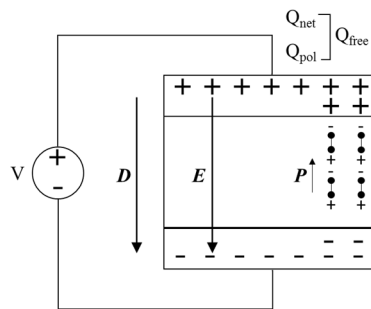


Fig. 3. 7 Electric behaviour of a parallel plate capacitor with a dielectric medium.

Charge  $Q$  is created on the plates, which is described using  $Q_{\text{free}}$ ,  $Q_{\text{net}}$ , and  $Q_{\text{pol}}$  which are: the charge on the conducting plates, related to the electric displacement  $D$ ; net charge on the conducting plates, related to the electric field  $E$  and charge on the conducting plates that compensates the polarization of the dielectric medium, respectively. The relation between them

is described as follows;

$$Q_{pol} = Q_{free} - Q_{net} \quad \text{Equation 3.9}$$

Using these equations, polarization is described as follows;

$$\mathbf{P} = \epsilon_0 \mathbf{E} - \mathbf{D} \quad \text{Equation 3.10}$$

Where  $\epsilon_0$  is permittivity of free space,  $8.854 \times 10^{-12}$  [F/m]. The electric displacement (the electric charge per unit area) [C/m<sup>2</sup>] are as follows;

$$D = \frac{Q}{A} \quad \text{Equation 3.11}$$

where  $A$  is area of the plates. The system used in this project determines  $Q$  on the plates by detecting a current  $I$  through a sample by feedback method.

Strain can be measured at the same time with polarization because strain is coupled with polarization. There are several measurement techniques of strain as follows: capacitance probe; fiber optic probe; strain gauge and laser interferometry. In this project, laser interferometry was used because the measurement resolution is the highest among the four procedures. This technique is designed based on Michelson interference where the displacement of a sample is measured using the path difference between a reference beam (fixed path) and a beam reflected from the sample.<sup>109</sup> Polarization and electric field-induced strain (SE) was measured at 1 Hz using a triangular wave form up to 10 kV/cm from room temperature to 175°C in silicone oil using a ferroelectric tester (AixACCT, TF 2000). This equipment can control the temperature around the sample from room temperature to 300°C. When measuring the temperature dependence of polarization and strain, the measurements were conducted at least 5 minutes after target temperature was attained. All the measurements were implemented at Christian Doppler Laboratory on Advanced Ferroic Oxides, Sheffield Hallam University, Sheffield in collaboration with Dr. Antonio Feteira.

## 3.5 Electrical measurements

### 3.5.1 Relative permittivity ( $\epsilon_r$ ) and dielectric loss ( $\tan\delta$ )

$\epsilon_r$  can be calculated from the capacitance and the geometric parameters of the sample

using:

$$\epsilon_r = \frac{Cd}{\epsilon_0 A} \quad \text{Equation 3.12}$$

where  $C$  is the capacitance (F),  $d$  is the thickness of the sample (m),  $A$  is the area of the sample ( $\text{m}^2$ ),  $\epsilon_0$  is permittivity of vacuum,  $8.854 \times 10^{-12}$  (F/m), and  $\epsilon_r$  is relative permittivity or dielectric constant.

Capacitance and dielectric loss ( $\tan\delta$ ) can be measured using LCR meter ( $L$  = Inductance,  $C$  = Capacitance, and  $R$  = Resistance). There are many ways in principal to measure impedance. The LCR meter used in this project works by the “Automatic balancing bridge method” shown in Fig. 3.8. The  $I$ - $V$  converter operates to make the current  $I_x$  flowing through the device under test (DUT) balance with the current  $I_r$  which flows through the range resistor ( $R_r$ ), i.e.,  $I_x = I_r$ . The potential at the low point is kept at zero volts, which is called a virtual ground. The impedance of DUT is calculated using the voltage measured at the high terminal ( $V_x$ ) and across  $R_r$  ( $V_r$ ) using the following formula.

$$Z_x = \frac{V_x}{I_x} = R_r \frac{V_x}{V_r} \quad \text{Equation 3.13}$$

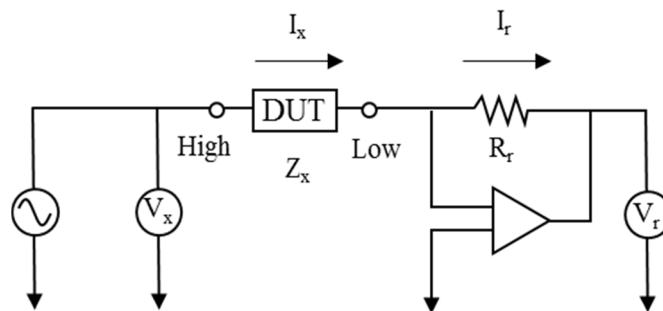


Fig. 3. 8 Schematic diagram of Automatic Balancing Bridge.

As the phase angle of  $V_x$  and  $V_r$  are also recorded, the capacitance and  $\tan\delta$  for DUT are calculated at the same time.

Temperature dependence of relative permittivity and  $\tan\delta$  were measured at 10 kHz using a LCR meter (HP, 4284A) connected to a computer through GP-IB interface. The sample was loaded in a conductivity jig where the sample is put between two electrode pins. The jig

was loaded in the tube type furnace with a thermocouple the tip which was placed within 5mm of the sample.

### 3.5.2 Impedance spectroscopy

Impedance spectroscopy is very useful technique to reveal the electric properties of dielectric materials using AC fields. It is well known that various dielectric responses of a material to applied voltages as a function of frequency can be associated with different kinds of processes at the atomic and microstructural level. Impedance spectroscopy in this study was conducted using an Impedance analyser (LCR meter) with automatic balancing bridge as described in the preceding section.

Measured complex impedance ( $Z$ ) can be converted to three other formalisms, the electric modulus ( $M$ ), the admittance ( $A$ ), and the permittivity ( $\epsilon$ ). These are interrelated as follows;

$$\left. \begin{aligned} Y &= \frac{1}{Z} = \frac{1}{Z' - jZ''} = \frac{Z' + jZ''}{(Z')^2 + (Z'')^2} \\ Y' &= \frac{Z'}{(Z')^2 + (Z'')^2} \\ Y'' &= \frac{Z''}{(Z')^2 + (Z'')^2} \end{aligned} \right\} \text{Equation 3.14}$$

$$\left. \begin{aligned} M &= j\omega C_0 Z = j\omega C_0 (Z' - jZ'') = \omega C_0 Z'' + j\omega C_0 Z' \\ M' &= \omega C_0 Z'' \\ M'' &= \omega C_0 Z' \\ C_0 &= \epsilon_0 \frac{A}{d} \end{aligned} \right\} \text{Equation 3.15}$$

$$\left. \begin{aligned} \epsilon &= \frac{1}{M} = \frac{1}{M' + jM''} = \frac{1}{\omega C_0} \cdot \frac{Z'' - jZ'}{(Z')^2 + (Z'')^2} \\ \epsilon' &= \frac{1}{\omega C_0} \cdot \frac{Z''}{(Z')^2 + (Z'')^2} \\ \epsilon'' &= \frac{1}{\omega C_0} \cdot \frac{Z'}{(Z')^2 + (Z'')^2} \end{aligned} \right\} \text{Equation 3.16}$$

where  $Z'$  and  $Z''$  are real and imaginary parts of complex impedance, respectively.  $\omega$  is the

angular frequency  $2\pi f$ ,  $C_0$  is the vacuum capacitance of the measuring cell, and  $j$  is  $\sqrt{-1}$ .

Although an ideal dielectric should be described as a capacitor, leakage currents exist within the material. Therefore, the equivalent circuit for real ceramics is described in Fig. 3.9 where the resistance component is introduced in parallel. When the ceramics is ideally made, the complex impedance or Cole-Cole plot gives a single semi-circle (Fig. 3.9).

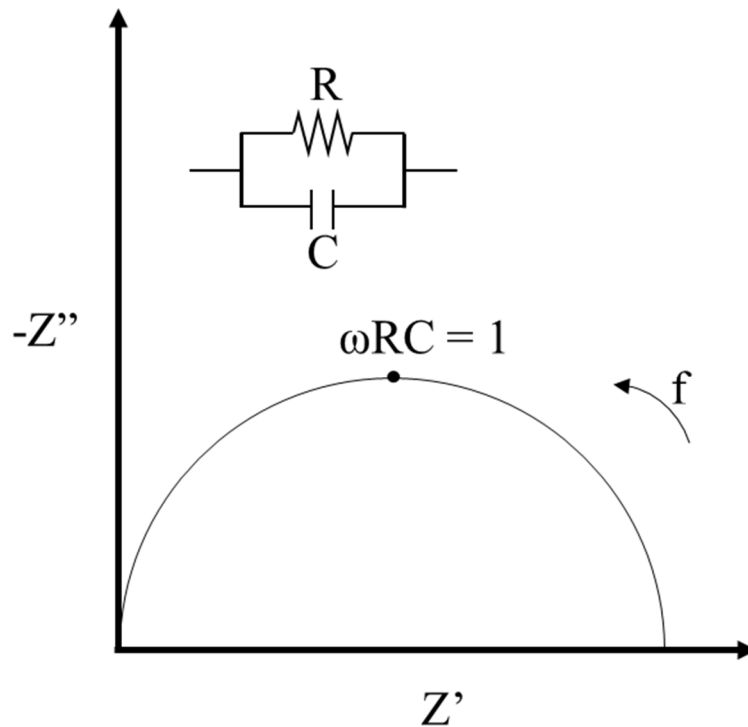


Fig. 3. 9 Possible equivalent circuit of an uniform dielectric and the complex impedance plot.

If the ceramics consists of several components, for example a grain component and a grain boundary component, the equivalent circuit needs to connect two RC components in series shown in Fig. 3.10,

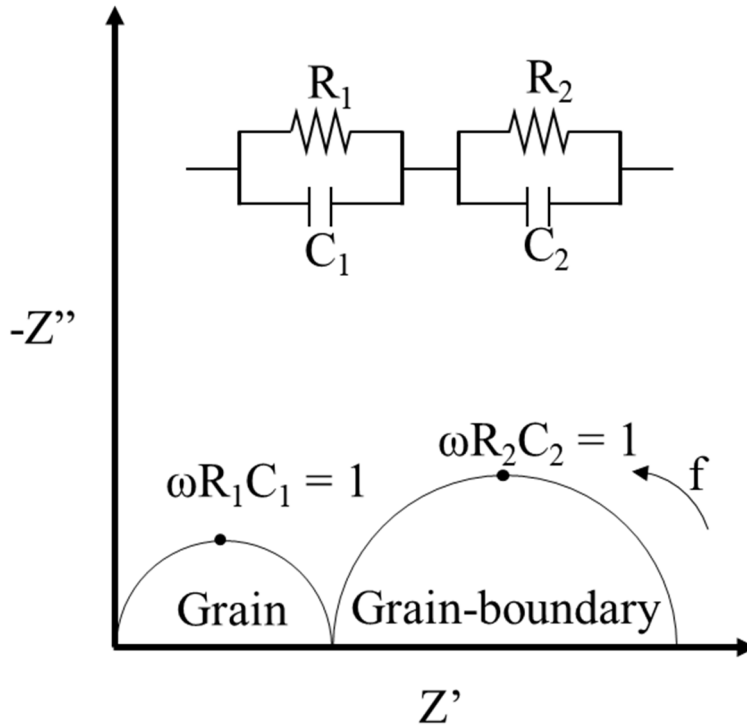


Fig. 3. 10 Possible equivalent circuit of the dielectric consisting of two types of components and the complex impedance plot.

where  $R_1$  and  $C_1$  are the resistance and the capacitance of the grain, respectively,  $R_2$  and  $C_2$  are the resistance and the capacitance of the grain-boundary, respectively.<sup>110,111</sup> Since the resistance of grain-boundaries is generally higher than those of grains, the complex impedance plot of the ceramics is often depicted like Fig. 3.10. However, impedance ( $Z$ ) often shows a single semi-circle in the measurements of ceramics because the impedance response is dominated totally by the parallel RC element with the larger resistance  $R_2$ . On the other hand,  $M^*$  is dominated by the smallest capacitance in the equivalent circuit and is therefore used to extract information about the bulk component. Impedance  $Z$  is measured directly by an impedance analyser and capacitance calculated from the relation  $\omega RC = 1$ . DC electrical conductivity can be calculated according to the relation given below,

$$\sigma = \frac{1}{Z'} \times \frac{t}{A} \quad \text{Equation 3.17}$$

where  $\sigma$  is DC electrical conductivity,  $Z'$  is low frequency intercept of the large arc in the  $Z^*$  plots,  $t$  and  $A$  are the thickness and the area of the sample.

As the DC electrical conductivity of the material is a thermally activated process obeying

Arrhenius behaviour, the activation energy can be calculated using:

$$\sigma = \sigma_0 e^{\frac{E_a}{k_B T}} \quad \text{Equation 3.18}$$

where  $\sigma_0$  is pre-exponential component,  $E_a$  is activation energy,  $k_B$  is Boltzmann constant ( $8.6173324 \times 10^{-5} \text{ eVK}^{-1}$ ), and  $T$  is temperature.<sup>27</sup> Equation 3. 18 can be converted as follows,

$$E_a = m \times k_B \quad \text{Equation 3.19}$$

where  $m$  is slope of the plots of  $\text{Ln}(\sigma_{dc})$  versus  $1000/T$ .

Samples were loaded in a conductivity jig and placed between two electrode pins, similar to that used to measure the temperature dependence of  $\epsilon_r$ . The jig was loaded in the tube type furnace with a thermocouple tip within 5mm of the sample. Impedance was measured from 200°C to 500°C using HP4192A (5 Hz – 13 MHz) precision LCR meter. The applied voltage was 0.1 V and the data corrected for geometric factor  $A/t$ , where  $A$  and  $t$  are area and thickness of the sample, using ZView™ software (Scribner Associates Inc, USA).

## Chapter 4: Processing of Materials

### 4.1 Introduction

The ceramics samples studied in this project were made by a solid-state synthesis method. In this section, the ceramic preparation procedure is described and explained from the characterisation of raw materials to the sintering method used to densify ceramics. Table 4.1 shows the list of the composition investigated in this project. Composition No.4 was used for the prototype manufacturing of multilayer actuator described in chapter 8.

Table 4. 1 List of composition studied in this project.

No.	Composition	Remarks
Chapter 5		
1	0.05BiFe( <i>Me</i> )O <sub>3</sub> -0.25BaTiO <sub>3</sub> -0.70BiFeO <sub>3</sub>	<i>Me</i> = Y, Sc <sub>1/2</sub> Y <sub>1/2</sub> , Mg <sub>2/3</sub> Nb <sub>1/3</sub> , Sc, Zn <sub>2/3</sub> Nb <sub>1/3</sub> , Zn <sub>1/2</sub> Ti <sub>1/2</sub> , Ga, and Al
Chapter 6		
2	0.05Bi(Mg <sub>2/3</sub> Nb <sub>1/3</sub> )O <sub>3</sub> -(0.95- <i>x</i> )BaTiO <sub>3</sub> -( <i>x</i> )BiFeO <sub>3</sub>	<i>x</i> = 0.55, 0.60, 0.63, 0.65, 0.70, and 0.75
Chapter 7		
3	0.05BiScO <sub>3</sub> -(0.95- <i>x</i> )BaTiO <sub>3</sub> -( <i>x</i> )BiFeO <sub>3</sub>	<i>x</i> = 0.55, 0.60, 0.625, 0.65, and 0.70
Chapter 8		
4	0.05Bi(Mg <sub>2/3</sub> Nb <sub>1/3</sub> )O <sub>3</sub> -0.63BaTiO <sub>3</sub> -0.32BiFeO <sub>3</sub> (One of the compositions, no. 2)	Multilayer actuator

### 4.2 Raw materials

#### 4.2.1 Raw materials

The raw materials used in this project are all commercially available powders. Table 4.2 shows the purity and the supplier of each raw material. No attempt however, was made to characterise the nature and type of impurities associated with each raw material.

Table 4. 2 List of raw materials used in this project.

No.	Chemical	Purity (%)	Supplier
1	Bi <sub>2</sub> O <sub>3</sub>	99.9	Acros Organics
2	Fe <sub>2</sub> O <sub>3</sub>	99	Sigma Aldrich
3	BaCO <sub>3</sub>	99.9	Sigma Aldrich
4	TiO <sub>2</sub>	99.9	Sigma Aldrich
5	MgO	99	Sigma Aldrich
6	Nb <sub>2</sub> O <sub>5</sub>	99.5	Alfa Aesar
7	Y <sub>2</sub> O <sub>3</sub>	99.99	Alfa Aesar
8	Sc <sub>2</sub> O <sub>3</sub>	99.995	Stanford Materials
9	ZnO	99.9	Sigma Aldrich
10	Ga <sub>2</sub> O <sub>3</sub>	99.99	Stanford Materials
11	Al <sub>2</sub> O <sub>3</sub>	99.8	Aldrich Chemical Company

#### 4.2.2 Drying of raw materials

Properties of ceramics can be strongly affected by the imbalance in the stoichiometry. Li et al<sup>112</sup> reported that only 1% deviation of Ti concentration from the stoichiometry makes a huge difference to the electrical conductivity in Na<sub>0.5</sub>Bi<sub>0.5</sub>TiO<sub>3</sub> ceramics. Therefore, accurately weighing raw materials is extremely important in fabricating ceramics. Since the powders are usually stored in air, the absorption of moisture and CO<sub>2</sub> results in the formation surface hydroxide, carbonates and hydrocarbonates.<sup>113</sup> Their amount depends on the kind of material, humidity, particle size, and the method of storage. Hence, raw materials are dried at high temperature to eliminate these contaminants. The drying temperature depends on the type of raw material. All the raw materials were heated at the required temperatures for at least 8 h and then cooled to 200°C, after which they were moved to sealed desiccator for cooling to room temperature. Since this drying process is normally conducted overnight, the temperature is kept at 200°C until weighing. Weighing was conducted as soon as possible after the raw materials were cooled. The drying temperatures of all the raw materials are shown in Table 4.3.

Table 4. 3 Drying temperatures of raw materials.

No.	Chemical	Drying temperature (°C)
1	Bi <sub>2</sub> O <sub>3</sub> , BaCO <sub>3</sub>	180
2	Fe <sub>2</sub> O <sub>3</sub> , ZnO, Ga <sub>2</sub> O <sub>3</sub>	600
3	TiO <sub>2</sub> , MgO, Nb <sub>2</sub> O <sub>5</sub> , Y <sub>2</sub> O <sub>3</sub> , Sc <sub>2</sub> O <sub>3</sub> , Al <sub>2</sub> O <sub>3</sub>	900

### 4.2.3 Phase analysis of raw materials

To confirm the crystal structure of raw materials, they were examined after drying using XRD. XRD patterns match with Powder Diffraction Files for Bi<sub>2</sub>O<sub>3</sub>, Fe<sub>2</sub>O<sub>3</sub>, BaCO<sub>3</sub>, TiO<sub>2</sub>, MgO, Nb<sub>2</sub>O<sub>5</sub>, Y<sub>2</sub>O<sub>3</sub>, Sc<sub>2</sub>O<sub>3</sub>, ZnO, Ga<sub>2</sub>O<sub>3</sub>, Al<sub>2</sub>O<sub>3</sub>, respectively as shown in Fig. 4.1 and 4.2

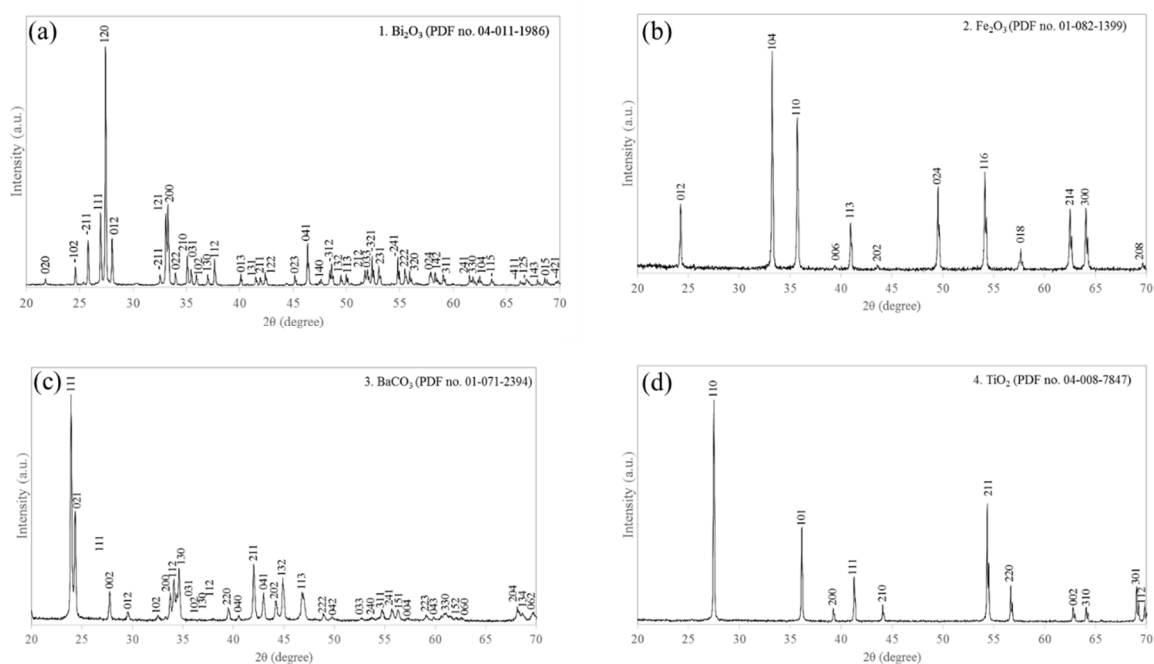


Fig. 4. 1 XRD patterns for raw materials of (a) Bi<sub>2</sub>O<sub>3</sub>, (b) Fe<sub>2</sub>O<sub>3</sub>, (c) BaCO<sub>3</sub> and (d) TiO<sub>2</sub>, matched PDF card nos. 04-011-1986, 01-082-1399, 01-071-2394, 04-008-7847 of Bi<sub>2</sub>O<sub>3</sub>, Fe<sub>2</sub>O<sub>3</sub>, BaCO<sub>3</sub>, TiO<sub>2</sub>, respectively.

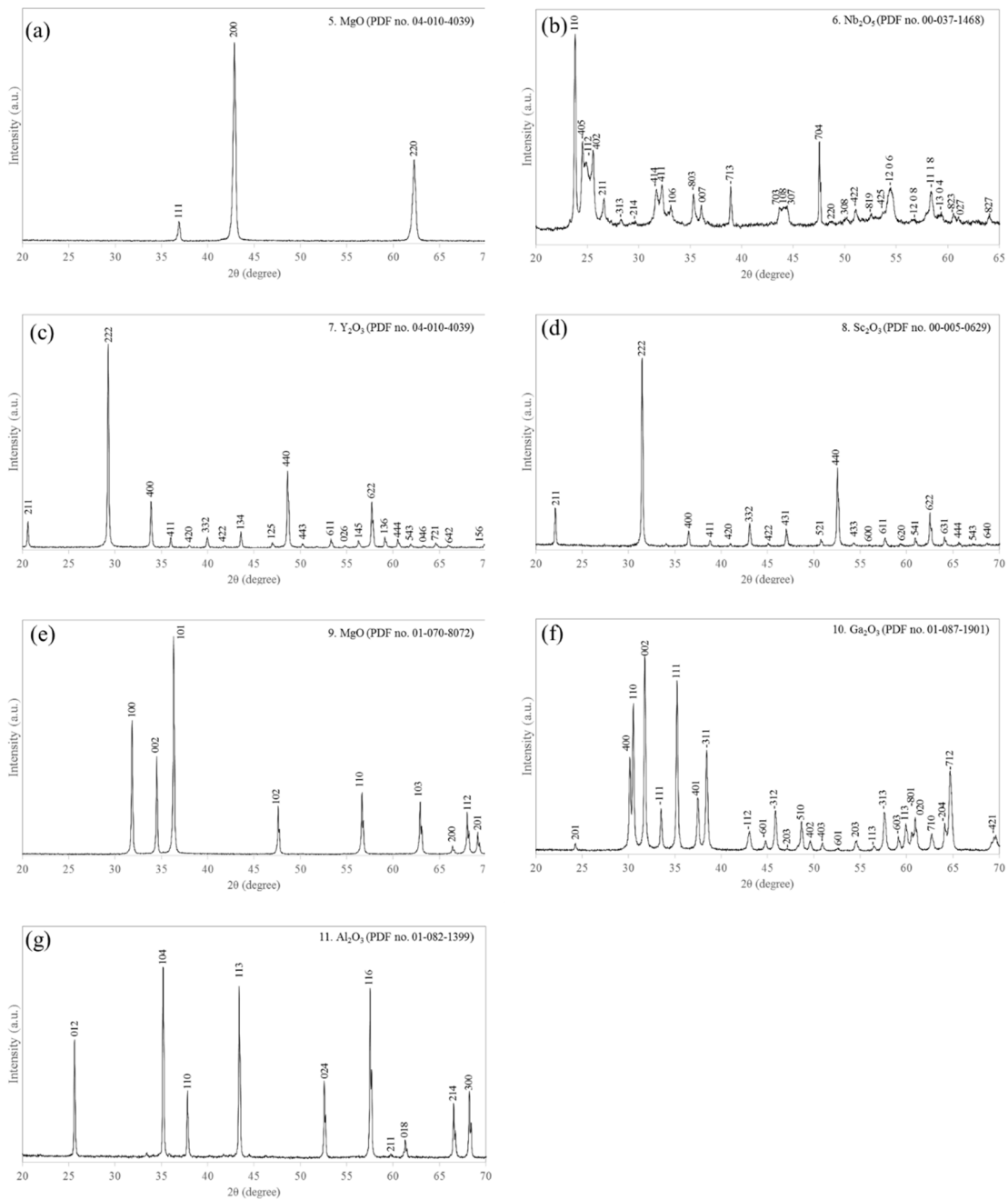


Fig. 4. 2 XRD patterns of (a) MgO, (b) Nb<sub>2</sub>O<sub>5</sub>, (c) Nb<sub>2</sub>O<sub>5</sub>, (d) Y<sub>2</sub>O<sub>3</sub>, (e) Sc<sub>2</sub>O<sub>3</sub>, (f) ZnO, (g) Ga<sub>2</sub>O<sub>3</sub> and (h) Al<sub>2</sub>O<sub>3</sub> matched PDF card nos. 04-010-4039, 00-037-1468, 04-010-4039, 00-005-0629, 01-070-8072, 01-087-1901, 01-082-1309 of MgO, Nb<sub>2</sub>O<sub>5</sub>, Nb<sub>2</sub>O<sub>5</sub>, Y<sub>2</sub>O<sub>3</sub>, Sc<sub>2</sub>O<sub>3</sub>, ZnO, Ga<sub>2</sub>O<sub>3</sub>, Al<sub>2</sub>O<sub>3</sub>, respectively.

#### 4.2.4 Particle size analysis of raw materials

Particle size analysis was conducted using a laser diffraction measurement, as shown in Fig. 4.3. This method cannot tell the difference between a real single particle and the agglomerate. However, it is useful to determine quantitatively the trends in particle size and distribution. Fig. 4.3 shows that the mean particle size for all raw materials are within the same

order of magnitude from 1 –  $\mu\text{m}$ .

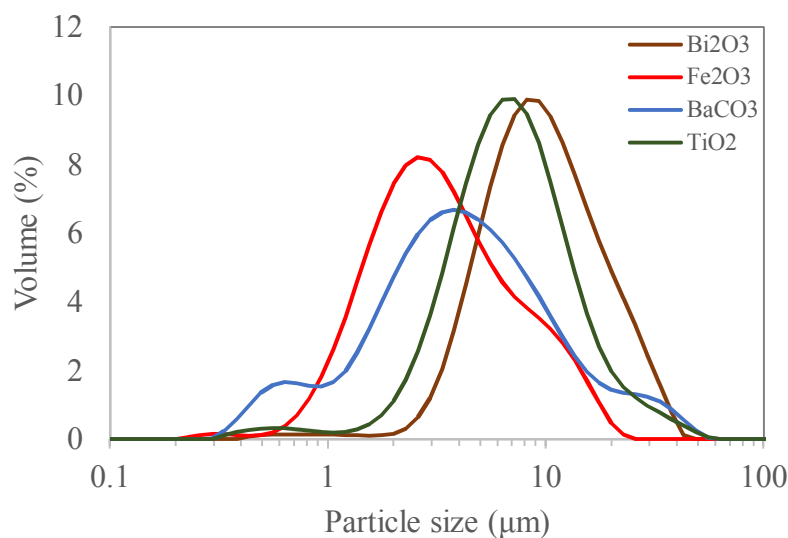


Fig. 4. 3 Particle size distribution of raw materials of BT-BF.

## 4.3 Ceramic processing

### 4.3.1 Powder weighing

As mentioned in 4.2.2, the stoichiometry of ceramics is extremely important, so that weighing of raw materials was carried out to  $\pm 1$  mg using a Precisa, 923M-202A balance shortly after drying. The amount of powder in a batch was fixed about 60 g so that every composition underwent the same process conditions for mixing and calcination.

### 4.3.2 Mixing and milling of powder

To obtain reproducible properties, it is critical to mix raw materials well enough to form a uniform distribution and to reduce the particle size to decrease diffusion distance for the reaction.<sup>27</sup> The milled particle diameter is proportional to the milling time as shown in Fig. 4.4.<sup>114</sup> However, milling for too long results in contamination due to degradation of the milling media. In this project, dried powders were attrition milled for 1 to 2 h at 300 rpm in a Union Processes attritor mill (Szegvari Attritor System, Union Process), using 3mm diameter yttria-stabilised zirconia media in isopropanol. The slurry was separated from the media and dried overnight at 80°C. XRD spectrum of all the samples showed that there were no ZrO<sub>2</sub> secondary

phases (Fig. 4.1 and fig. 4.2). The particle size distribution of dried and attrition milled raw materials are shown in Fig. 4.5. Each raw material was attrition milled prior to measuring the particle size and it was confirmed attrition milling reduced the particle size of all raw materials. However, for  $\text{Fe}_2\text{O}_3$ , larger particles were observed probably due to agglomeration during drying at  $600^\circ\text{C}$  for 8 h.

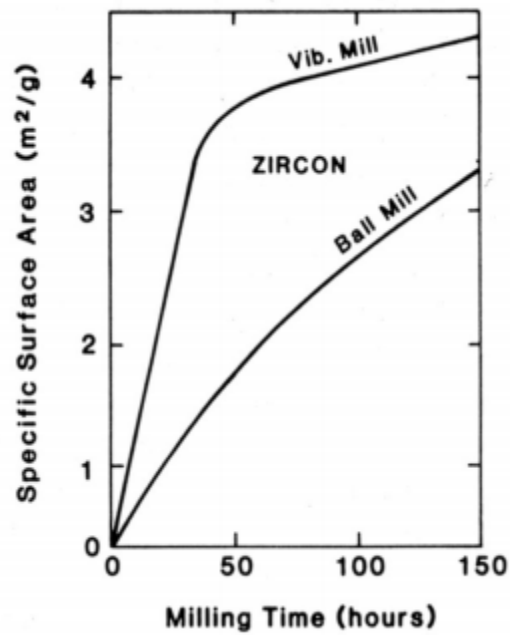


Fig. 4. 4 Specific surface area vs milling time.<sup>114</sup>

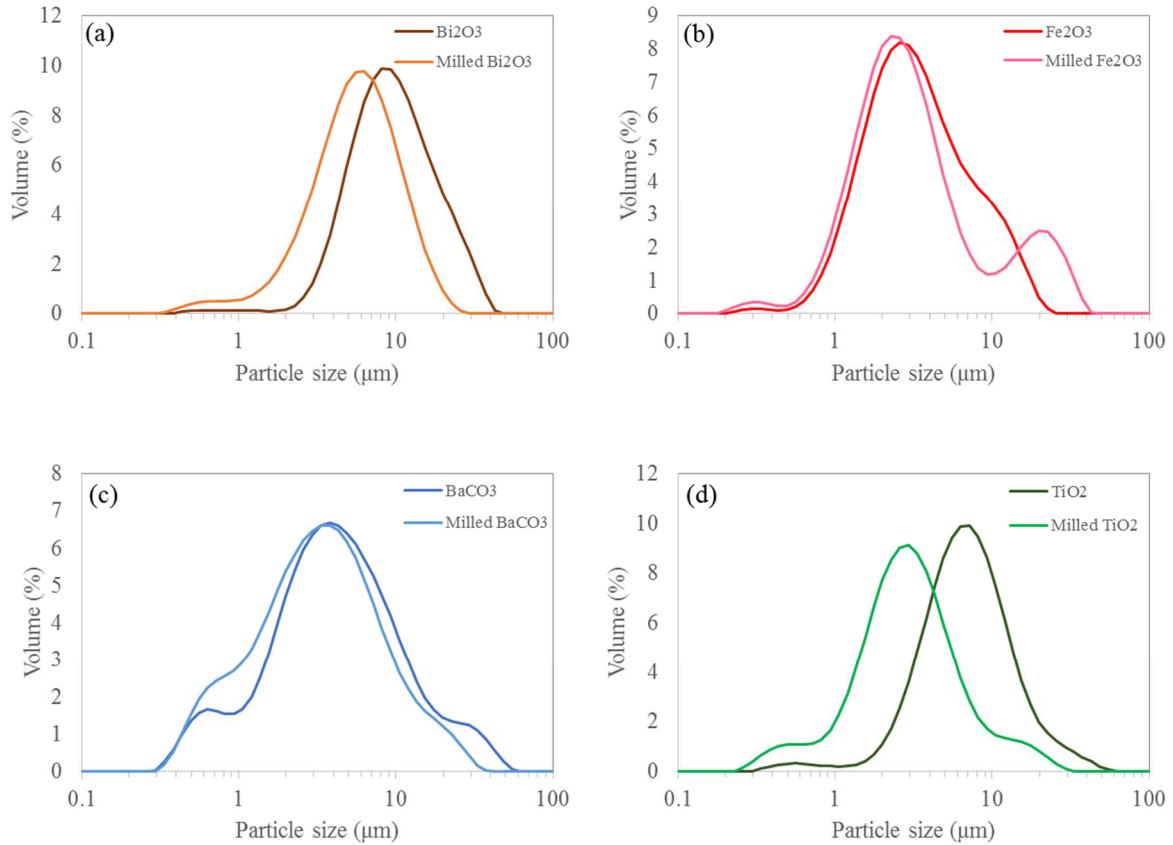


Fig. 4. 5 Particle size distribution before and after drying and attrition milling for raw materials, (a)  $\text{Bi}_2\text{O}_3$ , (b)  $\text{Fe}_2\text{O}_3$ , (c)  $\text{BaCO}_3$ , (d)  $\text{TiO}_2$ .

### 4.3.3 Calcination

The aim of calcination is to cause ions in the raw materials to diffuse into each other to make uniform powder of the desired crystal structure. However, in practice chemical gradients remain. These gradients are usually removed through re-milling and reheating at the sintering temperature, typically 2-300 °C higher than calcination.<sup>27</sup>

Many researchers have reported calcination of  $\text{BaTiO}_3$ - $\text{BiFeO}_3$  systems at 750 to 860°C.<sup>22, 115</sup> In this project, calcination was carried out for 2 h at 750 to 800°C. Calcination was conducted in an  $\text{Al}_2\text{O}_3$  crucible for 2 h with heating rate of 3.0°C/min in a muffle furnace. As a result, uniform and single-phase powders were obtained. The calcination temperatures of all samples are shown in Table 4.4. The particle size distribution of calcined and attrition milled powder for  $0.05\text{Bi}(\text{Mg}_{2/3}\text{Nb}_{1/3})\text{O}_3$ - $0.63\text{BiFeO}_3$ - $0.32\text{BaTiO}_3$  is shown in Fig. 4.6. The mean particle size is ~4 μm, approximately the same the raw materials.

Table 4. 4 Calcination temperature of all the composition in this project.

Composition	Calcination temperature (°C)
<b>Chapter 5</b>	
0.05BiFe( <i>Me</i> )O <sub>3</sub> -0.25BaTiO <sub>3</sub> -0.70BiFeO <sub>3</sub> ( <i>Me</i> = Mg <sub>2/3</sub> Nb <sub>1/3</sub> , Sc, Zn <sub>2/3</sub> Nb <sub>1/3</sub> , Zn <sub>1/2</sub> Ti <sub>1/2</sub> , Ga, and Al)	800
0.05BiFe( <i>Me</i> )O <sub>3</sub> -0.25BaTiO <sub>3</sub> -0.70BiFeO <sub>3</sub> ( <i>Me</i> = Y, Sc <sub>1/2</sub> Y <sub>1/2</sub> )	750
<b>Chapter 6</b>	
0.05Bi(Mg <sub>2/3</sub> Nb <sub>1/3</sub> )O <sub>3</sub> -(0.95- <i>x</i> )BaTiO <sub>3</sub> -( <i>x</i> )BiFeO <sub>3</sub> ( <i>x</i> = 0.55, 0.60, 0.63, 0.65, and 0.70)	800
0.05Bi(Mg <sub>2/3</sub> Nb <sub>1/3</sub> )O <sub>3</sub> -(0.95- <i>x</i> )BaTiO <sub>3</sub> -( <i>x</i> )BiFeO <sub>3</sub> ( <i>x</i> = 0.75)	750
<b>Chapter 7</b>	
0.05BiScO <sub>3</sub> -(0.95- <i>x</i> )BaTiO <sub>3</sub> -( <i>x</i> )BiFeO <sub>3</sub> ( <i>x</i> = 0.55, 0.60, 0.625, 0.65, and 0.70)	800
<b>Chapter 8</b>	
0.05Bi(Mg <sub>2/3</sub> Nb <sub>1/3</sub> )O <sub>3</sub> -0.63BaTiO <sub>3</sub> -0.32BiFeO <sub>3</sub>	800

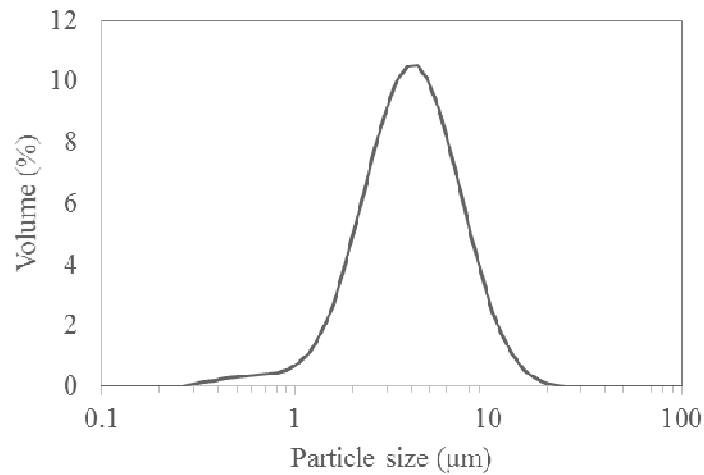


Fig. 4. 6 Particle size distribution of calcined and attrition milled powder for 0.05Bi(Mg<sub>2/3</sub>Nb<sub>1/3</sub>)O<sub>3</sub>-0.63BiFeO<sub>3</sub>-0.32BaTiO<sub>3</sub>.

### 4.3.4 Pressing into green compact

There are various types of geometric shaping techniques for ceramics as shown in table 4.5. In this project, dry-pressing for monolithic ceramics and tape casting (band-casting) and screen-printing for multilayer actuators were used. The calcined powder was further attrition milled and dried, as described in section of 4.3.2. The attrition milled powder was mixed with 0.5 wt% poly(vinyl alcohol) to prevent the compact from cracking. It was then dried, pulverized by using an agate pestle and mortar, and sieved through 250  $\mu\text{m}$  mesh.  $\sim 0.3$  g of powder was uniaxially pressed into a disk with a 10 mm diameter at 125 MPa to form a compact.

Table 4. 5 Feed materials for various shaping methods and the type of product.

Shaping method	Type of feed material	Type of shape
(1) Dry-pressing	Free-flowing granules	Small simple shapes
(2) Isostatic pressing	Fragile granules	Larger more intricate shapes
(3) Calendering; viscous plastic processing	Plastic mass based on an elastic polymer	Thin plates Simple shapes
(4) Extrusion	Plastic mass using a viscous polymer solution	Elongated shapes of constant cross-section
(5) Jiggering	Stiff mud containing clay	Large simple shapes
(6) Injection moulding	Organic binder giving fluidity when hot	Complex shapes
(7) Slip-casting	Free-flowing cream	Mainly hollow shapes
(8) Band-casting	Free-flowing cream	Thin plates and sheets
(9) Screen-printing	Printing ink consistency	thin layers on substrates

### 4.3.5 Sintering

Sintering or densification process generally consists of three steps which are (A) burning out binders, (B) densification, and (C) cooling, as shown in Fig. 4.7 and 4.8.<sup>27, 114</sup> In (A), temperature is increased slowly to burn out binders. If it is raised rapidly, a temperature gradient develops inside the green compact, which can cause cracking. In the (B), particles stick together and ions diffuse. This process begins through necking. Once full reaction has

occurred shrinkage of the compact takes, leading in principle to a dense body. During cooling (C), limited densification continues but most importantly if the ceramics are cooled rapidly, cracking may occur which lowers the mechanical integrity of the ceramics. Intentionally rapidly cooling ceramics from the sintering temperature is referred to as quenching. Quenching can retain the crystal structure or/and microstructure from the sintering temperature but from a commercial perspective, this process is not advisable for piezoelectrics which are subject to large electric fields and strains in applications. Fig. 4.7 (b) shows the schematic of sintering temperature profile used in this project.

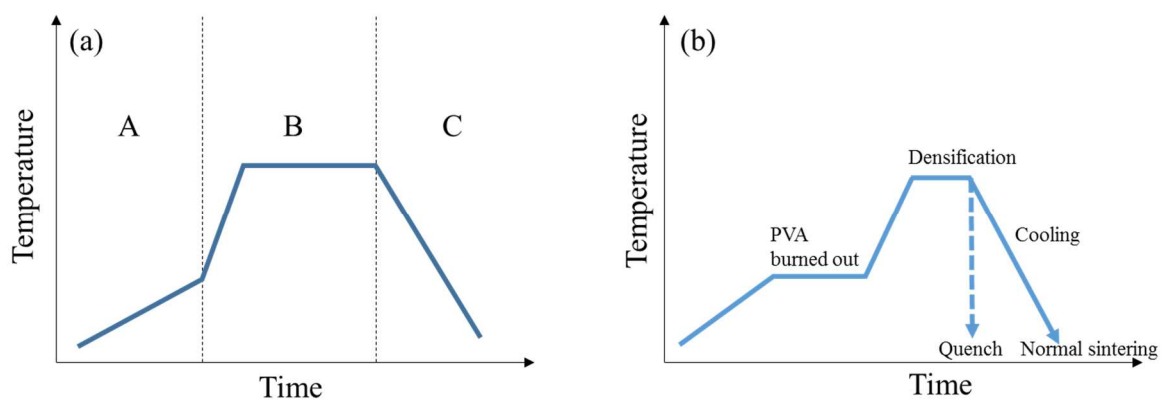


Fig. 4. 7 (a) Schematic of sintering temperature profile and (b) the profile schematic used in this project.

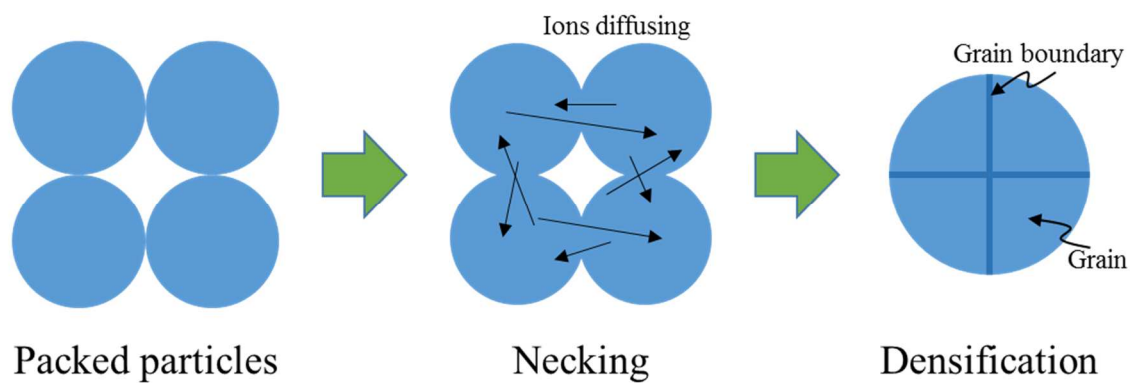


Fig. 4. 8 Schematic of sintering phenomenon.

Compacts were sintered 2h between 940 to 1040°C after burning out the binder at 550°C. The optimal sintering temperature was determined by  $d_{33}$ , not the density since the sintering temperature where the ceramics show the highest  $d_{33}$  is not always same as that of the highest

density. The optimal sintering temperatures of all the samples evaluated in this project are shown in table 4.6. In this project, a muffle furnace was used for sintering and the pellets were placed on Pt foil in a rectangular unlidded alumina crucible.

Table 4. 6 Optimal sintering temperature of the samples studied.

Composition	Optimal sintering temperature (°C)
Chapter 5	
$0.05\text{BiFe}(Me)\text{O}_3-0.25\text{BaTiO}_3-0.70\text{BiFeO}_3$	
$Me = \text{Y}$	960
$Me = \text{Sc}_{1/2}\text{Y}_{1/2}$	940
$Me = \text{Mg}_{2/3}\text{Nb}_{1/3}$	1000
$Me = \text{Sc}$	1010
$Me = \text{Zn}_{2/3}\text{Nb}_{1/3}$	1010
$Me = \text{Zn}_{1/2}\text{Ti}_{1/2}$	1010
$Me = \text{Ga}$	1010
$Me = \text{Al}$	970
Chapter 6	
$0.05\text{Bi}(\text{Mg}_{2/3}\text{Nb}_{1/3})\text{O}_3-(0.95-x)\text{BaTiO}_3-(x)\text{BiFeO}_3$	
$x = 0.55$	1020
$x = 0.60$	1010
$x = 0.63$	1000
$x = 0.65$	1010
$x = 0.70$	1000
$x = 0.75$	980
$x = 0.75$ (Quenched)	990
Chapter 7	
$0.05\text{BiScO}_3-(0.95-x)\text{BaTiO}_3-(x)\text{BiFeO}_3$	
$x = 0.55$	1020
$x = 0.60$	1005
$x = 0.625$	990
$x = 0.65$	1010
$x = 0.70$	1010
Chapter 8	
$0.05\text{Bi}(\text{Mg}_{2/3}\text{Nb}_{1/3})\text{O}_3-0.32\text{BaTiO}_3-0.63\text{BiFeO}_3$ (Multilayer Actuator)	
	1005

## Chapter 5: Optimising dopants in BiMeO<sub>3</sub>-BaTiO<sub>3</sub>-BiFeO<sub>3</sub> ceramics

### 5.1 Introduction

Ideally, for optimised properties in doped BT-BF ceramics, universal design rules are required based on established crystallochemical principles. The tolerance factor ( $t$ ) is known to indicate the local strain and stability of a perovskite phase. It has been used many times to predict/explain properties and expressed as equation 2.7. When the tolerance factor of a crystal is close to 1.0, the crystal structure is more stable and given a matrix composed of highly polarisable ionic species, ferroelectric properties are encouraged. Electronegativity difference,  $e_n$ , can also indicate the stability of the crystal structure as expressed in equation 2.8. When  $e_n$  is large, the bonding energy between the cation and oxygen ion increases and then the crystal structure becomes more stable.<sup>39, 40</sup> These two crystallochemical factors, listed in Table 1 for the studied composition, have been used in many ferroelectric systems but not brought to bear in BT-BF. To study the role of  $e_n$  and  $t$  in designing the optimum ferroelectric and piezoelectric response in BT-BF ceramics, compositions in the series 0.05Bi(*Me*)O<sub>3</sub>-(0.95- $x$ )BaTiO<sub>3</sub>-( $x$ )BiFeO<sub>3</sub> (*Me*: Y, Sc<sub>1/2</sub>Y<sub>1/2</sub>, Mg<sub>2/3</sub>Nb<sub>1/3</sub>, Sc, Zn<sub>2/3</sub>Nb<sub>1/3</sub>, Zn<sub>1/2</sub>Ti<sub>1/2</sub>, Ga, Al,  $x = 0.70$ ) were systematically investigated.

### 5.2 Results and Discussion

#### 5.2.1 XRD Analysis and microstructure

XRD diffractograms of 0.05Bi(*Me*)O<sub>3</sub>-0.25BaTiO<sub>3</sub>-0.70BiFeO<sub>3</sub> (*Me*: Y, Sc<sub>1/2</sub>Y<sub>1/2</sub>, Mg<sub>2/3</sub>Nb<sub>1/3</sub>, Sc, Zn<sub>2/3</sub>Nb<sub>1/3</sub>, Zn<sub>1/2</sub>Ti<sub>1/2</sub>, Ga, Al) ceramics are shown in Fig. 5.1. The main peaks in all patterns are indexed according to a perovskite structure. However, only compositions for which  $Me = Mg_{2/3}Nb_{1/3}$  and Sc are free from minor peaks associated with a secondary Bi<sub>22</sub>Fe<sub>2</sub>O<sub>36</sub> phase (PDCF card no. is 01-084-2559). We speculate that the absence of secondary phases relates to a combination of an ideal ionic radius for the B-site coupled with an electronegativity difference that suppresses the formation of complex phase assemblage on cooling.

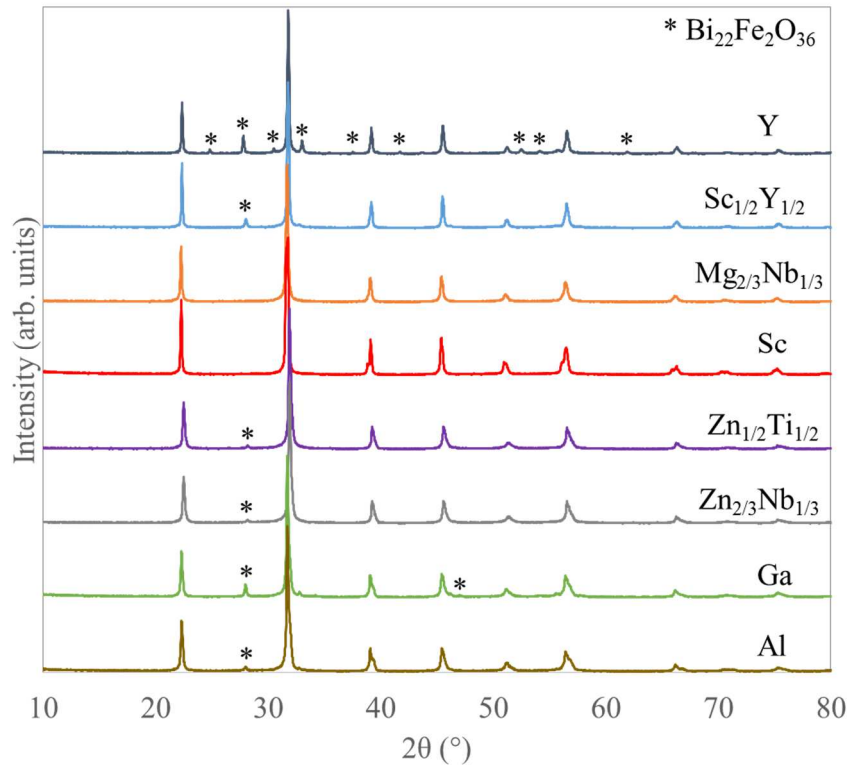


Fig. 5. 1 XRD diffractograms of  $0.05\text{Bi}(Me)\text{O}_3\text{-}0.25\text{BaTiO}_3\text{-}0.70\text{BiFeO}_3$  ( $Me = \text{Y}, \text{Sc}_{1/2}\text{Y}_{1/2}, \text{Mg}_{2/3}\text{Nb}_{1/3}, \text{Sc}, \text{Zn}_{2/3}\text{Nb}_{1/3}, \text{Zn}_{1/2}\text{Ti}_{1/2}, \text{Ga}, \text{Al}$ ) ceramics.

To investigate the microstructure and the compositional homogeneity of the ceramics, BSE images for the polished  $0.05\text{Bi}(Me)\text{O}_3\text{-}0.25\text{BaTiO}_3\text{-}0.70\text{BiFeO}_3$  ceramics were acquired (Fig. 5.2). For compositions with  $Me = \text{Mg}_{2/3}\text{Nb}_{1/3}$  and  $\text{Sc}$  the grain size was  $\sim 5$  to  $10 \mu\text{m}$  and the image contrast suggested a homogeneous cation distribution, free from second phase in agreement with the XRD traces. For composition with  $Me = \text{Y}$  and  $\text{Sc}_{1/2}\text{Y}_{1/2}$ , the grain size was smaller, with each grain exhibiting homogeneous contrast but with a light contrast, intergranular second phase, presumably  $\text{Bi}_{22}\text{Fe}_2\text{O}_{36}$  (Fig. 5.1) which has a larger weight average atomic number ( $WAA$ ) than the perovskite matrix. For ceramics with  $Me = \text{Zn}_{2/3}\text{Nb}_{1/3}, \text{Zn}_{1/2}\text{Ti}_{1/2}, \text{Ga}$ , and  $\text{Al}$ , a much smaller average grain size is observed ( $< 4 \mu\text{m}$ ) with evidence of a core shell contrast within the grains. Regions of the brightest contrast in the images are Bi-rich compared to the matrix according to energy dispersive X-ray analysis (Fig. 5.3 and Table 5.1) and assumed most parts are  $\text{Bi}_{22}\text{Fe}_2\text{O}_{36}$ , consistent with XRD data, Fig. 5. 1. Table 5.1 shows

that the brighter contrast area is a Bi-rich phase and darker contrast area is a Bi-poor phase. It is noted that there are the dark precipitates present in the  $\text{BiSc}_{1/2}\text{Y}_{1/2}\text{O}_3$  and  $\text{BiYO}_3$  doped samples (Fig. 5.2a and 5.2b) which correspond, according to EDS, to an yttrium ferrite phase (Fig. 5.4). We conclude therefore that  $\text{Y}_2\text{O}_3$  does not enter the matrix. In summary, we report that only  $\text{BiScO}_3$  and  $\text{BiMg}_{2/3}\text{Nb}_{1/3}\text{O}_3$  doped composition are free from secondary phase and exhibit a homogeneous microstructure. All other dopants either do not enter the lattice ( $\text{Y}_2\text{O}_3$ ) and/or modify the phase equilibria to promote  $\text{Bi}_{22}\text{Fe}_2\text{O}_{36}$  formation. In addition, compositions with  $Me = \text{Zn}_{2/3}\text{Nb}_{1/3}$ ,  $\text{Zn}_{1/2}\text{Ti}_{1/2}$ , Ga, and Al promote the formation of a two-phase perovskite matrix. Previous authors and the results of the next section have reported that immiscibility is suppressed by quenching.<sup>84, 116</sup>

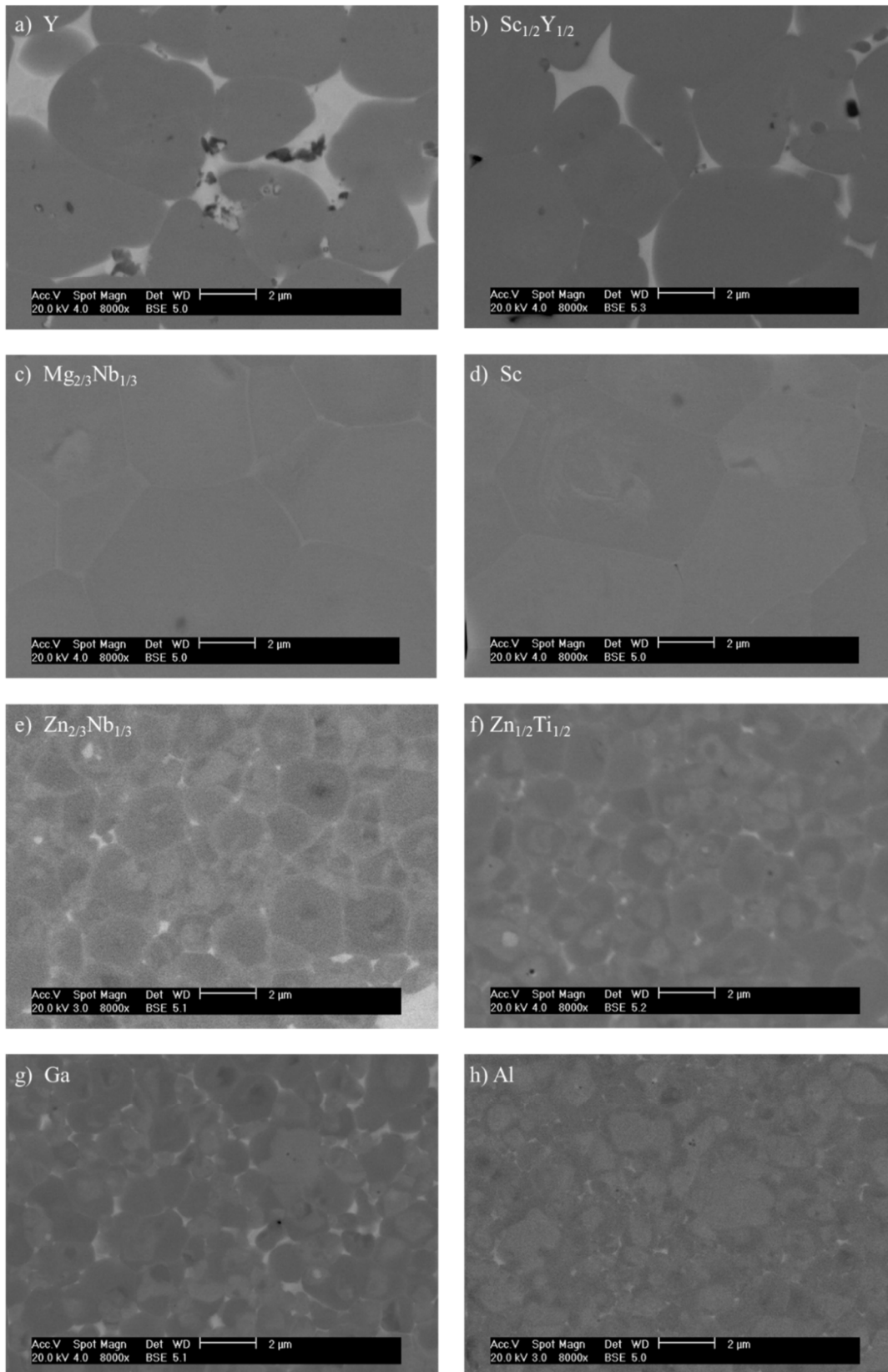


Fig. 5. 2 BSE images of polished surface of 0.05Bi(Me)O<sub>3</sub>-0.25BaTiO<sub>3</sub>-0.70BiFeO<sub>3</sub> ceramics, with Me = (a) Y, (b) Sc<sub>1/2</sub>Y<sub>1/2</sub>, (c) Mg<sub>2/3</sub>Nb<sub>1/3</sub>, (d) Sc, (e) Zn<sub>2/3</sub>Nb<sub>1/3</sub>, (f) Zn<sub>1/2</sub>Ti<sub>1/2</sub>, (g) Ga, and (h) Al.

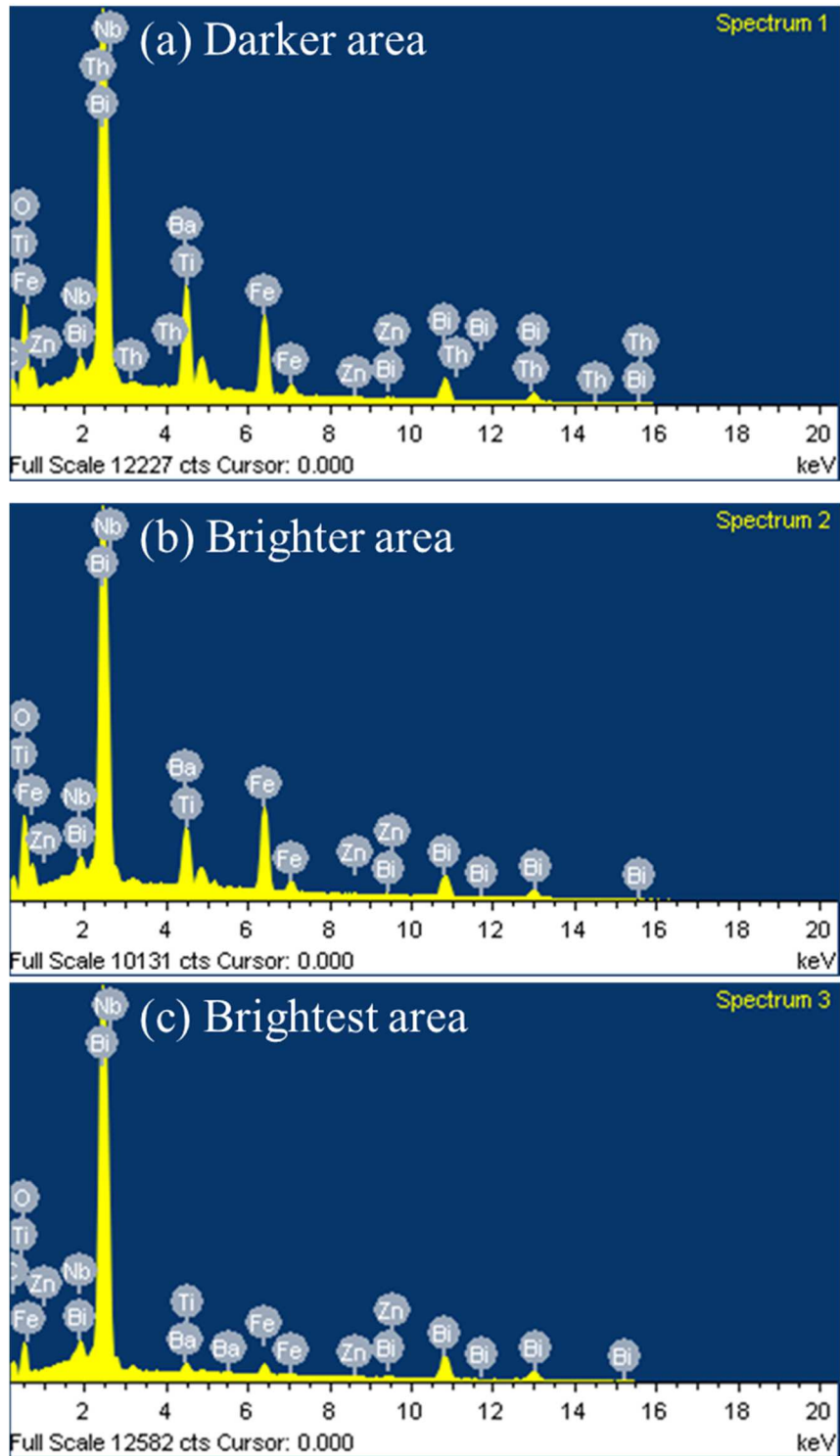


Fig. 5. 3 EDS point analysis spectrums of polished surface of  $0.05\text{BiZn}_{2/3}\text{Nb}_{1/3}\text{O}_3-0.25\text{BaTiO}_3-0.70\text{BiFeO}_3$  ceramics for (a) darker contrast area, (b) brighter contrast area, and (c) the brightest contrast area.

Table 5. 1 Quantitative analysis results for EDS point analysis spectrums of polished surface of  $0.05\text{BiZn}_{2/3}\text{Nb}_{1/3}\text{O}_3-0.25\text{BaTiO}_3-0.70\text{BiFeO}_3$  ceramics for (a) darker contrast area, (b) brighter contrast area, and (c) the brightest contrast area.

	mol%					
	Bi	Fe	Ba	Ti	Zn	Nb
Darker area	37.0	30.3	16.2	13.8	1.2	1.6
Brighter area	41.4	36.5	11.4	8.9	0.4	1.4
Brightest area	81.9	9.5	2.8	3.8	0.1	1.9

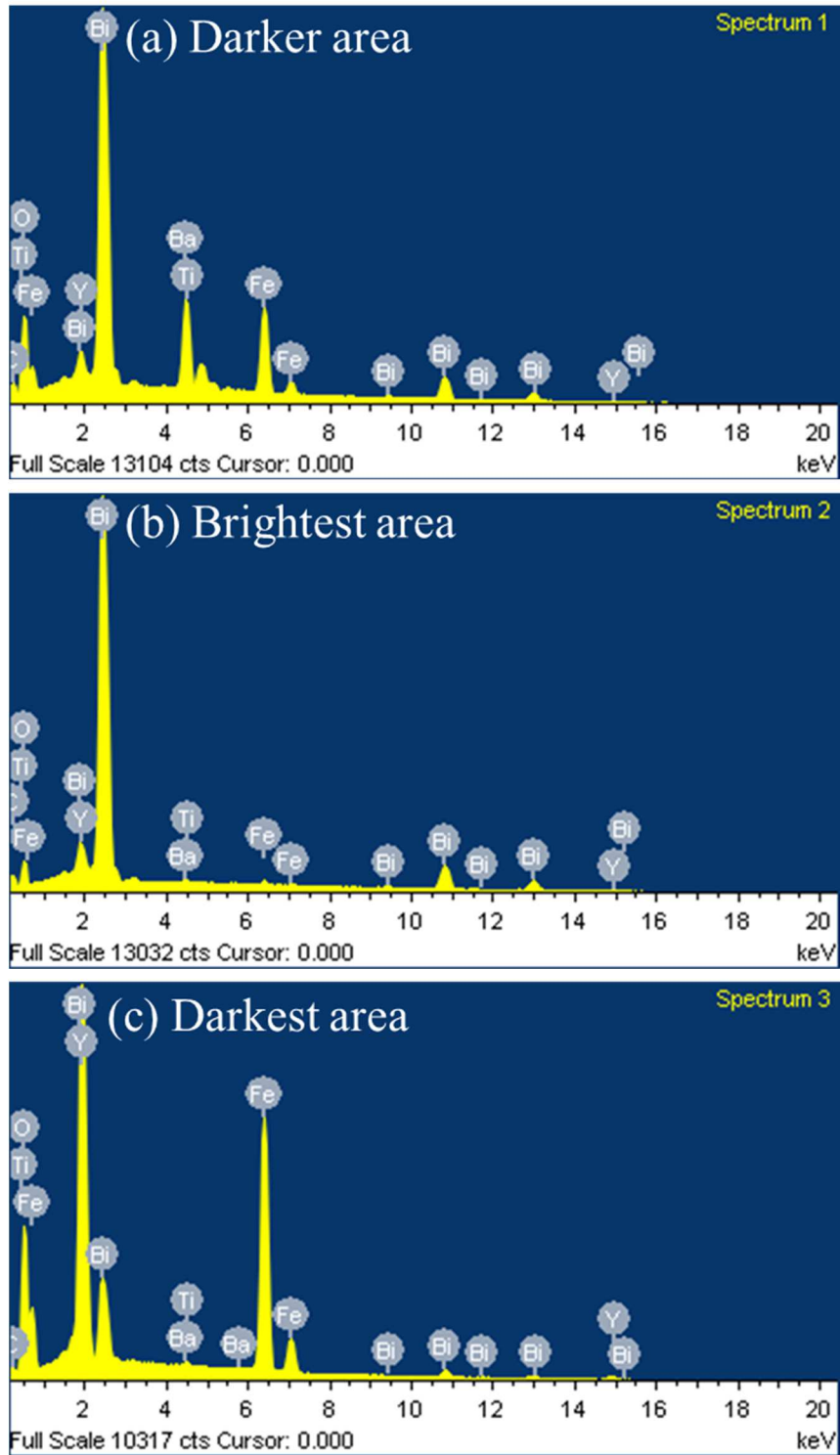


Fig. 5. 4 EDS point analysis spectrums of polished surface of  $0.05\text{BiYO}_3\text{-}0.25\text{BaTiO}_3\text{-}0.70\text{BiFeO}_3$  ceramics for (a) darker contrast area, (b) brighter contrast area, and (c) the brightest contrast area.

Table 5. 2 Quantitative analysis results for EDS point analysis spectrums of polished surface of 0.05BiYO<sub>3</sub>-0.25BaTiO<sub>3</sub>-0.70BiFeO<sub>3</sub> ceramics for (a) darker contrast area, (b) the brightest contrast area, and (c) the darkest contrast area.

	mol%				
	Bi	Fe	Ba	Ti	Y
Darker area	38.2	34.6	14.1	12.6	0.6
Brightest area	90.3	3.7	1.2	0.7	4.2
Darkest area	6.6	56.7	0.1	0.5	36.1

### 5.2.2 Temperature dependence of $\epsilon_r$ and $\tan\delta$

The temperature dependencies of  $\epsilon_r$  and  $\tan\delta$  for the 0.05Bi(*Me*)O<sub>3</sub>-0.25BaTiO<sub>3</sub>-0.70BiFeO<sub>3</sub> ceramics are shown in Fig. 5.5(a) and 5.5(b) (measured at 10 kHz). All anomalies are broad and often exhibit more than one dielectric maximum but the narrowest profiles occur for compositions with *Me* = Y, Sc<sub>1/2</sub>Y<sub>1/2</sub>, Mg<sub>2/3</sub>Nb<sub>1/3</sub>, and Sc (Fig. 5.5(a)) whose matrix perovskite grains exhibit a homogenous microstructure. In contrast, compositions with *Me* = Zn<sub>2/3</sub>Nb<sub>1/3</sub>, Zn<sub>1/2</sub>Ti<sub>1/2</sub>, Ga, and Al, show the broadest dielectric anomalies and exhibit a two phase perovskite core-shell matrix, attributed to immiscibility observed in the next section.<sup>116</sup> The dielectric loss for *Me* = Y and Sc<sub>1/2</sub>Y<sub>1/2</sub> (Fig. 5.5(b)), increases dramatically at ~100°C, consistent with the presence of a conducting grain boundary second phase (Fig. 5.2) 90% of which is composed of Bi<sub>2</sub>O<sub>3</sub>. However, further detailed investigation is necessary to reveal the conduction mechanism of the Bi rich phase. The other compositions show a steep increase at ~ 250 °C, typical of BaTiO<sub>3</sub>-BiFeO<sub>3</sub> based solid solutions<sup>116</sup> and likely to relate to migration of oxygen vacancies (*V<sub>O</sub>*) or space charges or point defects. Once again further investigation is required to make determine the conduction mechanism.

The relative permittivities of all the samples became negative at higher temperatures (>500 °C) but this is an artifact of the measurement caused by the sample's conductivity being greater than that of the measurement jigs, which is results in higher inductance in the samples.

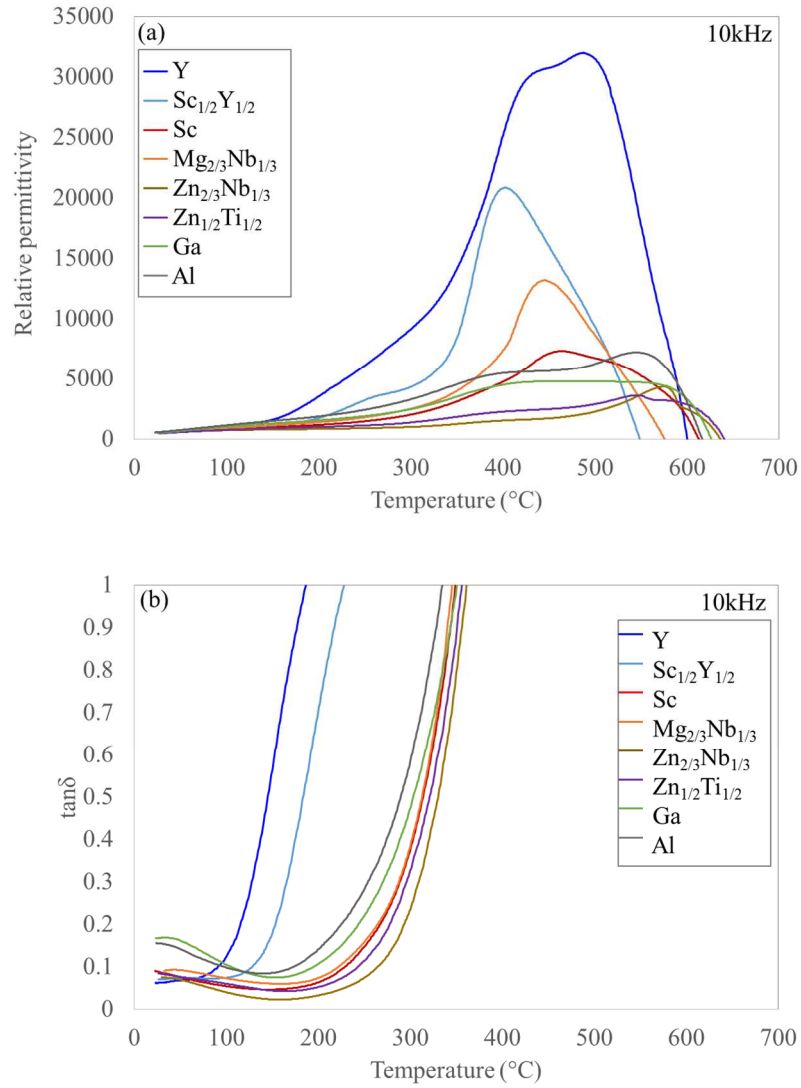


Fig. 5.5 Temperature dependence of (a) relative permittivity and (b) dielectric loss,  $\tan\delta$  for  $0.05\text{Bi}(Me)\text{O}_3\text{-}0.25\text{BaTiO}_3\text{-}0.70\text{BiFeO}_3$  ( $Me = \text{Y}, \text{Sc}_{1/2}\text{Y}_{1/2}, \text{Mg}_{2/3}\text{Nb}_{1/3}, \text{Sc}, \text{Zn}_{2/3}\text{Nb}_{1/3}, \text{Zn}_{1/2}\text{Ti}_{1/2}, \text{Ga}, \text{Al}$ ) ceramics.

### 5.2.3 Ferroelectric and Piezoelectric properties

PE hysteresis loops and bipolar SE curves for the  $0.05\text{Bi}(Me)\text{O}_3\text{-}0.25\text{BaTiO}_3\text{-}0.70\text{BiFeO}_3$  ceramics were measured under an electric field of 7 kV/mm at room temperature (Fig. 5.6(a) and Fig. 5.6(b)). For  $Me = \text{Mg}_{2/3}\text{Nb}_{1/3}$ , and Sc, the PE hysteresis loops show a classic ferroelectric square loop but for  $Me = \text{Y}$  and  $\text{Sc}_{1/2}\text{Y}_{1/2}$ , the loops are rounded consistent with a large contribution from a space charge distribution (presumably from the Bi-rich secondary phase) within the sample and concomitant with the higher dielectric loss. Slim and mainly

elliptical PE loops were recorded for  $Me = \text{Zn}_{1/2}\text{Ti}_{1/2}$ , Ga, and Al, suggesting only limited long-range ferroelectric order in these samples, consistent with the inhomogeneous matrix microstructure observed in Fig. 5.2.

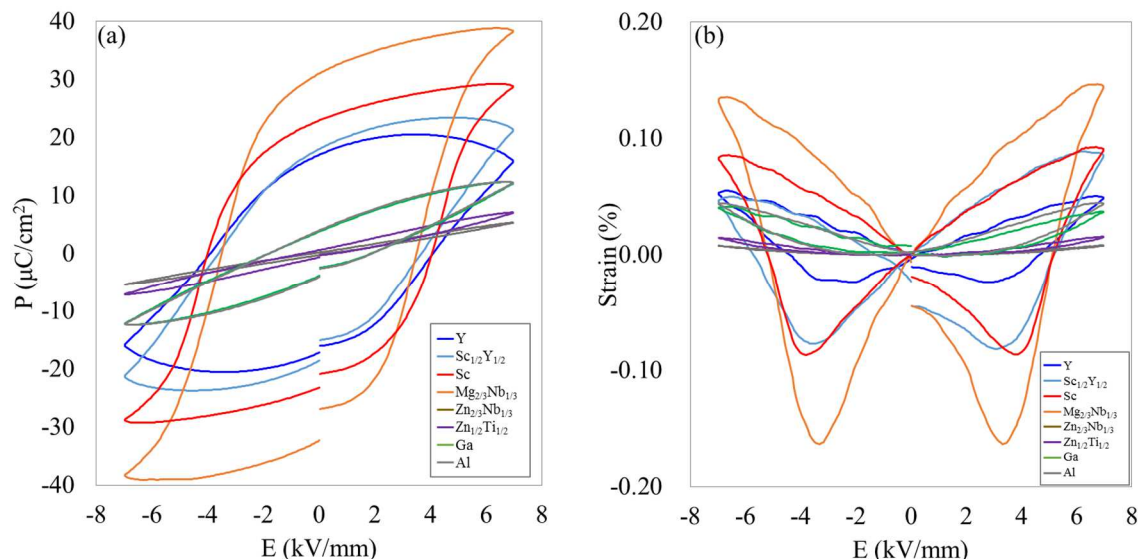


Fig. 5. 6 (a) PE hysteresis loops and (b) bipolar SE curves for  $0.05\text{Bi}(Me)\text{O}_3\text{-}0.25\text{BaTiO}_3\text{-}0.70\text{BiFeO}_3$  ( $Me = \text{Y}, \text{Sc}_{1/2}\text{Y}_{1/2}, \text{Mg}_{2/3}\text{Nb}_{1/3}, \text{Sc}, \text{Zn}_{2/3}\text{Nb}_{1/3}, \text{Zn}_{1/2}\text{Ti}_{1/2}, \text{Ga}, \text{Al}$ ) ceramics.

For bipolar strain, SE curves for  $Me = \text{Mg}_{2/3}\text{Nb}_{1/3}, \text{Sc}, \text{Y}$ , and  $\text{Sc}_{1/2}\text{Y}_{1/2}$  show butterfly loops typical of a long-range order ferroelectric but for  $Me = \text{Zn}_{1/2}\text{Ti}_{1/2}, \text{Ga}$ , and Al, the SE curves show a parabolic curve consistent with electrostrictive, relaxor-like materials. Compositions with  $Me = \text{Zn}_{2/3}\text{Nb}_{1/3}$ , exhibited near zero strain and consistent with the linear dielectric-like hysteresis loop, the significant heterogeneity in the matrix phase in Fig. 5.2 and the exceptionally broad dielectric anomaly in Fig. 5.5.

The Berlincourt piezoelectric coefficient ( $d_{33}$ ) for the  $0.05\text{Bi}(Me)\text{O}_3\text{-}0.25\text{BaTiO}_3\text{-}0.70\text{BiFeO}_3$  ceramics are plotted on a graph of  $t$  versus  $e_n$  (Fig. 5.7). The largest  $d_{33}$  values of 145 pC/N and 146 pC/N were achieved for  $Me = \text{Mg}_{2/3}\text{Nb}_{1/3}$  and Sc, consistent with the absence of secondary phase peaks in XRD traces and a homogeneous microstructure (Figs. 5.1 and 5.2), thereby encouraging long range polar order. Y and  $\text{Sc}_{1/2}\text{Y}_{1/2}$  exhibit smaller  $d_{33}$ , potentially due to the grain boundary secondary phase observed in BSE images (Figs. 5.1 and 5.2). Compositions with  $Me = \text{Zn}_{2/3}\text{Nb}_{1/3}, \text{Zn}_{1/2}\text{Ti}_{1/2}, \text{Ga}, \text{Al}$  exhibit a low  $d_{33}$  from 8 to 23 pC/N

which is attributed to the inhomogeneous cation distribution, as evidenced by the core-shell contrast in BSE images, (Fig. 5.2).

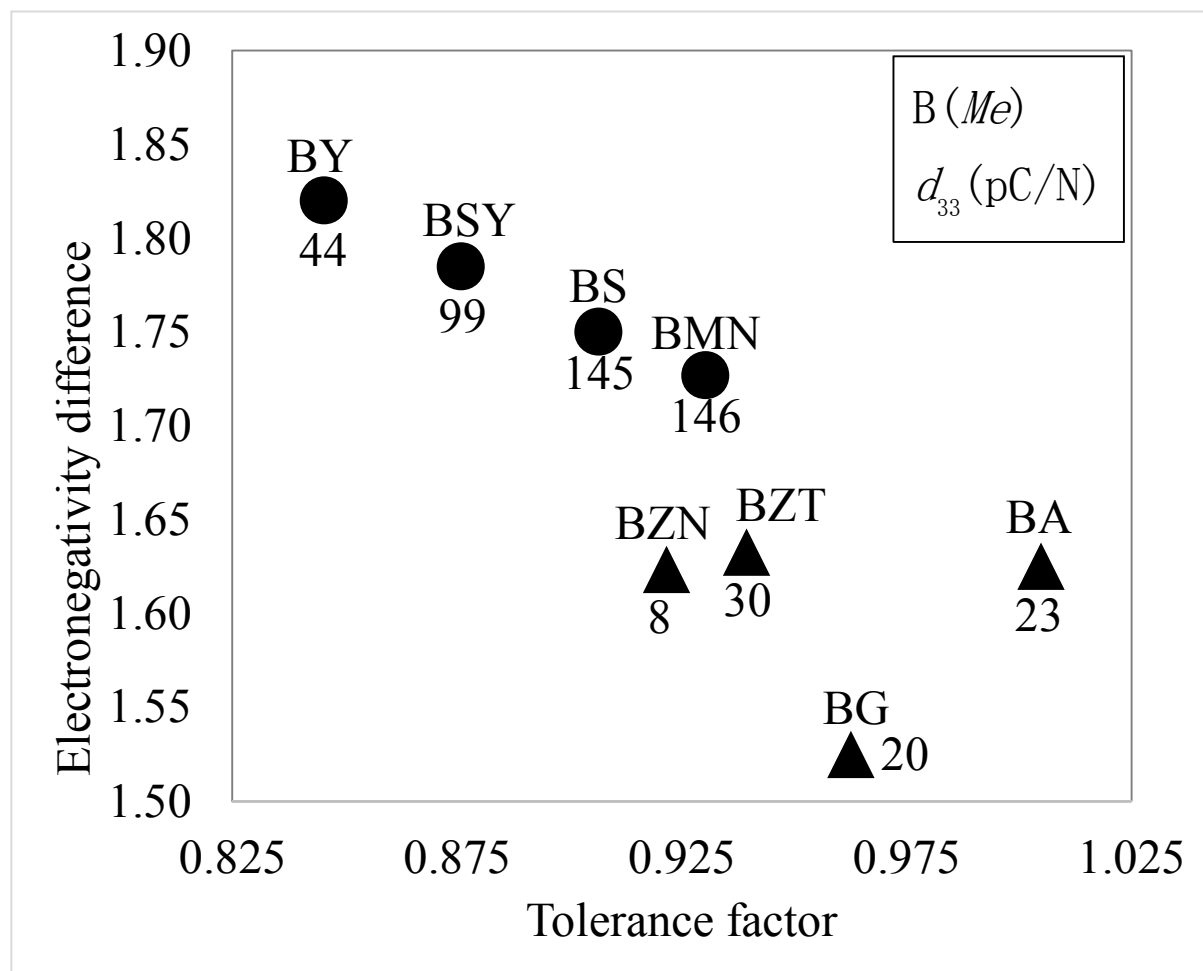


Fig. 5. 7 Piezoelectric coefficient  $d_{33}$ , tolerance factor, and electronegativity difference for  $0.05\text{Bi}(Me)\text{O}_3-0.25\text{BaTiO}_3-0.70\text{BiFeO}_3$  ( $Me = \text{Y}$  (BY),  $\text{Sc}_{1/2}\text{Y}_{1/2}$  (BSY),  $\text{Mg}_{2/3}\text{Nb}_{1/3}$  (BMN),  $\text{Sc}$  (BS),  $\text{Zn}_{2/3}\text{Nb}_{1/3}$  (BZN),  $\text{Zn}_{1/2}\text{Ti}_{1/2}$  (BZT),  $\text{Ga}$  (BG),  $\text{Al}$  (BA) ceramics. Numerical labels are the piezoelectric coefficient,  $d_{33}$ .

### 5.2.4 Crystallochemical Considerations

Fig. 5.7 is a plot of  $e_n$  vs.  $t$  for  $0.05\text{Bi}(Me)\text{O}_3-0.25\text{BaTiO}_3-0.70\text{BiFeO}_3$  compositions. With reference to Fig. 5.7 and related XRD, SEM and piezoelectric data, only  $\text{Mg}_{2/3}\text{Nb}_{1/3}$  and  $\text{Sc}$  doped compositions that lie within a narrow range of  $e_n$  vs.  $t$ , successfully substitute into the BT-BF matrix without either promoting secondary phases (yttrium ferrite and  $\text{Bi}_{22}\text{Fe}_2\text{O}_{36}$ ) or through altering the matrix cation distribution to contain two immiscible perovskite phases. It

is no coincidence that compositions with  $Me = \text{Mg}_{2/3}\text{Nb}_{1/3}$  and Sc reveal the optimum Berlincourt, low signal  $d_{33}$ . The effect of  $e_n$  and  $t$  on the phase assemblage has its origins in the local strain/bond strength induced by the substituents. Y ( $R_Y = 0.9 \text{ \AA}$ ) has a large ionic radius ( $R$ ) for a B-site species ( $R_{Ti} = 0.605$ ) and it therefore does not enter the perovskite lattice but instead reacts with  $\text{Fe}_2\text{O}_3$  to form an yttrium ferrite phase. This creates an excess of  $\text{Bi}_2\text{O}_3$  which is observed within the microstructure as  $\text{Bi}_{22}\text{Fe}_2\text{O}_{36}$  surrounding the perovskite grains, Fig. 5.2. Al, Ga and Zn ions have a low  $e_n$  and thus generally favour covalent bonding. covalent bonding is more directional and therefore makes it harder to control the reaction kinetics for forming homogeneous grain.<sup>139</sup> The result is an inhomogeneous distribution of cations and an immiscible two perovskite phase matrix. The underlying crystal chemistry for the perovskite-perovskite phase separation is undoubtedly complex but reinterpretation of previous reports in the literature suggests that immiscibility is commonly observed but suppressed by quenching to give higher  $d_{33}$ .<sup>84</sup> The results of the next section (Section 6) also reveals regions of perovskite – perovskite immiscibility in  $\text{Mg}_{2/3}\text{Nb}_{1/3}$  doped compositions as a function of  $\text{BaTiO}_3$  concentration.

### 5.3 Conclusion

The relationship between piezoelectric/ferroelectric properties and phase assemblage in  $0.05\text{Bi}(Me)\text{O}_3-(0.95-x)\text{BaTiO}_3-x\text{BiFeO}_3$  ( $Me = \text{Y}, \text{Sc}_{1/2}\text{Y}_{1/2}, \text{Mg}_{2/3}\text{Nb}_{1/3}, \text{Sc}, \text{Zn}_{2/3}\text{Nb}_{1/3}, \text{Zn}_{1/2}\text{Ti}_{1/2}, \text{Ga}, \text{Al}, x = 0.70$ ) was investigated as a function of  $e_n$  and  $t$ .  $\text{Mg}_{2/3}\text{Nb}_{1/3}$  and Sc have similar values of  $t$  and  $e_n$  and are the only substituents that do not create secondary phases or give rise to an inhomogeneous distribution of cations. B-site ion substituents with larger radii (Y) do not enter the lattice and result in the formation of secondary phases whereas lower  $e_n$  species give rise to a two-phase inhomogeneous perovskite core-shell matrix phase (immiscibility). Optimum ferroelectric and piezoelectric properties for  $x = 0.70$  were achieved for  $Me = \text{Sc}$  and  $\text{Mg}_{2/3}\text{Nb}_{1/3}$  which exhibit remarkably similar values of  $e_n$  and  $t$ .

## Chapter 6: 0.05Bi(Mg<sub>2/3</sub>Nb<sub>1/3</sub>)O<sub>3</sub>-(0.95-x)BaTiO<sub>3</sub>-(x)BiFeO<sub>3</sub> ceramics

### 6.1 Introduction

The results of chapter 6 revealed that (Mg<sub>2/3</sub>Nb<sub>1/3</sub>)O<sub>3</sub> and Sc have the potential to unlock the piezoelectric properties of BT-BF ceramics and prompted further studies on 0.05BiMg<sub>2/3</sub>Nb<sub>1/3</sub>O<sub>3</sub>-(0.95-x)BaTiO<sub>3</sub>-(x)BiFeO<sub>3</sub> (BMN-BT-BF,  $x = 0.55, 0.60, 0.63, 0.65, 0.70,$  and  $0.75$ ) and 0.05BiScO<sub>3</sub>-(0.95-x)BaTiO<sub>3</sub>-(x)BiFeO<sub>3</sub> (BS-BT-BF,  $x = 0.55, 0.60, 0.625, 0.65,$  and  $0.70$ ) ceramics. In this chapter, the relationship between piezoelectric and dielectric properties and structure/microstructure for BMN-BT-BF ceramics is reported.

As mentioned in the section of 2.2.4, given that all dopant strategies appear to empirically improve resistivity and stoichiometric/self-compensated dopants improve  $d_{33}$ , it is logical to design doped compositions which not only act locally as aliovalent dopants but which also maintain macroscopic stoichiometry. The base composition has a mixture of Fe<sup>3+</sup> and Ti<sup>4+</sup> on the B-site. Consequently, only 2+ ions (e.g. Mg<sup>2+</sup>) will consistently act as an acceptor irrespective of where they substitute in the lattice. A similar argument can be made for donor 5+ species (e.g. Nb<sup>5+</sup>) which will act as a local donor wherever they substitute on the B-site. Substituting in the ratio Mg<sub>2/3</sub>Nb<sub>1/3</sub> maintains macroscopic stoichiometry (assuming an average 3+ valence) by creating a self-compensated combined dopant and follows previous work on stoichiometric dopants, e.g. Bi(Mg<sub>1/2</sub>Ti<sub>1/2</sub>)O<sub>3</sub>-BaTiO<sub>3</sub>-BiFeO<sub>3</sub>, reported by other researchers.<sup>21,</sup><sup>26</sup> However, the higher valence of Nb<sup>5+</sup> in comparison to Ti<sup>4+</sup> ensures the universal presence of a donor as well as acceptor ion (Mg<sup>2+</sup>). In this chapter, there are two objectives. One is to confirm whether (Mg<sub>2/3</sub>Nb<sub>1/3</sub>) enters the BT-BF for all values of  $x$ , as suggested by the data in Section 5, the other is to determine its potential to optimize piezoelectric properties BT-BF ceramics.

### 6.2 Results and discussion

#### 6.2.1 XRD Analysis

XRD diffractograms of 0.05Bi(Mg<sub>2/3</sub>Nb<sub>1/3</sub>)O<sub>3</sub>-(0.95-x)BaTiO<sub>3</sub>-(x)BiFeO<sub>3</sub> ( $x = 0.55, 0.60, 0.63, 0.65, 0.70,$  and  $0.75$ ) ceramics are shown in Fig. 6.1. All patterns indexed according to a

perovskite structure with no secondary phase peaks present. In addition, to determine the most probable structure for each data set, Rietveld refinements were conducted (Table 6.1). As  $x$  increased from 0.55 to 0.75, a systematic change in structure occurred from pseudocubic ( $Pm-3m$ ) to mixed pseudocubic ( $Pm-3m$ ) and rhombohedral ( $R3c$ ) with the ratio of  $R3c/Pm-3m$  generally increasing with  $x$  as the  $\text{BiFeO}_3$  end member is approached. The Miller indices in the XRD traces of  $x = 0.55$  and  $x = 0.75$  in Fig. 6.1 are in the pseudocubic ( $Pm-3m$ ) and rhombohedral ( $R3c$ ) settings, respectively.

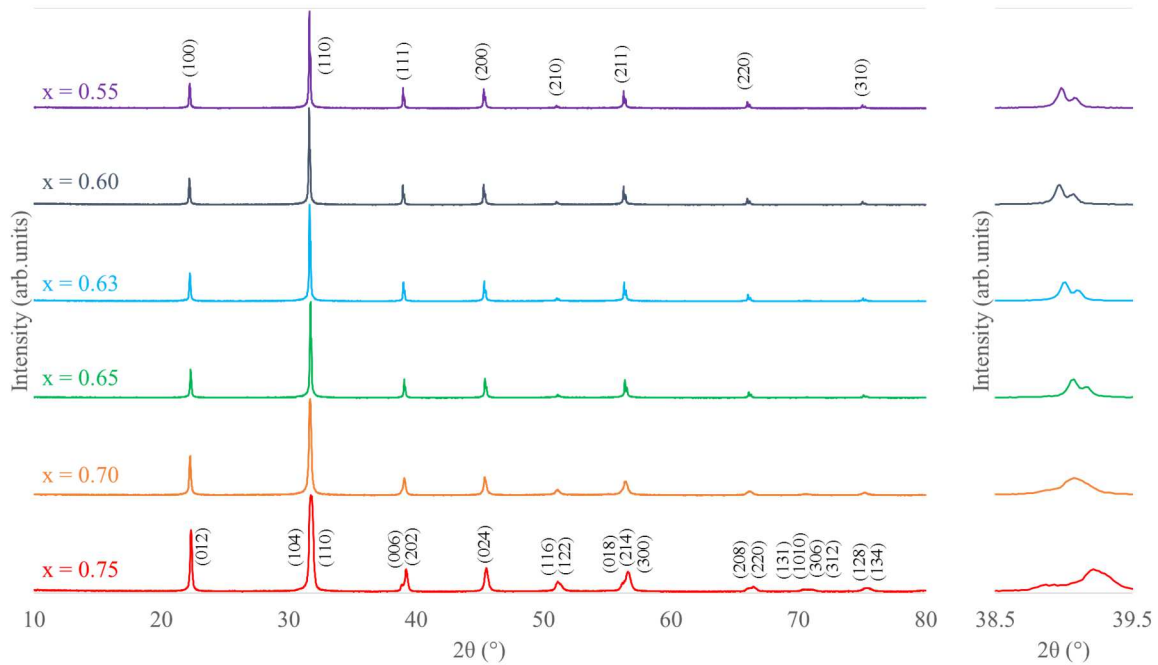


Fig. 6. 1 XRD patterns of  $0.05\text{Bi}(\text{Mg}_{2/3}\text{Nb}_{1/3})\text{O}_3-(0.95-x)\text{BaTiO}_3-(x)\text{BiFeO}_3$  ( $x = 0.55, 0.60, 0.63, 0.65, 0.70,$  and  $0.75$ ) ceramics measured at room temperature. Indexation for  $x = 0.55$  and  $0.75$  are in pseudocubic and rhombohedral settings, respectively.

Table 6. 1 Lattice parameters (a, b, and c), fraction of phase (wt%) and fitting parameters ( $R_{wp}$ ,  $R_p$ , and  $\chi^2$ ) for  $0.05\text{Bi}(\text{Mg}_{2/3}\text{Nb}_{1/3})\text{O}_3-(0.95-x)\text{BaTiO}_3-(x)\text{BiFeO}_3$  ( $x = 0.55, 0.60, 0.63, 0.65, 0.70, \text{ and } 0.75$ ) ceramics measured at room temperature.

$x$	Space group	Lattice parameters			Weight (%)	R-factors		
		$a$ (Å)	$b$ (Å)	$c$ (Å)		$R_{wp}$ (%)	$R_p$ (%)	$\chi^2$
0.55	<i>Pm-3m</i>	4.0007(9)	4.0007(9)	4.0007(9)		9.41	7.37	2.78
0.60	<i>Pm-3m</i>	3.9988(1)	3.9988(1)	3.9988(1)		9.51	7.46	3.07
0.63	<i>Pm-3m</i>	3.9980(8)	3.9980(8)	3.9980(8)	85.3	9.70	7.69	1.36
	<i>R3c</i>	5.6145(0)	5.6145(0)	14.0691(7)	14.7			
0.65	<i>Pm-3m</i>	3.9967(6)	3.9967(6)	3.9967(6)	86.5	10.3	8.29	1.67
	<i>R3c</i>	5.6573(8)	5.6573(8)	13.7388(5)	13.5			
0.70	<i>Pm-3m</i>	3.9994(6)	3.9994(6)	3.9994(6)	31.6	9.64	7.40	3.39
	<i>R3c</i>	5.6352(6)	5.6352(6)	13.8498(9)	68.4			
0.75	<i>Pm-3m</i>	3.9982(3)	3.9982(3)	3.9982(3)	13.3	9.40	7.33	3.04
	<i>R3c</i>	5.6272(6)	5.6272(6)	13.8844(2)	86.7			

## 6.2.2 Microstructure

To investigate the microstructure and the compositional homogeneity of ceramics, BSE images for the  $0.05\text{Bi}(\text{Mg}_{2/3}\text{Nb}_{1/3})\text{O}_3-(0.95-x)\text{BaTiO}_3-(x)\text{BiFeO}_3$  ceramics were acquired (Fig. 6.2). For all samples except  $x = 0.75$ , most grains were in the range of 5 to 10  $\mu\text{m}$  and image contrast suggested a homogeneous composition, indicating  $\text{Mg}^{2+}$  (0.72 Å) nm and  $\text{Nb}^{5+}$  (0.64 Å) reside on the B site (Fe, 0.645 Å and Ti, 0.601 Å). However, for  $x = 0.75$ , grains were  $< 5 \mu\text{m}$ , smaller than in other samples with evidence of a core-shell structure with darker and brighter contrast, relating to regions of lower ( $\text{BaTiO}_3$ -rich) and higher ( $\text{BiFeO}_3$ -rich) weight average atomic number consistent with energy dispersive X-ray analysis (Fig. 6.3). Inhomogeneity relates to the higher,  $\text{BiFeO}_3$  concentration in BT-BF ceramics with  $x = 0.7$ . Core shell microstructures are commonly observed in all BT-BF compositions as the  $\text{BiFeO}_3$  concentration increases and relate to competition between dominantly covalently ( $\text{BiFeO}_3$ ) and ionically ( $\text{BaTiO}_3$ ) bonded end members following similar arguments to that discussed in Chapter 5.

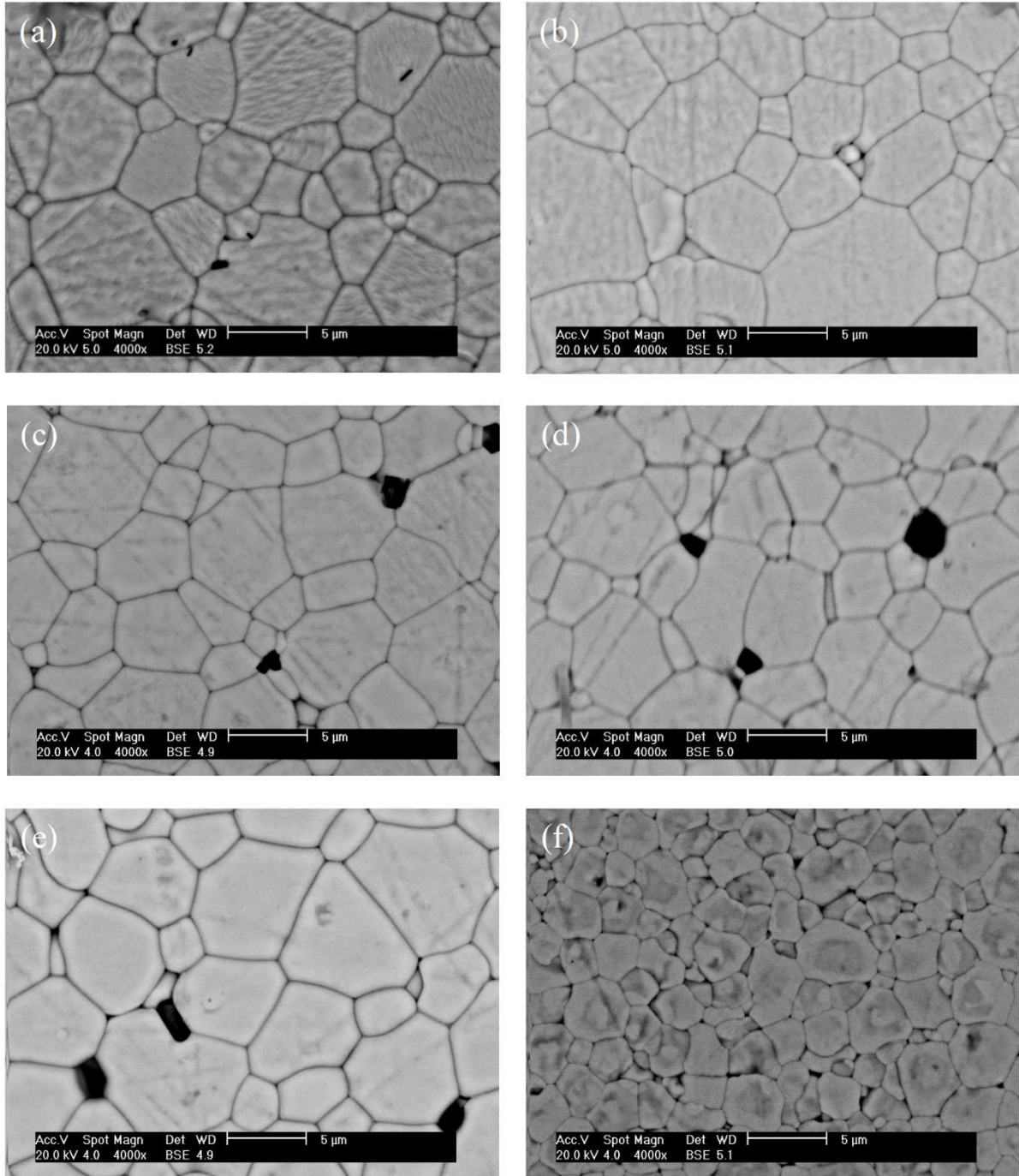
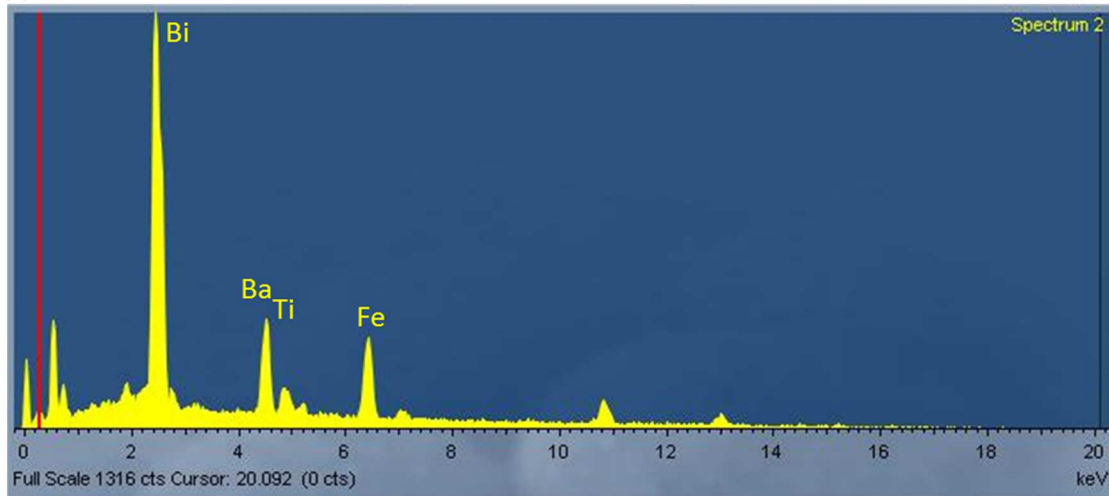


Fig. 6. 2 BSE images of polished surface of  $0.05\text{Bi}(\text{Mg}_{2/3}\text{Nb}_{1/3})\text{O}_3-(0.95-x)\text{BaTiO}_3-(x)\text{BiFeO}_3$  ceramics for  $x =$  (a) 0.55, (b) 0.60, (c) 0.63, (d) 0.65, (e) 0.70 and (f) 0.75. Residual flaws and irregularities are caused by polishing and thermal etching. Note that steps and flows are typically induced on the sample surface during polishing and enhanced by thermal etching.

(a) Darker area



(b) Brighter area

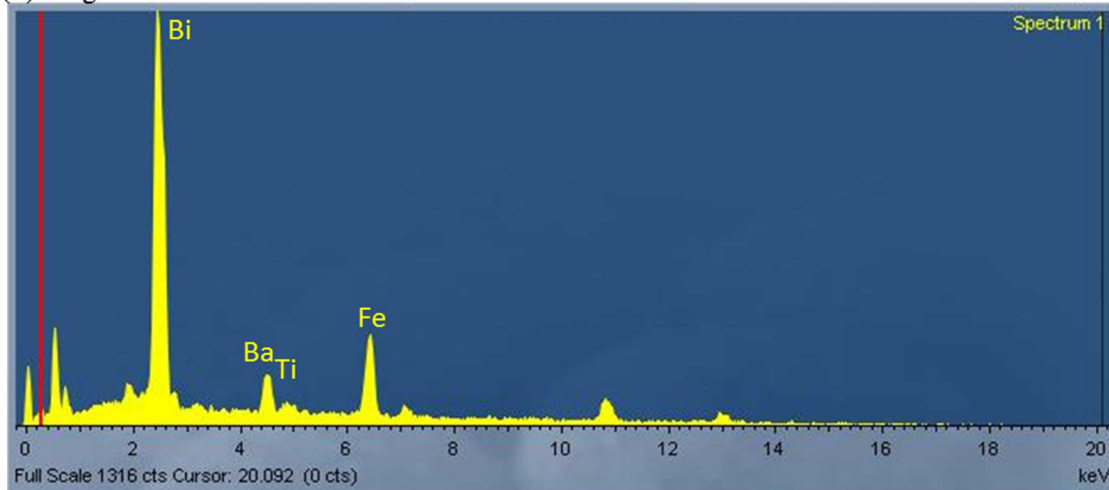


Fig. 6. 3 EDS point analysis spectra of (a) darker contrast area (b) brighter contrast area for  $0.05\text{Bi}(\text{Mg}_{2/3}\text{Nb}_{1/3})\text{O}_3\text{-}0.20\text{BaTiO}_3\text{-}0.75\text{BiFeO}_3$ . The spectrum of the darker contrast area illustrates larger peak of Ba and Ti, indicating the area is  $\text{BaTiO}_3$  rich phase.

Fig. 6.4 (a) is a dark field two beam TEM image of a sample with  $x = 0.63$  obtained using a 111 reflection with the electron beam approximately parallel to a [110] direction. There is no evidence of long range polar order (no distinct domain walls) and only local correlation of fringe contrast, typical of a pseudocubic (XRD data in Fig. 6.1), relaxor-like compound with a nano- rather than macro- domain structure. Inset in Fig. 6.4 (a) is a [110] zone axis diffraction pattern. Only fundamental perovskite spots appear in the pattern with no superstructure reflections, indicating the absence of octahedral tilting. In contrast, Fig 6.4 (b) shows a bright

field image near a  $[112]$  direction for samples with  $x = 0.7$  which shows an  $R3c$  phase, consistent with the XRD data, Fig. 6.1. The  $R3c$  phase is characterised by lamellar ferroelectric domains with corresponding diffraction patterns exhibiting  $\frac{1}{2}\{000\}$  antiphase tilting superstructure reflections in some but not all  $\langle 112 \rangle$  zone axes. Two variants of the  $\langle 112 \rangle$  zone axes (with and without  $\frac{1}{2}\{000\}$ ) are included in Fig 6.4(b). Please note that on tilting the sample lamellar domains may also be observed in the upper RHS of the image. XRD and BSE images, indicate that for  $0.63 \leq x \leq 0.75$ , rhombohedral phase and pseudocubic phase coexist even within homogeneous grains, implying the coexistence of nano and lamellar ferroelectric domains.

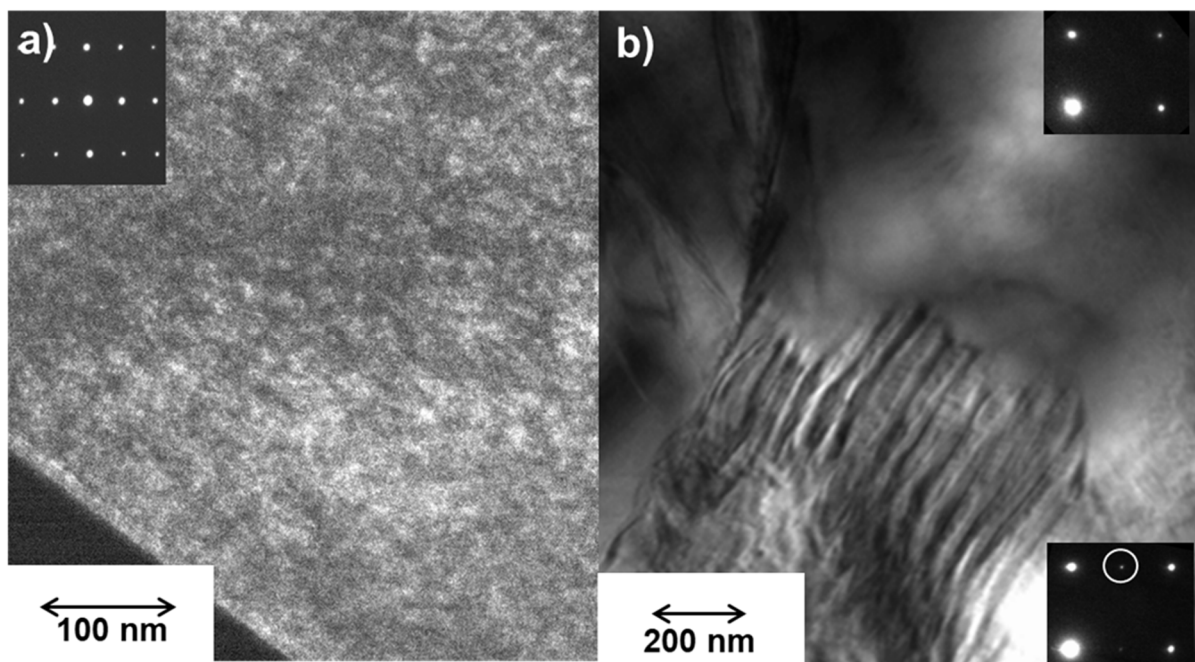


Fig. 6. 4 a) Two beam dark field transmission electron microscopy image of a sample with  $x = 0.63$  obtained using a  $111$  reflection close to the  $[110]$  direction, illustrating the nanodomain structure of the pseudocubic relaxor-like phase. Inset is the  $[110]$  zone axis diffraction pattern in which only fundamental perovskite reflections are apparent. b) Bright field image of  $x = 0.7$  close to the  $[112]$  direction. Bottom LHS shows lamellar ferroelectric domains and the top RHS exhibits a similar domain structure on tilting. Inset are two variants of the  $[112]$  zone axis for the  $R3c$  phase with and without  $\frac{1}{2}\{000\}$  antiphase tilt reflections.

To evaluate the electrical homogeneity, impedance spectroscopy (IS) analysis was conducted. Spectroscopic plots of  $Z''$  and  $M''$  extracted from impedance spectroscopy data may be used as a simple means to qualitatively assess electrical homogeneity. Fig. 6.5 (a-f) show  $Z''$  and  $M''$  from complex IS plots with frequency for the  $0.05\text{Bi}(\text{Mg}_{2/3}\text{Nb}_{1/3})\text{O}_3-(0.95-x)\text{BaTiO}_3-(x)\text{BiFeO}_3$  ceramics. For  $x = 0.55$  to  $0.70$ , the measurements were conducted at  $320^\circ\text{C}$ . For  $x =$

0.75, the measurement was conducted at 180°C to ascertain the entire shape of the  $Z''$  and  $M''$  spectra. All  $M''$  spectra show a main peak and the low frequency tail of a second, higher frequency peak, indicating that they all have two or more electrical phases, most likely relating to either grain boundary, shell or core regions. The capacitance calculated from  $Z''_{max}$  measured at 320°C for the  $0.05\text{Bi}(\text{Mg}_{2/3}\text{Nb}_{1/3})\text{O}_3-(0.95-x)\text{BaTiO}_3-(x)\text{BiFeO}_3$  ceramics are shown in Table 6.2. For  $x = 0.55$  to  $0.65$ , the capacitance values are  $\sim 1$  to  $2$  nF which is consistent with a grain boundary type-response but the capacitance decreases to  $0.43$  nF for  $x = 0.70$  and  $0.13$  nF for  $x = 0.75$  and these lower values are more indicative of a shell-type response. For  $x = 0.75$  there is a clear gap between the peak positions of  $Z''$  and  $M''$ , indicating the main electric path is electrically heterogeneous which may correspond to compositional inhomogeneity shown in the BSE image.

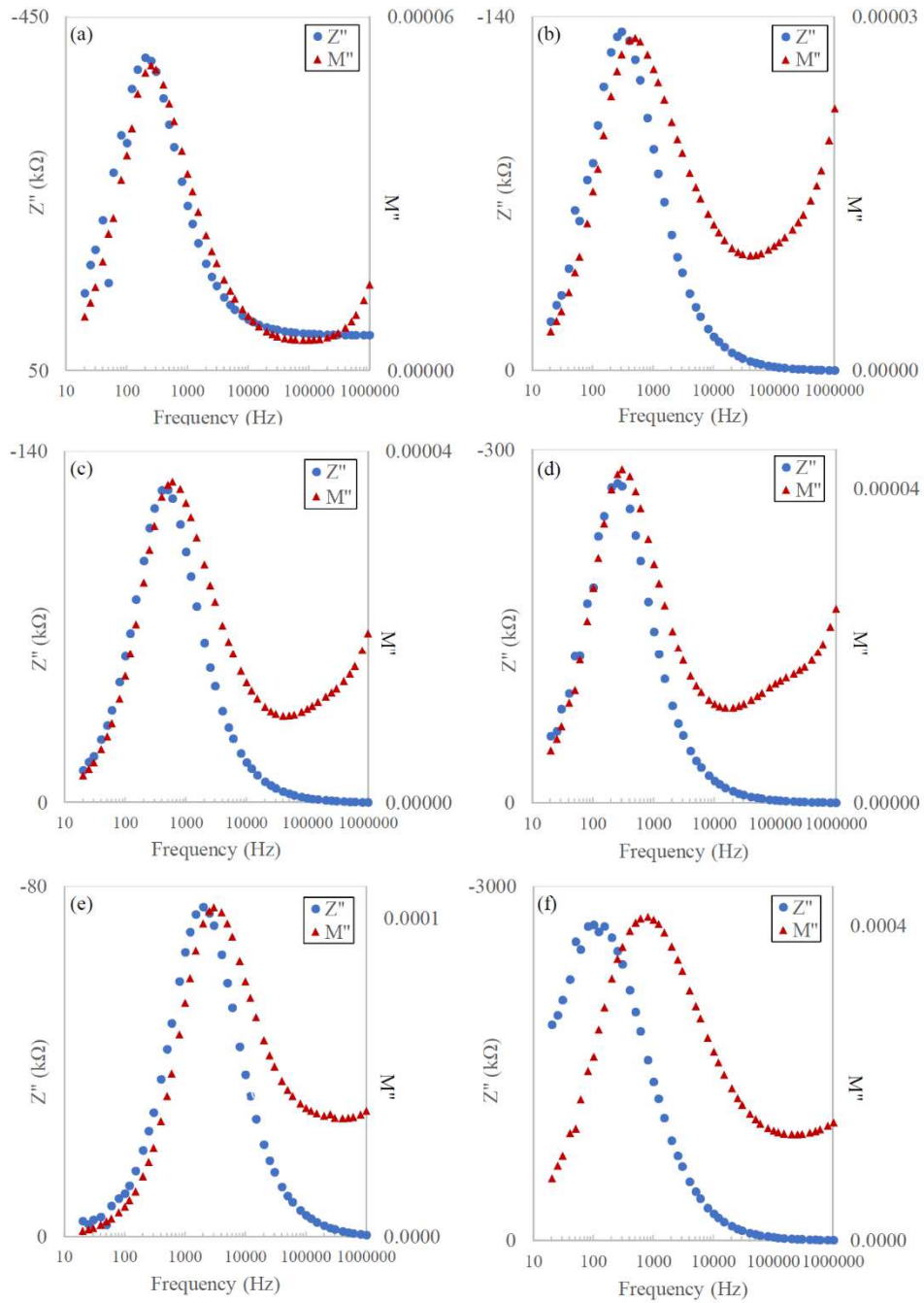


Fig. 6. 5 Combined  $Z''$  and  $M''$  spectroscopic plots for  $0.05\text{Bi}(\text{Mg}_{2/3}\text{Nb}_{1/3})\text{O}_3-(0.95-x)\text{BaTiO}_3-(x)\text{BiFeO}_3$  ceramic with  $x =$  (a) 0.55, (b) 0.60, (c) 0.63, (d) 0.65, (e) 0.70 measured at 320°C and (f) 0.75 and measured at 180°C.

Table 6. 2 Capacitance measured at 320°C (from  $Z''$  peak) and activation energy for the dc conductivity for  $0.05\text{Bi}(\text{Mg}_{2/3}\text{Nb}_{1/3})\text{O}_3-(0.95-x)\text{BaTiO}_3-(x)\text{BiFeO}_3$  ( $x = 0.55, 0.60, 0.63, 0.65, 0.70, \text{ and } 0.75$ ) ceramics.

$x$	Capacitance at 320°C $C$ (nF/cm)	Activation Energy $E_a$ (eV)
0.55	1.01	1.12
0.60	1.98	1.11
0.63	1.59	1.15
0.65	1.17	1.14
0.70	0.43	1.11
0.75	0.13	0.87

The total electrical conductivity ( $\sigma_{dc} = 1/R$ ) was calculated from the low frequency intercept of the large arc in the  $Z^*$  plots in Fig. 6.6 which is an example for  $x=0.63$  which corresponds to the large  $Z''$  peak observed in Fig. 6.5 (a-f),  $\sigma_{dc}$  versus reciprocal temperature for the  $0.05\text{Bi}(\text{Mg}_{2/3}\text{Nb}_{1/3})\text{O}_3-(0.95-x)\text{BaTiO}_3-(x)\text{BiFeO}_3$  ceramics are shown in Fig. 6.7 and the activation energy ( $E_a$ ) calculated from these plots are shown in Table 2. Fig. 6.7 shows that  $x = 0.75$  is more conductive than the others. For  $x = 0.75$ , the  $E_a$  is clearly smaller, which means there is an obvious difference in the conduction mechanism between  $x = 0.55$  to  $0.65$  and  $x = 0.75$  and supports the conductivity results. Furthermore, these data imply that the electric path which show high resistivity for  $x = 0.55$  to  $0.65$  is not present in  $x = 0.75$ . In other words, when compositions are microstructurally homogeneous (e.g.  $x = 0.55$  to  $0.65$ ) a high resistive electric path is maintained. Looking at  $x = 0.60, 0.63, \text{ and } 0.65$ , the highest conductivity was obtained for  $x = 0.63$  and the lowest for  $x = 0.65$ , inconsistent with BF ratio and implying complex behavior in composition where pseudocubic and rhombohedral phases coexist. The high resistive electrical path is tentatively attributed to a grain boundary response but further measurements are required to confirm this assignment.

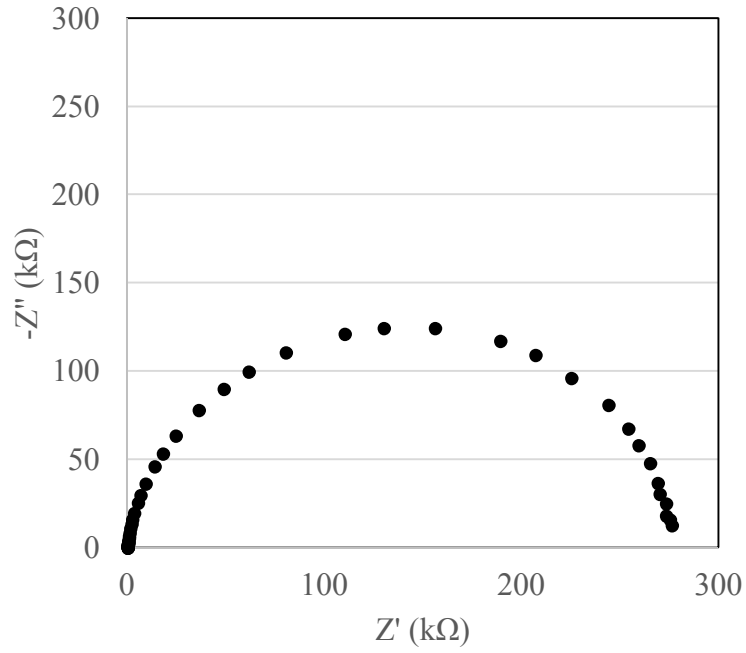


Fig. 6. 6  $Z^*$  plots for  $0.05\text{Bi}(\text{Mg}_{2/3}\text{Nb}_{1/3})\text{O}_3\text{-}0.32\text{BaTiO}_3\text{-}0.63\text{BiFeO}_3$  ceramics.

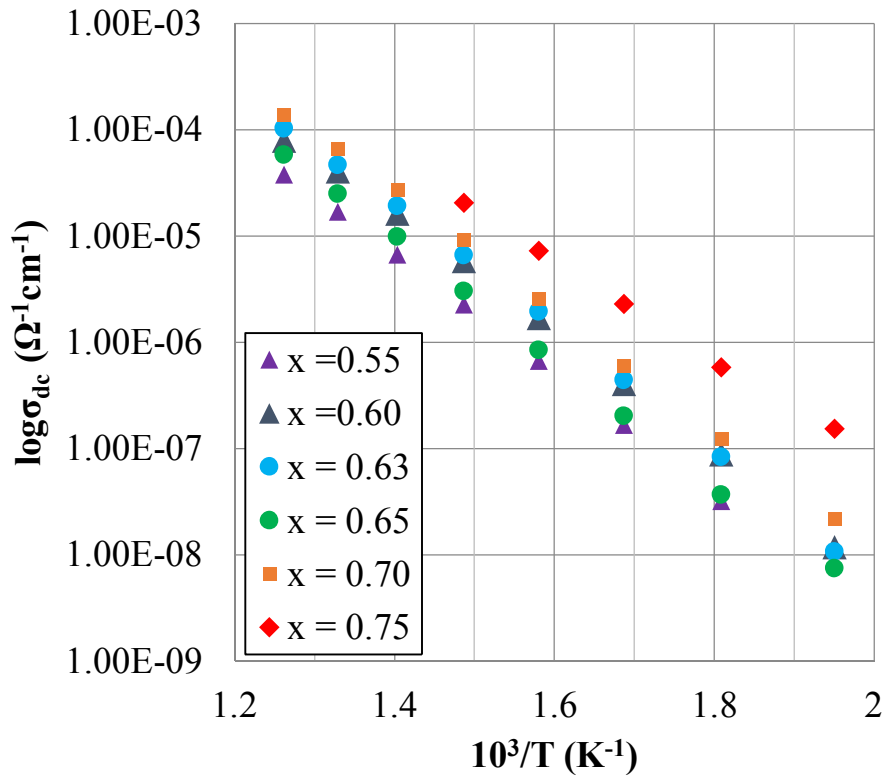


Fig. 6. 7 Arrhenius plot of the dc electrical conductivity for  $0.05\text{Bi}(\text{Mg}_{2/3}\text{Nb}_{1/3})\text{O}_3\text{-}(0.95\text{-}x)\text{BaTiO}_3\text{-}(x)\text{BiFeO}_3$  ( $x = 0.55, 0.60, 0.63, 0.65, 0.70,$  and  $0.75$ ) ceramics.

### 6.2.3 Temperature dependence of relative permittivity ( $\epsilon_r$ ) and $\tan\delta$

The temperature dependencies of  $\epsilon_r$  and  $\tan\delta$  for the  $0.05\text{Bi}(\text{Mg}_{2/3}\text{Nb}_{1/3})\text{O}_3-(0.95-x)\text{BaTiO}_3-x\text{BiFeO}_3$  ceramics are shown in Fig. 6.8(a) and 6.8(b) (measured at 10 kHz). For  $x = 0.55$  (Fig. 6.7(a)), the dielectric anomaly is broadly consistent with a relaxor-like transition and concomitant with the pseudocubic structure refined from XRD data. As  $x$  increases to  $x = 0.70$ , the dielectric anomalies sharpen as the volume fraction of the ferroelectric ( $R3c$ ) phase in structural refinements increases. However, for  $x = 0.75$ , a broad flat dielectric anomaly is observed suggesting that this composition is no longer homogeneous, as confirmed by BSE images and  $Z''$ ,  $M''$  impedance plots.

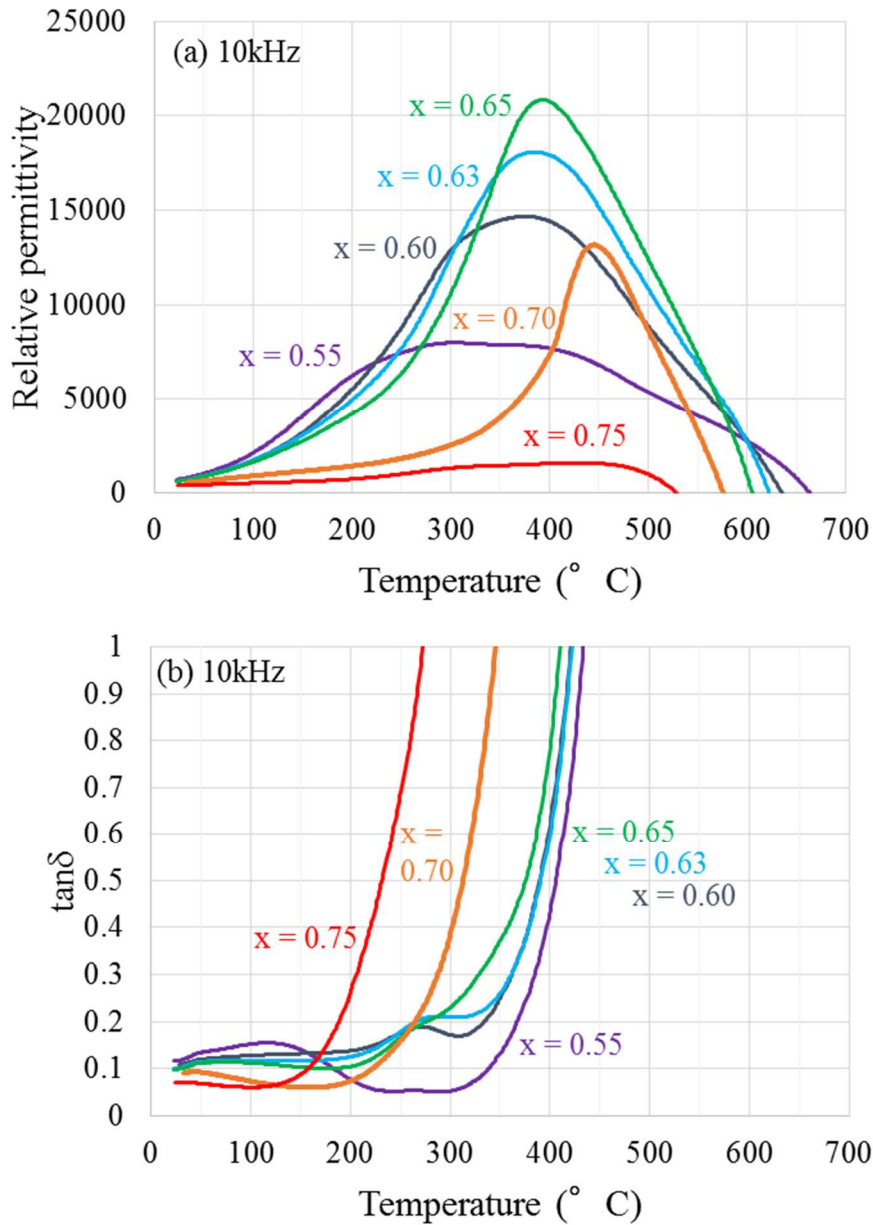


Fig. 6. 8 Temperature dependence of (a) relative permittivity and (b) dielectric loss,  $\tan\delta$  for  $0.05\text{Bi}(\text{Mg}_{2/3}\text{Nb}_{1/3})\text{O}_3-(0.95-x)\text{BaTiO}_3-(x)\text{BiFeO}_3$  ( $x = 0.55, 0.60, 0.63, 0.65, 0.70,$  and  $0.75$ ) ceramics.

The frequency dependence of  $\epsilon_r$  and  $\tan\delta$  vs. temperature for  $0.05\text{Bi}(\text{Mg}_{2/3}\text{Nb}_{1/3})\text{O}_3-(1-x)\text{BaTiO}_3-(x)\text{BiFeO}_3$  ceramics ( $x =$  (a) 0.55, (b) 0.63, (c) 0.70) measured at 1, 10, 100, and 250 kHz are shown in Fig. 6.9. For  $x = 0.55$ , the dielectric anomaly and  $\tan\delta$  shift to high temperature as the frequency increases, indicating these ceramics are relaxors. For  $x = 0.70$ , the dielectric anomaly also shifts in a similar manner to  $x = 0.55$  but by a smaller interval,

probably due to the difference of the ratio of relaxor-like to ferroelectric-like phase. However, for  $x = 0.63$ , the dielectric anomaly decreased but did not shift from 10 kHz to 100 kHz. The reason for the absence of classic relaxor-like behaviour is not clear but may relate to the presence of multiple phase transitions which obscure the trends expected for pseudocubic ceramics which contain short range ordered polar nanoregions, as evidenced by XRD (Fig. 6.1) and TEM (Fig. 6.4).

$\tan\delta$  for all compositions at room temperature in Fig. 6.8 is typically  $<0.1$  and for  $0.55 \leq x \leq 0.65$  does not increase significantly until  $>350^\circ\text{C}$  which is encouraging for high temperature applications. However, for  $x \geq 0.70$  the onset of the sharp increase in dielectric loss shifts to lower temperatures, consistent with a chemically and electrically inhomogeneous microstructure observed by BSE images and  $Z''$ ,  $M''$ , impedance plots, respectively. The onset point at which  $\tan\delta$  rises, decreases as  $x$  increases (Fig. 6.7), indicating that the conduction mechanism but not the conductivity relates to the BT/BF ratio but further investigation is required.

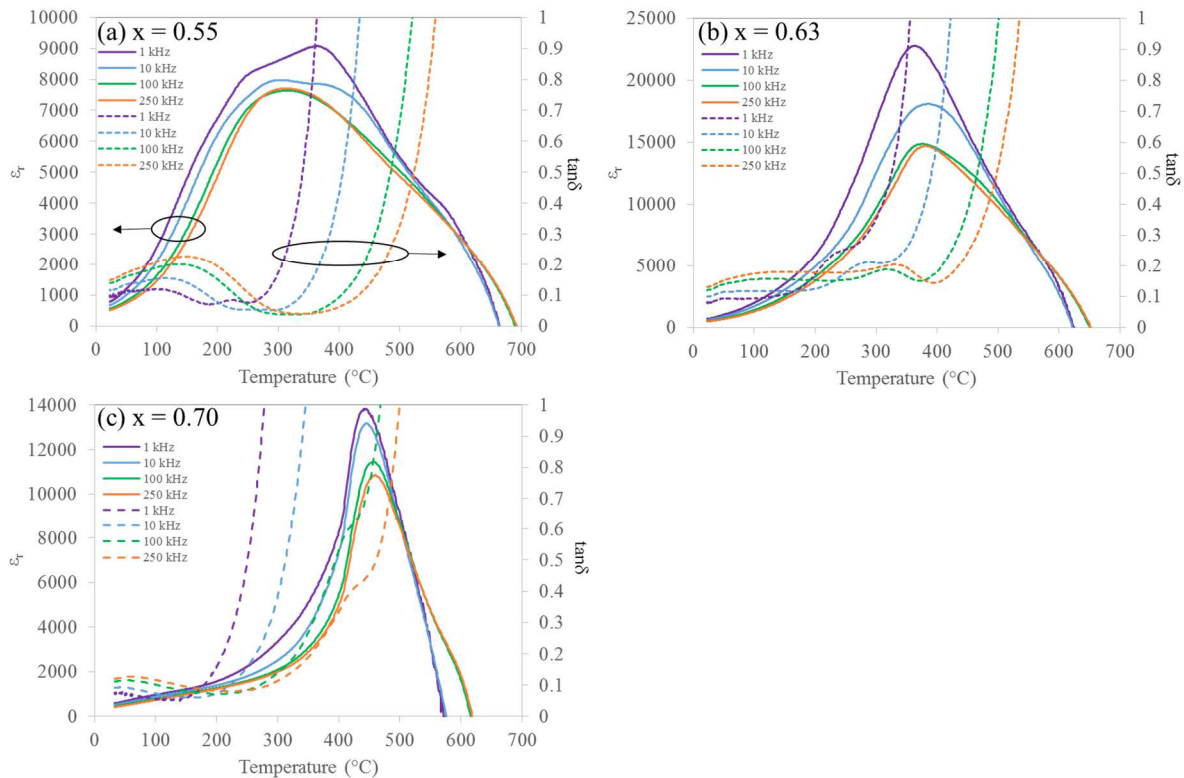


Fig. 6. 9 Frequency dependence of relative permittivity and  $\tan\delta$  vs temperature for  $0.05\text{Bi}(\text{Mg}_{2/3}\text{Nb}_{1/3})\text{O}_3-(0.95-x)\text{BaTiO}_3-(x)\text{BiFeO}_3$  ( $x =$  (a) 0.55, (b) 0.63, and (c) 0.70).

## 6.2.4 Ferroelectric and Piezoelectric properties

PE hysteresis loops and bipolar SE curves for the  $0.05(\text{Mg}_{2/3}\text{Nb}_{1/3})\text{O}_3-(0.95-x)\text{BaTiO}_3-(x)\text{BiFeO}_3$  ceramics were measured under an electric field of 7 kV/mm at room temperature (Fig. 6.10(a) and Fig. 6.10(b)). PE hysteresis loops show a change from a narrow hysteresis loop, more typical of electrostrictive compositions with limited or no long-range ferroelectricity to a classic ferroelectric square loop as  $x$  increases until 0.7, consistent with the increase in volume fraction of the  $R3c$  phase. A similar trend is observed for bipolar strain field measurements which transform from loops commensurate with dominant electrostrictive behaviour (negligible negative strain) to classic butterfly loops typical of a long-range order ferroelectric. However,  $x = 0.75$  does not exhibit ferroelectric hysteresis and shows negligible strain, concomitant with an electrically and chemically inhomogeneous ceramic. Unpoled samples with  $x = 0.63$  recorded the maximum strain of 0.41% at 10kV/mm at room temperature (Fig. 6.11 (a)). It is noted however, that the largest  $d_{33}^*$  was obtained for this composition in the poled state, notably at 5kV/mm rather than 10 kV/mm (544 pm/V), Fig. 6.11 (b). We further note that the largest strains/ $d_{33}^*$  are recorded at the point of crossover from dominant relaxor, electrostrictive ( $x < 0.63$ ) to ferroelectric behaviour ( $0.65 \leq x \leq 0.70$ ), a trend previously observed in Pb-free systems based on NBT or  $(\text{K}_{0.5}\text{Bi}_{0.5})\text{TiO}_3$  (KBT).<sup>71, 117, 118</sup>

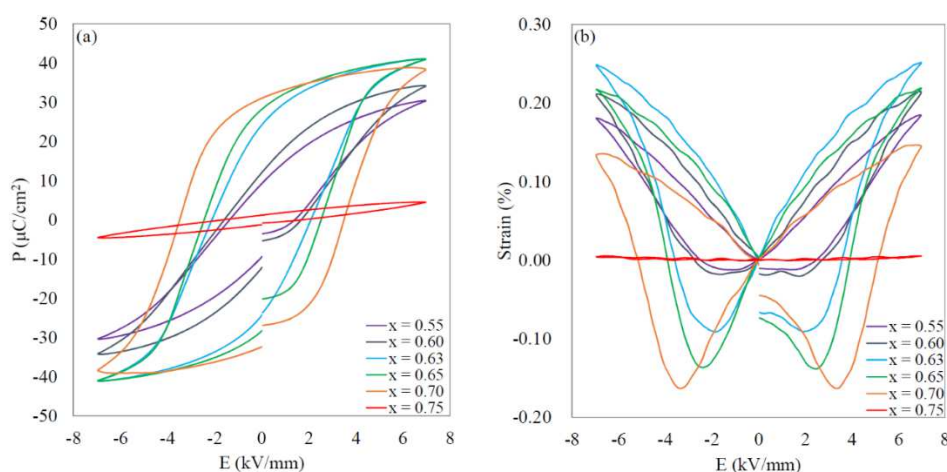


Fig. 6. 10 (a) PE hysteresis loops and (b) bipolar SE curves for  $0.05\text{Bi}(\text{Mg}_{2/3}\text{Nb}_{1/3})\text{O}_3-(0.95-x)\text{BaTiO}_3-(x)\text{BiFeO}_3$  ( $x = 0.55, 0.60, 0.63, 0.65, 0.70, \text{ and } 0.75$ ) ceramics measured at room temperature.

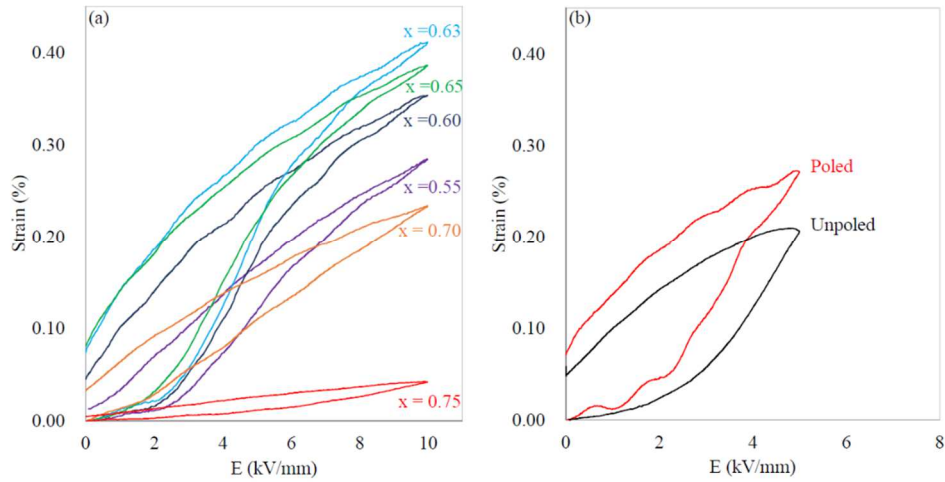


Fig. 6. 11 Unipolar SE curve of (a) unpoled and (b) poled and unpoled samples of  $0.05\text{Bi}(\text{Mg}_{2/3}\text{Nb}_{1/3})\text{O}_3-(0.95-x)\text{BaTiO}_3-x\text{BiFeO}_3$  ( $x = 0.63$ ) ceramics measured at room temperature.

The temperature dependence of the unipolar SE curves and PE curves for poled  $0.05\text{Bi}(\text{Mg}_{2/3}\text{Nb}_{1/3})\text{O}_3-(0.95-x)\text{BaTiO}_3-x\text{BiFeO}_3$  ( $x = 0.63$ ) ceramics measured under an electric field of 6 kV/mm from 25 to 175°C are shown in Fig. 6.11. The strain increased from ~0.27 to ~0.34% at 100 °C and decreased to ~0.30% at 175 °C accompanied by a notable decrease in hysteresis with respect to room temperature measurements. The variation of strain ( $\Delta S$ ) was 25%. Comparison of the variation with PZT and other PbO free materials is given in table 6.3. The results suggest that BMN-BT-BF may have the potential to operate at higher temperatures than typical for PbO-free ceramics which often have low depolarising temperatures or a decrease in piezoactivity as temperature increases.<sup>86, 118, 119, 120, 121</sup>

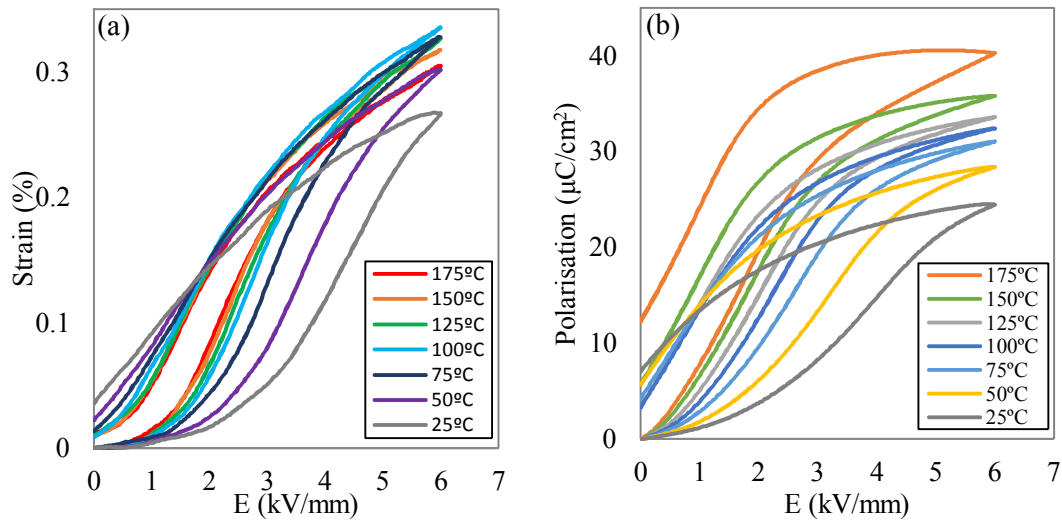


Fig. 6. 12 The temperature dependence of (a) unipolar SE curve (b) PE hysteresis loop for poled  $0.05\text{Bi}(\text{Mg}_{2/3}\text{Nb}_{1/3})\text{O}_3-(0.95-x)\text{BaTiO}_3-(x)\text{BiFeO}_3$  ( $x = 0.63$ ) ceramics measured under an electric field of 6 kV/mm from 25 to 175 °C.

Table 6. 3 Comparison of the temperature dependence of strain ( $\Delta S$ ) for several kinds of piezoelectric ceramics (PZT,  $\text{Bi}_{1/2}\text{K}_{1/2}\text{TiO}_3\text{-BF}$  (BKT-BF),  $\text{Bi}_{1/2}\text{Na}_{1/2}\text{TiO}_3\text{-Bi}_{1/2}\text{K}_{1/2}\text{TiO}_3$  (BNT-BKT), BT-BF, BMN-BT-BF).

Material	Temperature Range	$\Delta S$	Reference
PZT 4	RT-160°C	15%	10
PZT-5H	RT-80°C	>40%	47
0.91BKT-0.09BF	RT-175°C	15%	43
BNT-BKT	RT-190°C	3%	45
0.3BT-0.7BF	RT-150°C	42%	44
0.05BMN-0.32BT-0.63BF	RT-175°C	25%	This work

Fig. 6.13 compares  $d_{33}^*$  calculated from unipolar strain and  $d_{33}$  for poled  $0.05\text{Bi}(\text{Mg}_{2/3}\text{Nb}_{1/3})\text{O}_3-(0.95-x)\text{BaTiO}_3-(x)\text{BiFeO}_3$  ( $x = 0.55, 0.60, 0.63, 0.65, 0.70, \text{ and } 0.75$ ) ceramics. The largest  $d_{33}$  was 148 pC/N for  $x = 0.70$  and the largest  $d_{33}^*$  was 544 pm/V for  $x = 0.63$  at 5 kV/mm. We note that the maximum  $d_{33}$  and  $d_{33}^*$  are not coincident, suggesting that the large strains relate principally to a field induced transition to a ferroelectric state rather than classic extender piezoelectric behaviour.<sup>42, 64, 122, 123-125</sup> A conclusion supported but the absence of evidence of long range polar order in the TEM images (Fig. 6.4(a)) and the pseudocubic

structure in XRD data (Fig. 6.1) for high strain compositions.

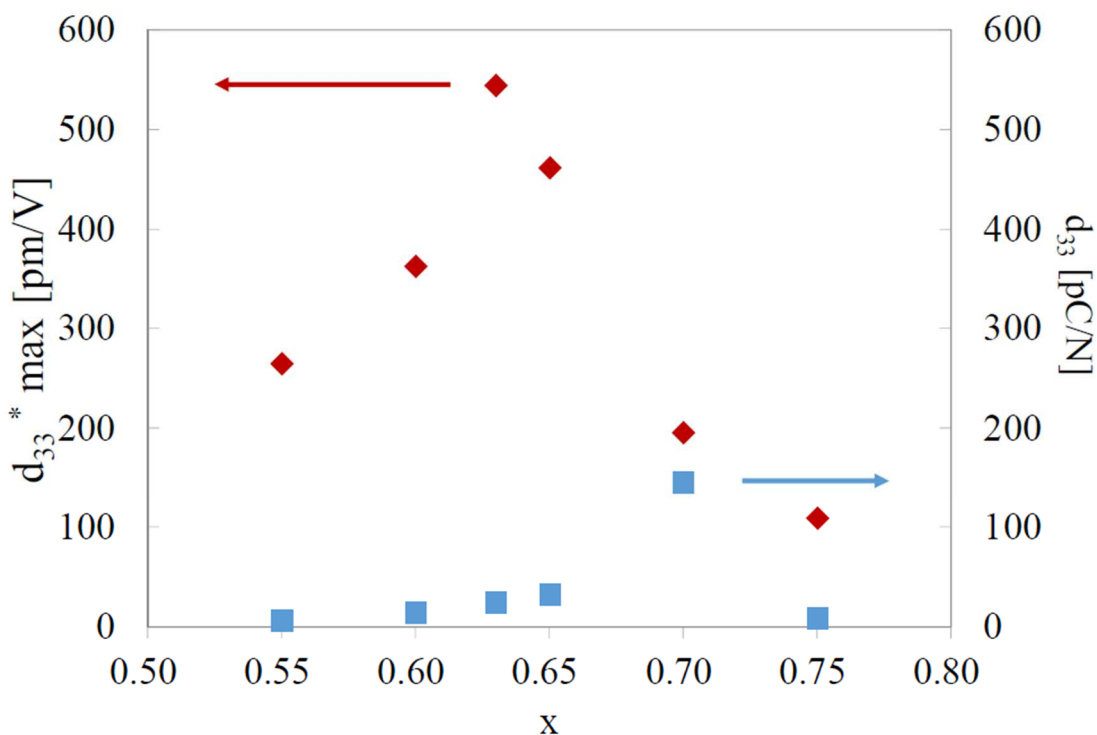


Fig. 6.13 The largest  $d_{33}^*$  calculated from unipolar strain and  $d_{33}$  for  $0.05\text{Bi}(\text{Mg}_{2/3}\text{Nb}_{1/3})\text{O}_3-(0.95-x)\text{BaTiO}_3-(x)\text{BiFeO}_3$  ( $x = 0.55, 0.60, 0.63, 0.65, 0.70,$  and  $0.75$ ) ceramics measured at room temperature.

### 6.2.5 Effect of quenching on $0.05\text{Bi}(\text{Mg}_{2/3}\text{Nb}_{1/3})\text{O}_3-0.20\text{BaTiO}_3-0.75\text{BiFeO}_3$

To investigate the cause of the compositional inhomogeneity for  $0.05\text{Bi}(\text{Mg}_{2/3}\text{Nb}_{1/3})\text{O}_3-(0.95-x)\text{BaTiO}_3-x\text{BiFeO}_3$  ( $x = 0.75$ ), quenched (into liquid  $\text{N}_2$ ) were compared to furnace cooled samples. Fig. 6.14 (a) and (b) show BSE images for polished  $0.05\text{Bi}(\text{Mg}_{2/3}\text{Nb}_{1/3})\text{O}_3-(0.95-x)\text{BaTiO}_3-(x)\text{BiFeO}_3$  ( $x = 0.75$ ) of furnace cooled and quenched samples. For the furnace cooled composition, the core shell structure is apparent in the BSE images but less evident in the quenched sample under identical imaging conditions. Moreover, ferroelectric macrodomains are observed in the quenched but not in the furnace cooled sample, consistent with the *PE* and *SE* loops, Figure 6.15 (a) and (b). We note however, that there is a bright presumably Bi rich phase in the grain boundary of the quenched sample. This might suggest a complex phase equilibrium at the sintering temperature, involving a Bi-rich grain boundary phase in addition to the perovskite matrix phase. It is nonetheless concluded that the

inhomogeneous distribution of constituent ions in the matrix phase was generated during furnace cooling.

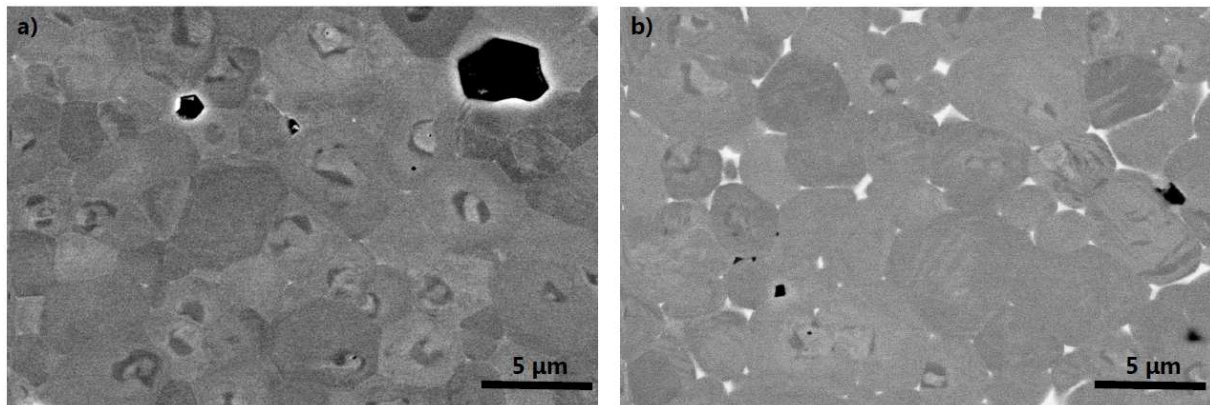


Fig. 6. 14 BSE images of polished surface of (a) furnace cooled and (b) quenched  $0.05\text{Bi}(\text{Mg}_{2/3}\text{Nb}_{1/3})\text{O}_3-(0.95-x)\text{BaTiO}_3-(x)\text{BiFeO}_3$  ( $x = 0.75$ ) ceramics.

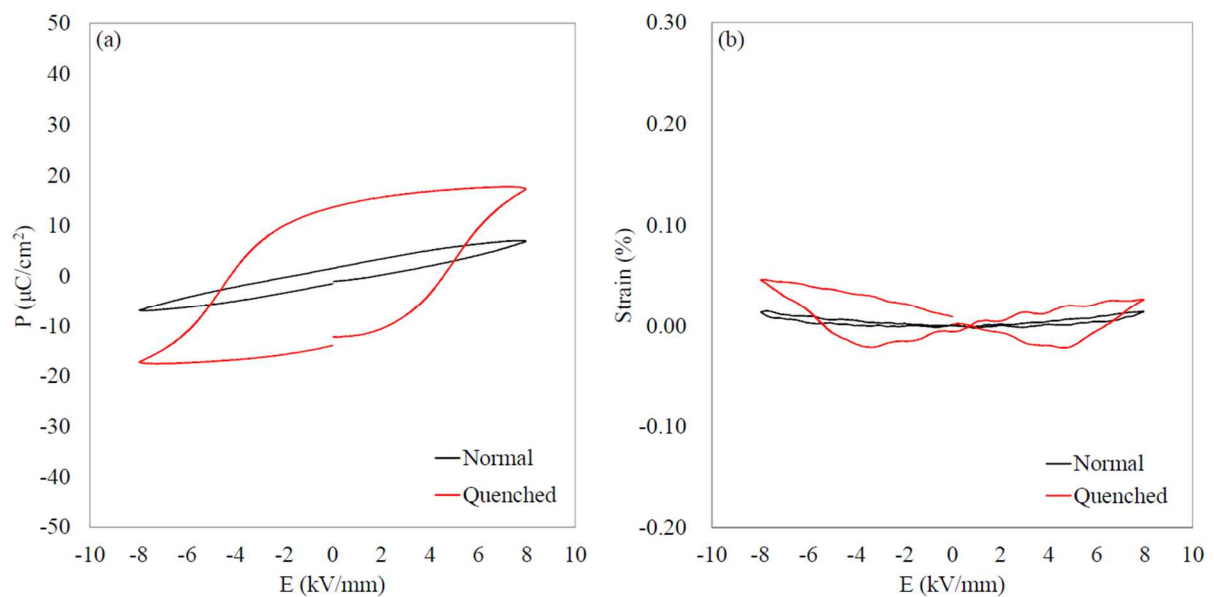


Fig. 6. 15 (a) PE hysteresis loops and (b) bipolar SE curves for furnace cooled and quenched  $0.05\text{Bi}(\text{Mg}_{2/3}\text{Nb}_{1/3})\text{O}_3-(0.95-x)\text{BaTiO}_3-(x)\text{BiFeO}_3$  ( $x=0.75$ ) ceramics measured at room temperature.

PE hysteresis loops and bipolar SE curves for furnace cooled and quenched samples measured at room temperature at 8 kV/mm are shown in Fig. 6.15(a) and 6.15(b). The PE hysteresis loop of the furnace cooled sample is elliptical which indicates that the ceramics have only a weak ferroelectric response but quenched samples show square hysteresis loops typical of a ferroelectric. Moreover, the furnace cooled sample reveals negligible strain in bipolar

measurements but the *SE* curve of the quenched sample shows a butterfly-like shape consistent with a strong ferroelectric/piezoelectric response. It is concluded therefore, that improved homogeneity in the matrix phase for quenched samples results in superior piezoelectric and ferroelectric properties in  $0.05\text{Bi}(\text{Mg}_{2/3}\text{Nb}_{1/3})\text{O}_3-(0.95-x)\text{BaTiO}_3-(x)\text{BiFeO}_3$  ( $x = 0.75$ ) ceramics. The onset of inhomogeneity in the matrix suggests that  $x = 0.75$  cools from a single perovskite phase at the sintering temperature through to a lower temperature region in which two perovskite phases co-exist.

It is noted that the largest strains in the BMN-BT-BF system occur at  $x = 0.63$  at the relaxor-ferroelectric crossover, a composition which remains homogeneous during furnace cooling, i.e. has a single perovskite phase over the entire temperature range from sintering. It is speculated that not only is the  $\text{Mg}_{2/3}\text{Nb}_{1/3}$ , self-compensated dopant important in controlling conductivity in these systems, but it also encourages the formation of a relaxor-ferroelectric point of crossover (high strain/ $d_{33}^*$ ) in compositions which are intrinsically homogeneous (miscible over large temperature ranges), effectively moving the perovskite immiscibility region away from the ‘sweet-spot’ for high strain and large  $d_{33}^*$ , thereby removing the need for quenching, alluded to by several authors.<sup>17, 100</sup>

These novel compositions based on BMN-BT-BF represent an important set of materials in the search for lead free electrostrictors and piezoelectrics. Although their small signal  $d_{33}$  is unsuitable for sensor applications, their large electrostrictive response and high strain (0.4%) are competitive with, or superior to, many lead free piezoelectrics for actuator applications.<sup>6</sup> The inclusion of  $\text{Mg}_{1/3}\text{Nb}_{2/3}$  as stoichiometric co-dopants was initially performed to modify the defect chemistry and reduce conductivity but it is evident from the results presented that  $\text{Mg}^{2+}$  and  $\text{Nb}^{5+}$  on the B-site also affect the correlation length of dipolar coupling and encourage the onset of relaxor rather than ferroelectric behaviour, thus permitting the large dominantly, electrostrictive strains.

BMN-BT-BF is composed of non-toxic and environmentally sustainable elements with the exception of  $\text{Nb}_2\text{O}_5$  but the low wt% in BMN-BT-BF (<2 wt%) in comparison to KNN (60 wt%) ensures that its environmental profile is superior.<sup>56</sup> Compared to NBT, KNN and BCZT there are relatively few studies of BMN-BT-BF based compositions but the large strains and multilayer fabrication for non-quenched compositions demonstrated in this chapter suggest

they are worthy of further investigation.

### 6.3 Conclusions

The relationship between the piezoelectric/electrostrictive properties, the structure and microstructure for  $0.05(\text{Mg}_{2/3}\text{Nb}_{1/3})\text{O}_3-(0.95-x)\text{BaTiO}_3-(x)\text{BiFeO}_3$  ( $x = 0.55, 0.60, 0.63, 0.65, 0.70,$  and  $0.75$ ) ceramics was investigated. XRD revealed that compositions gradually transformed from a pseudocubic ( $Pm-3m$ ) to a rhombohedral ( $R3c$ ) phase as  $x$  increased. BSE images and  $Z''$ ,  $M''$  spectroscopic plots showed that  $x = 0.75$  is chemically heterogeneous and has the greatest electrical inhomogeneity. The temperature dependence of the relative permittivity showed Curie maxima, consistent with a crossover from relaxor-like to ferroelectric behaviour as  $x$  increased with TEM images and polarisation - strain - field behaviour also coherent with this premise. The largest  $d_{33}^*$  was measured at 544 pm/V for  $x = 0.63$  under 5 kV/mm at the crossover from relaxor to ferroelectric behaviour. The temperature dependence for  $x = 0.63$  showed 0.30% strain under an electric field of 6 kV/mm at 175 °C with a notable decrease in hysteresis with respect to room temperature. For  $x = 0.75$ , quenching improved the chemical homogeneity in the perovskite phase and resulted in significantly improved ferroelectric and piezoelectric properties. We propose that not only is the  $\text{Mg}_{2/3}\text{Nb}_{1/3}$ , self-compensated dopant important in controlling conductivity in BT-BF based systems, but also encourages a relaxor-ferroelectric point of cross over in compositions which are miscible over large temperature ranges, effectively moving the immiscibility region away from the 'sweet-spot' for high strain and large  $d_{33}^*$ , thereby removing the need for quenching.

## Chapter 7: 0.05BiScO<sub>3</sub>-(0.95-x)BaTiO<sub>3</sub>-(x)BiFeO<sub>3</sub> based ceramics

### 7.1 Introduction

Following the results of chapter 6 and 7, the further investigation on 0.05BiScO<sub>3</sub>-(0.95-x)BaTiO<sub>3</sub>-(x)BiFeO<sub>3</sub> (BS-BT-BF,  $x = 0.55, 0.60, 0.625, 0.65,$  and  $0.70$ ) ceramics was encouraged to know the difference of dopant effects between (Mg<sub>2/3</sub>Nb<sub>1/3</sub>)<sup>3+</sup> and Sc<sup>3+</sup>. Since the tolerance factor and the electronegativity difference of (Mg<sub>2/3</sub>Nb<sub>1/3</sub>)<sup>3+</sup> and Sc<sup>3+</sup> are very close, the piezoelectric and dielectric properties are predicted to be similar. BiScO<sub>3</sub> has been used as an end member to form MPB with several piezoelectric materials such as BT, KNN, and PbTiO<sub>3</sub>.<sup>126-129</sup> BiScO<sub>3</sub> is not a stable end member compound and only forms under high pressure but it is considered as a rhombohedral-like material in the context of piezoelectrics, similar to BiFeO<sub>3</sub>. Here, the objective is to determine whether BiScO<sub>3</sub> is a useful substituent in BF-BT to optimise piezoelectric properties in a single phase compound, as predicted from the results described in Section 5 on 0.05BS-0.25BT-0.70BF.

### 7.2 Results and Discussion

#### 7.2.1 XRD Analysis

To further investigate dopant effects in BT-BF systems, the relationship between the piezoelectric/ferroelectric properties and the microstructure for 0.05BiScO<sub>3</sub>-(0.95-x)BaTiO<sub>3</sub>-(x)BiFeO<sub>3</sub> (BS-BT-BF,  $x = 0.55, 0.60, 0.625, 0.65,$  and  $0.70$ ) ceramics was investigated. Fig. 7.1 shows the XRD diffractograms of the BS-BT-BF ceramics. On visual inspection, all XRD patterns are attributed to a single perovskite phase without any secondary phase peaks. To determine the most probable structure for each data set, Rietveld refinements were conducted and the results summarised in Table 7.1. All XRD patterns were refined using a combination of pseudocubic (*Pm-3m*) and rhombohedral (*R3c*) cells. For  $x = 0.55$  to  $0.65$ , the ratio of *R3c/Pm-3m* is dominated by *Pm-3m* but for  $x = 0.70$  *R3c* dominates, consistent with most previous observations<sup>18, 22, 115</sup> although some authors refer to the presence of monoclinic or tetragonal symmetries.<sup>17, 19</sup>

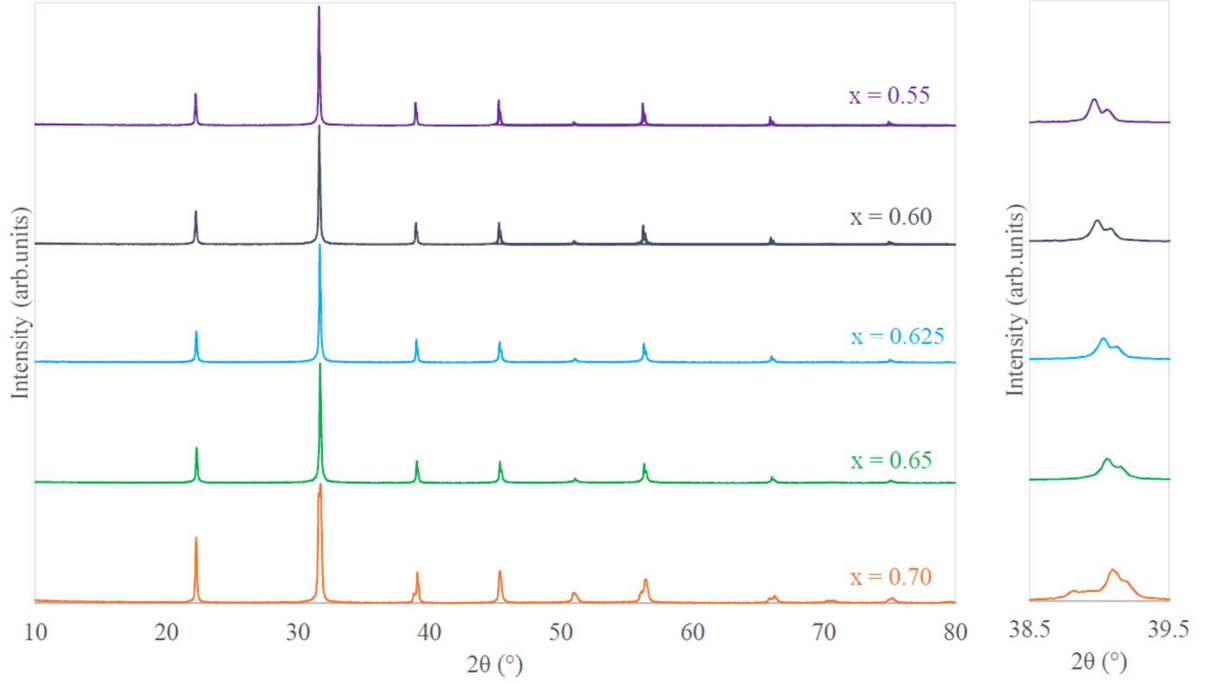


Fig. 7. 1 Powder XRD patterns for  $0.05\text{BiScO}_3-(0.95-x)\text{BaTiO}_3-(x)\text{BiFeO}_3$  ( $x = 0.55, 0.60, 0.625, 0.65,$  and  $0.70$ ) ceramics measured at room temperature.

Table 7. 1 Lattice parameters ( $a, b, c$ ), fraction of phase (wt%), and fitting parameters ( $R_{wp}, R_p,$  and  $\chi^2$ ) for  $0.05\text{BiScO}_3-(0.95-x)\text{BaTiO}_3-(x)\text{BiFeO}_3$  ( $x = 0.55, 0.60, 0.625, 0.65,$  and  $0.70$ ) ceramics measured at room temperature.

$x$	Space group	Lattice parameters			Weight (%)	R-factors		
		$a$ (Å)	$b$ (Å)	$c$ (Å)		$R_{wp}$ (%)	$R_p$ (%)	$\chi^2$
0.55	$Pm-3m$	4.0059(7)	4.0059(7)	4.0059(7)	89.3	9.44	7.39	1.47
	$R3c$	5.6695(8)	5.6695(8)	13.8662(3)	10.7			
0.60	$Pm-3m$	4.0027(8)	4.0027(8)	4.0027(8)	87.1	9.74	7.73	1.64
	$R3c$	5.7154(6)	5.7154(6)	14.0559(6)	12.9			
0.625	$Pm-3m$	4.0039(4)	4.0039(4)	4.0039(4)	94.8	9.94	7.89	1.74
	$R3c$	5.6054(4)	5.6054(4)	13.7375(2)	5.2			
0.65	$Pm-3m$	4.0017(4)	4.0017(4)	4.0017(4)	91.3	10.65	8.53	2.04
	$R3c$	5.6089(3)	5.6089(3)	13.7112(6)	8.7			
0.70	$Pm-3m$	4.0006(0)	4.0006(0)	4.0006(0)	25.2	8.29	6.36	1.94
	$R3c$	5.6377(5)	5.6377(5)	13.9112(3)	74.8			

## 7.2.2 Microstructure

BSE images for the  $0.05\text{BiScO}_3-(0.95-x)\text{BaTiO}_3-(x)\text{BiFeO}_3$  are illustrated as a function of  $x$  in Fig. 7.2. All samples generally show uniform contrast within the grains, indicating they

are compositionally homogeneous with few core-shell structures, thus confirming the prediction and experimental data that Sc is an excellent substituent into the BT-BF system.

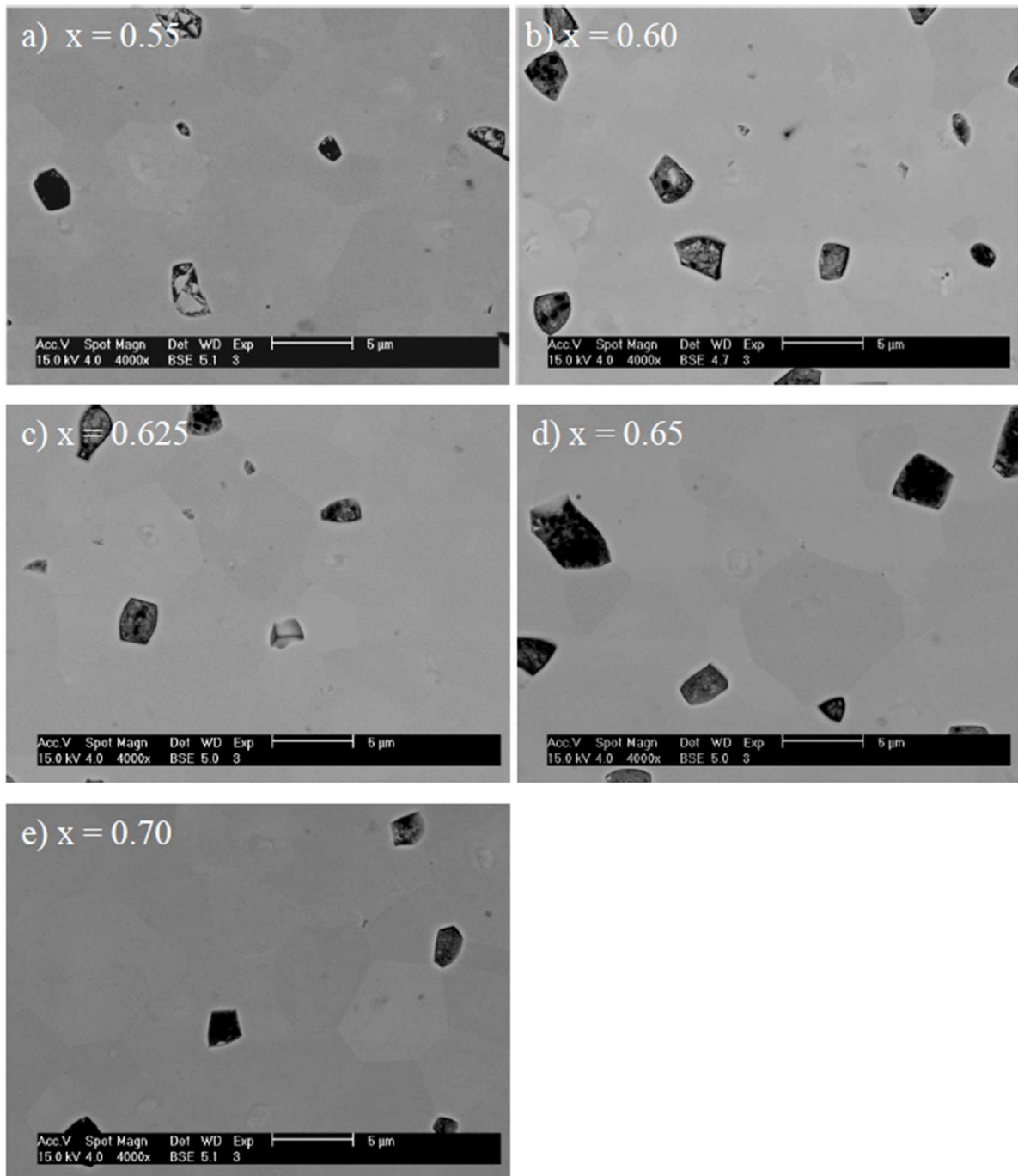


Fig. 7. 2 BSE images of polished surface of  $0.05\text{BiScO}_3-(0.95-x)\text{BaTiO}_3-(x)\text{BiFeO}_3$  ceramics.

To evaluate the electrical homogeneity, impedance spectroscopy (IS) analysis was conducted. Spectroscopic plots of  $Z''$  and  $M''$  extracted from IS data can be used as a simple way to qualitatively assess electrical homogeneity. Fig 7.3 (a-e) show  $Z''$  and  $M''$  spectroscopic

plots for  $0.05\text{BiScO}_3-(0.95-x)\text{BaTiO}_3-(x)\text{BiFeO}_3$  ceramics. For  $x = 0.55$  to  $0.65$ , data are shown for  $320^\circ\text{C}$  whereas for  $x = 0.70$ , the data are shown for  $243^\circ\text{C}$  to allow the  $Z''$  and  $M''$  spectra to be observed and compared with the other ceramics. All the  $M''$  spectra show a low frequency peak with an  $f_{max}$  value that is similar to the large  $Z''$  peak but there are clearly further  $M''$  peaks at intermediate and higher frequencies. The presence of multiple  $M''$  peaks means all samples have two or more electrical phases present, most likely relating to either grain boundary, shell or core regions. The capacitance values calculated from the single  $Z''$  Debye peak measured at  $320^\circ\text{C}$  for  $0.05\text{BiScO}_3-(0.95-x)\text{BaTiO}_3-(x)\text{BiFeO}_3$  ceramics are shown in Table 7.2. For  $x = 0.55$  to  $0.65$ , the capacitance values are  $\sim 1.2$  to  $2.8$  nF/cm consistent with a grain boundary type response but the capacitance decreases to  $0.29$  nF/cm for  $x = 0.70$ . This capacitance decrease implies that the main electrical (conduction) path in the ceramics changes from being a grain boundary-type response to a shell-type response at  $x = 0.70$  but further analyses are required to confirm this assignment. A comparison of  $\epsilon_r$  calculated using the capacitance from  $Z''$  peak and that using the capacitance measured by LCR meter, is given in Table 7.2. The agreement is not exact because the frequencies at which they are measured are different and space charge as well dipolar polarization contributes to  $\epsilon_r$  at lower frequencies. Further investigations including revealing the entire spectrum of  $M''$  are required to understand the electric properties of these systems.

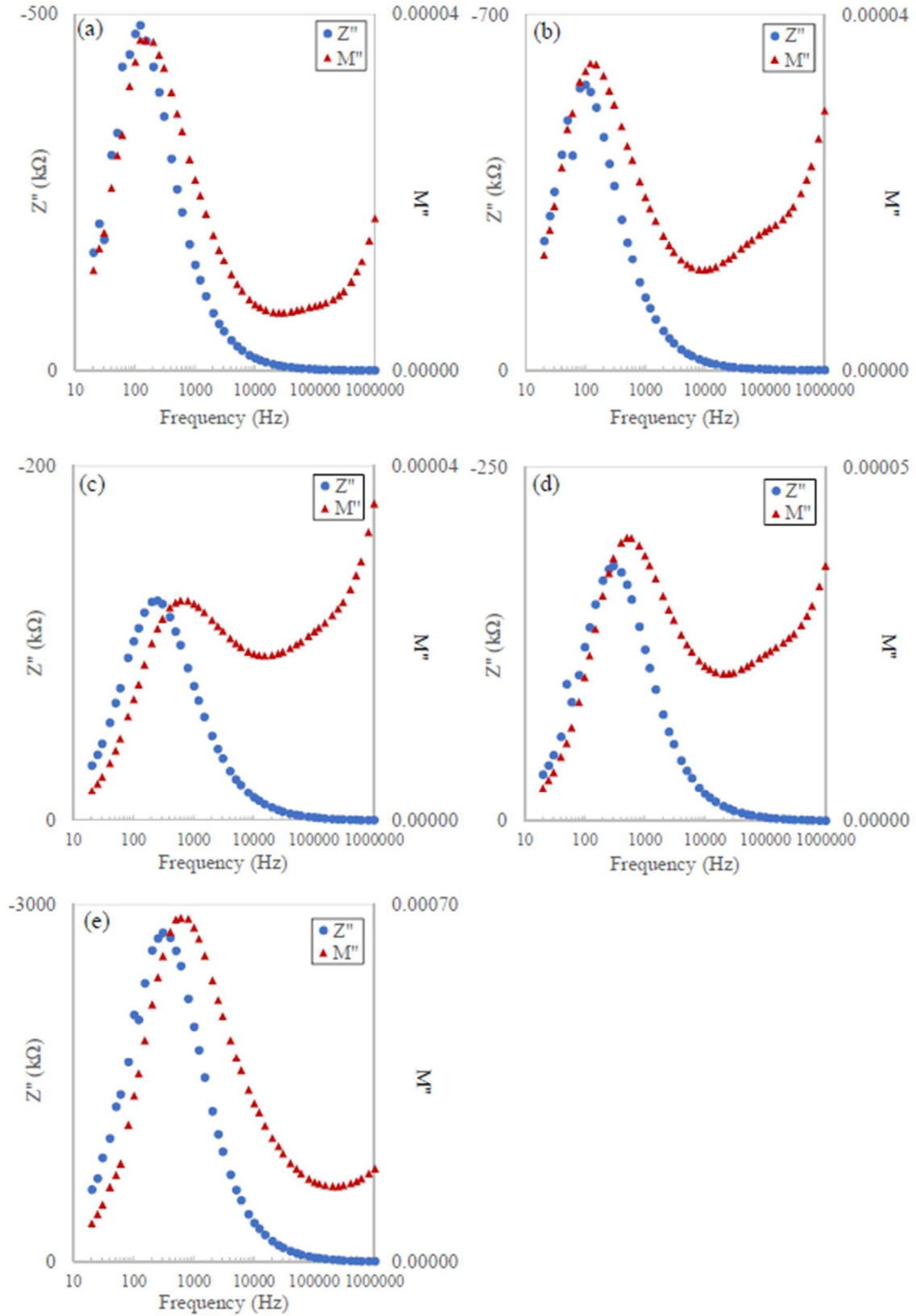


Fig. 7.3 Combined  $Z''$  and  $M''$  spectroscopic plots for  $0.05\text{BiScO}_3-(0.95-x)\text{BaTiO}_3-(x)\text{BiFeO}_3$  ceramics with  $x =$  (a) 0.55, (b) 0.60, (c) 0.625, (d) 0.65 measured at 320°C, and (f) 0.70 measured at 243°C.

Table 7. 2 Capacitance measured at 320°C and activation energy for the 0.05BiScO<sub>3</sub>-(0.95-x)BaTiO<sub>3</sub>-(x)BiFeO<sub>3</sub> ceramics.

x	Capacitance at 320°C C(nF/cm)	Activation Energy $E_a$ (eV)	$\epsilon_r$ calculated by Capacitance from Z'' peak	$\epsilon_r$ calculated by Capacitance measured by LCR meter
0.55	1.37	1.10	21420	10876
0.60	1.21	1.16	18200	13051
0.625	2.78	1.15	35810	11650
0.65	1.47	1.14	18790	7080
0.70	0.29	1.10	4010	2379

The large, single Z'' Debye peak was used to calculate the total resistivity of the ceramics and the inverse of this value used to estimate the total electrical conductivity. An Arrhenius plot of the total conductivity for 0.05BiScO<sub>3</sub>-(0.95-x)BaTiO<sub>3</sub>-(x)BiFeO<sub>3</sub> ceramics is shown in Fig. 7.4 and the activation energy ( $E_a$ ) calculated from these data are shown in Table 7.2. Fig. 7.4 shows the conductivity increases from  $x = 0.55$  to 0.70 and Table 3 reveals all samples have approximately the same  $E_a$  of ~ 1.1 to 1.2 eV, indicating that their conduction mechanisms are similar.

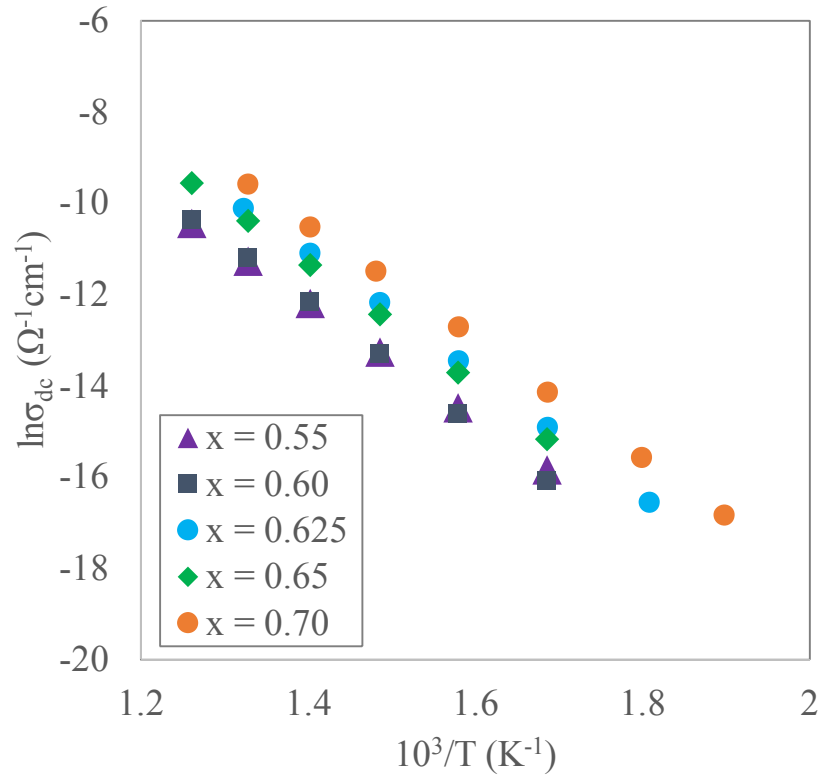


Fig. 7. 4 Arrhenius plot of electrical conductivity for  $0.05\text{BiScO}_3-(0.95-x)\text{BaTiO}_3-(x)\text{BiFeO}_3$  ceramics.

### 7.2.3 Temperature dependence of relative permittivity ( $\epsilon_r$ ) and $\tan\delta$

The temperature dependence of  $\epsilon_r$  and  $\tan\delta$  for the  $0.05\text{BiScO}_3-(0.95-x)\text{BaTiO}_3-(x)\text{BiFeO}_3$  ceramics measured at 10 kHz are shown in Fig. 7.5 (a) and 7.5 (b). For  $x = 0.55$  (Fig. 7.5 (a)), the dielectric anomaly is consistent with a relaxor-like transition and concomitant with the dominant pseudocubic structure refined from the XRD data. As  $x$  increases to 0.65, the dielectric anomalies become sharp and the temperature where the permittivity maximum shifts to higher temperature. For  $x = 0.70$ , there is more than one anomaly.  $\tan\delta$  for all compositions at room temperature is  $\sim 0.1$  and  $\tan\delta$  for  $0.55 \leq x \leq 0.65$  does not increase significantly until  $> 300^\circ\text{C}$  which is encouraging for high temperature applications. However, for  $x = 0.70$  the onset of the sharp increase in dielectric loss shifts to lower temperatures consistent with conductivity data obtained by impedance spectroscopy.

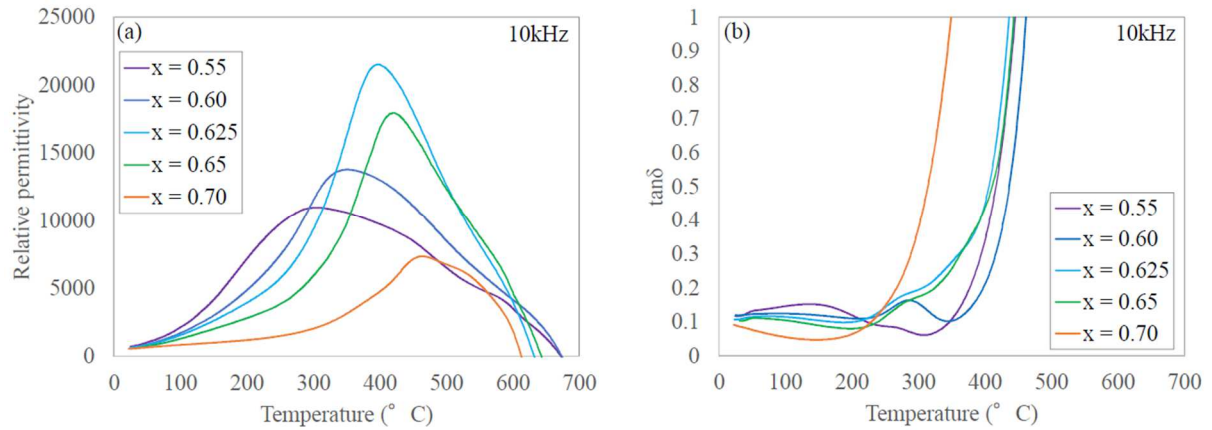


Fig. 7. 5 Temperature dependence of (a) relative permittivity and (b) dielectric loss,  $\tan\delta$  for 0.05BiScO<sub>3</sub>-(0.95-x)BaTiO<sub>3</sub>-(x)BiFeO<sub>3</sub> ceramics.

The frequency dependence from 1kHz to 250kHz of  $\epsilon_r$  and  $\tan\delta$  for the 0.05BiScO<sub>3</sub>-(0.95-x)BaTiO<sub>3</sub>-(x)BiFeO<sub>3</sub> ( $x = 0.55, 0.625, 0.70$ ) ceramics are shown in Fig. 7.6 (a)-(c). With increasing frequency, the  $\epsilon_r$  maximum shifts to higher temperature and is suppressed in all the compositions. The onset temperature where  $\tan\delta$  increases also shifts to higher temperature. It is concluded therefore that these samples have a nature of relaxor.

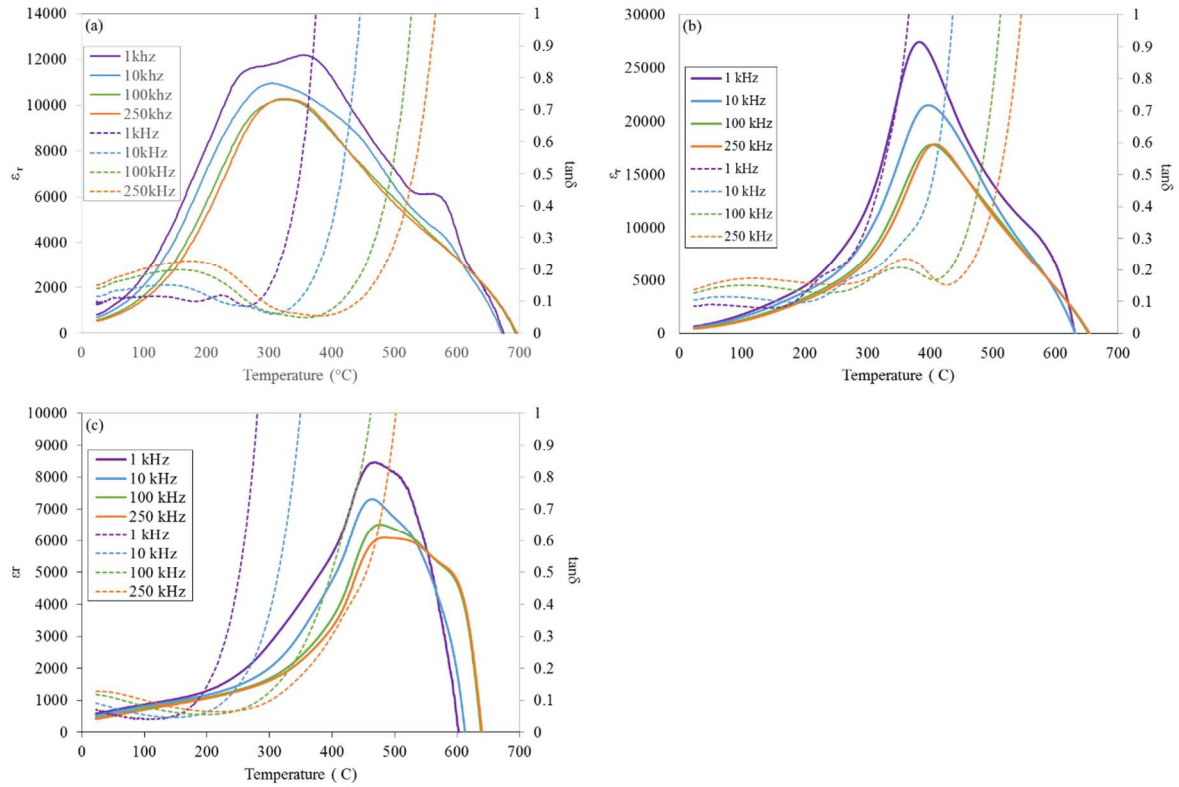


Fig. 7. 6 Frequency dependence of (a) relative permittivity and (b) dielectric loss,  $\tan\delta$  vs temperature for  $0.05\text{BiScO}_3-(0.95-x)\text{BaTiO}_3-(x)\text{BiFeO}_3$  ( $x =$  (a) 0.55, (b) 0.625, (c) 0.70) ceramics.

## 7.2.4 Ferroelectric and piezoelectric properties

PE hysteresis loops and bipolar SE curves for  $0.05\text{BiScO}_3-(0.95-x)\text{BaTiO}_3-(x)\text{BiFeO}_3$  ceramics were measured under an electric field of 7 kV/mm at room temperature (Fig. 7.7 (a) and Fig. 7.7 (b)). PE hysteresis loops show a change from a narrow loop typical of electrostrictive compositions with limited or no long-range ferroelectricity to a classic ferroelectric square loop as  $x$  increases, consistent with the increase in volume fraction of the R3c phase. A similar trend is observed for bipolar strain field measurements which transform from loops typical of dominant electrostrictive behaviour (negligible negative strain) to classic butterfly loops typical of a long-range ordered ferroelectric. Unipolar SE curves for the  $0.05\text{BiScO}_3-(0.95-x)\text{BaTiO}_3-(x)\text{BiFeO}_3$  ceramics measured under 5 kV/mm at room temperature are shown in Fig. 7.8. The largest  $d_{33}^*$  (465 pm/V at  $x = 0.625$ ), was obtained at the point of crossover from dominant relaxor, electrostrictive ( $x = 0.55$ ) to ferroelectric behaviour ( $0.60 \leq x \leq 0.70$ ), a trend previously observed in BMN/Nd doped BT-BF<sup>116</sup> and Pb-

free systems based on NBT and/or  $(K_{0.5}Bi_{0.5})TiO_3$  (KBT).<sup>19, 71, 117, 118</sup>

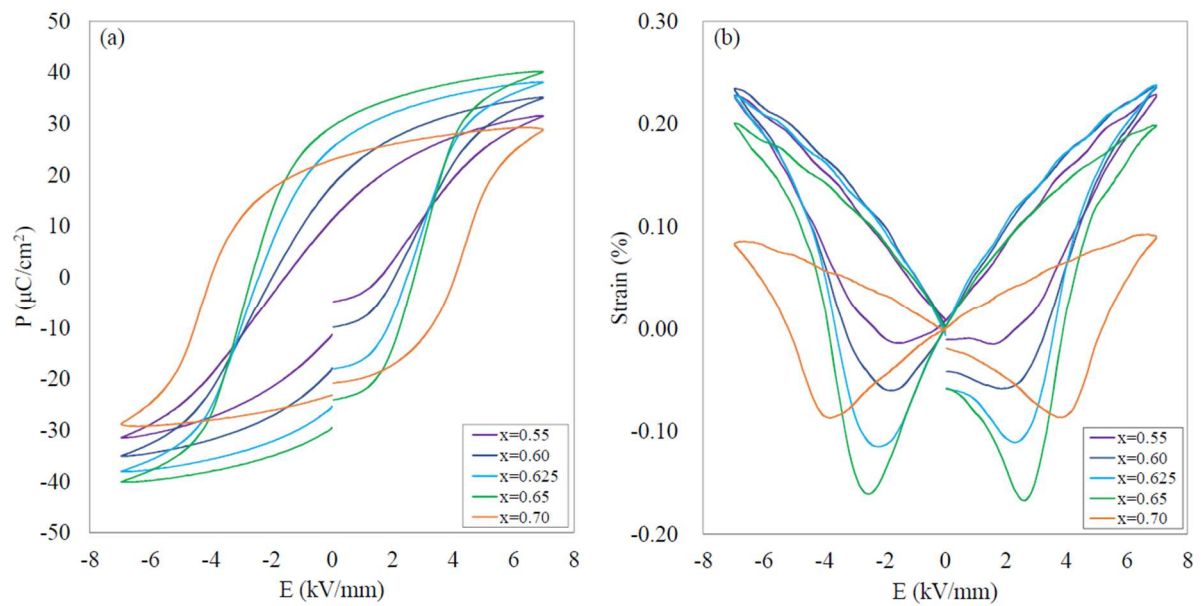


Fig. 7. 7 (a) PE hysteresis loops and (b) bipolar SE curves for  $0.05BiScO_3-(0.95-x)BaTiO_3-(x)BiFeO_3$  ceramics measured at room temperature.

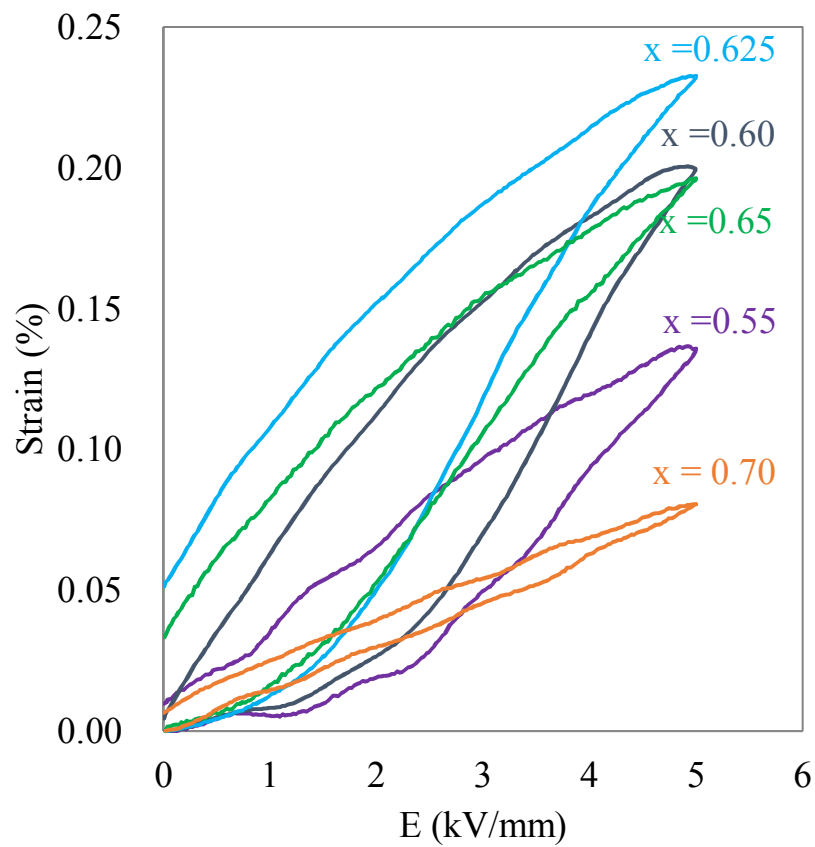


Fig. 7. 8 Unipolar SE curves for  $0.05BiScO_3-(0.95-x)BaTiO_3-(x)BiFeO_3$  ceramics measured at room temperature.

The temperature dependence of the unipolar SE curves for poled  $0.05\text{BiScO}_3\text{-(}0.95\text{-}x\text{)BaTiO}_3\text{-(}x\text{)BiFeO}_3$  ( $x = 0.63$ ) ceramics measured under an electric field of 6 kV/mm from 25 to 175°C are shown in Fig. 7.9. The strain increased from  $\sim 0.27$  to  $\sim 0.35\%$  at 150 °C and remained at  $\sim 0.35\%$  at 175°C, accompanied by a notable decrease in hysteresis with respect to room temperature measurements. The variation of strain ( $\Delta S$ ) was 31%. However, the PE curve at 175 °C became rounded, indicating the sample turns to be leaky, which is different from the results of BMN-BT-BF as shown in Fig. 6.11 (b). These results suggest that BS-BT-BF may have the potential to operate at higher temperatures than typical for PbO-free ceramics which often have low depolarising temperatures or a decrease in piezoactivity as temperature increases.<sup>86, 118-121</sup>

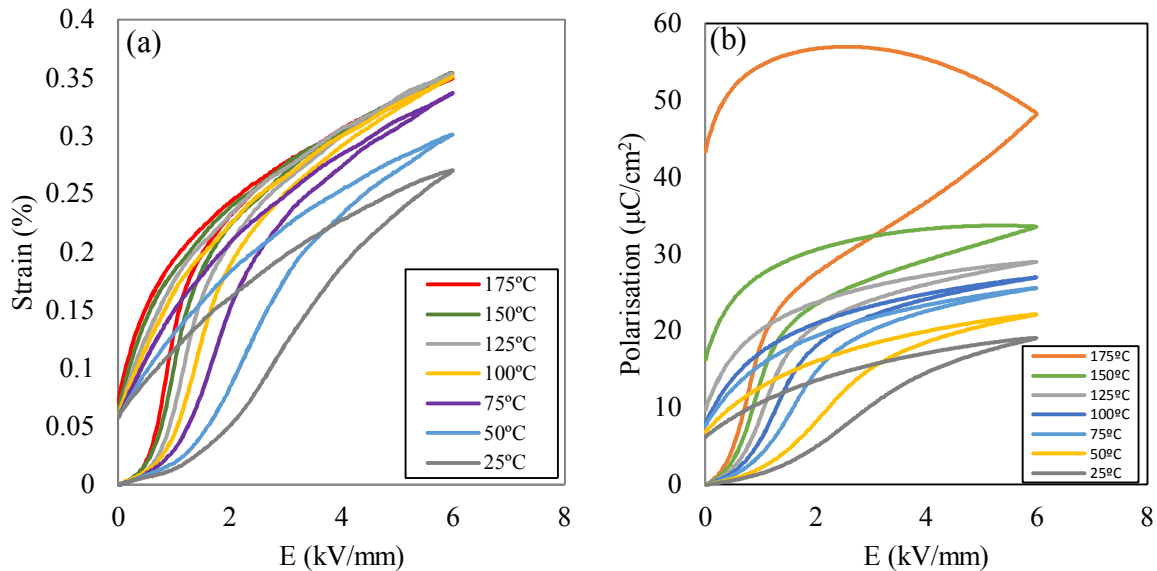


Fig. 7. 9 Temperature dependence of unipolar (a) SE curves and (b) PE curves for  $0.05\text{BiScO}_3\text{-}0.325\text{BaTiO}_3\text{-}0.625\text{BiFeO}_3$  ceramics measured under an electric field of 6 kV/cm at from 25 to 175°C.

### 7.2.5 Comparing with the properties for BMN-BT-BF ceramics

To tell the difference of effects between a self-compensated and an isovalent dopant, the properties of  $\text{Mg}_{2/3}\text{Nb}_{1/3}$ -doped and Sc-doped BT-BF systems are compared. Fig. 7.10 shows the relative density for BMN-BT-BF and BS-BT-BF. For all the samples except  $x = 0.55$ , Sc-doped samples have a lower relative density than  $\text{Mg}_{2/3}\text{Nb}_{1/3}$ -doped samples although both samples have uniform microstructure and a single-phase crystal structure. Especially for  $x = 0.65$  and  $0.70$ , the relative densities of Sc-doped samples are much smaller than the  $\text{Mg}_{2/3}\text{Nb}_{1/3}$ -

doped. For Sc-doped samples, there was a also gap between peak position of  $Z''$  and  $M''$  for  $x = 0.625$  to  $0.70$  as shown in Fig. 7.3 while the gap for  $Mg_{2/3}Nb_{1/3}$ -doped was much less, as shown in Fig. 6.4. These two results imply that  $Mg_{2/3}Nb_{1/3}$ -doped samples are more mechanically stable and electrically uniform. Fig. 7.11 shows  $d_{33}^*$  for BMN-BT-BF and BS-BT-BF as a function of  $x$ , BF ratio. At  $x = 0.625/0.63$  and  $0.65$ , the crossover from relaxor to ferroelectric, the  $d_{33}^*$  of  $Mg_{2/3}Nb_{1/3}$ -doped samples are clearly larger than Sc-doped samples. Also Fig. 7.12 shows  $d_{33}^*$  for BMN-BT-BF and BS-BT-BF as a function of  $x$  where  $d_{33}$  of BS-BT-BF is even larger than those of BMN-BF-BT. Moreover, for  $x = 0.55$  to  $0.65$ ,  $k_p$  and  $Q_m$  of BMN-BT-BF are smaller than those of BS-BT-BF as shown in Fig. 7.13 and Fig. 7.14. These results indicate  $Mg_{2/3}Nb_{1/3}$  shows enhanced electrostrictive behavior in the BT-BF systems in comparison to Sc doped samples.

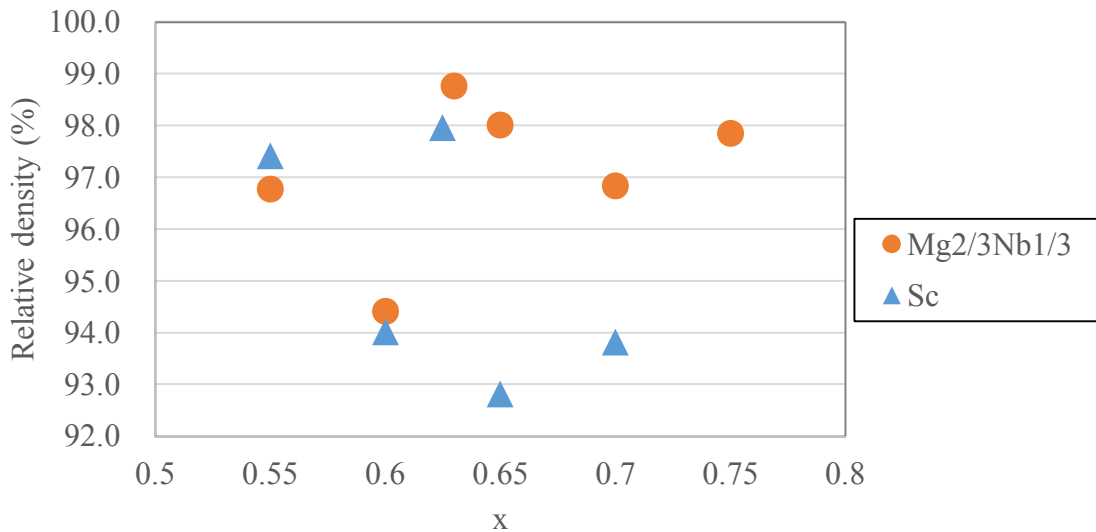


Fig. 7. 10 Relative densities for BMN-BT-BF and BS-BT-BF ceramics.

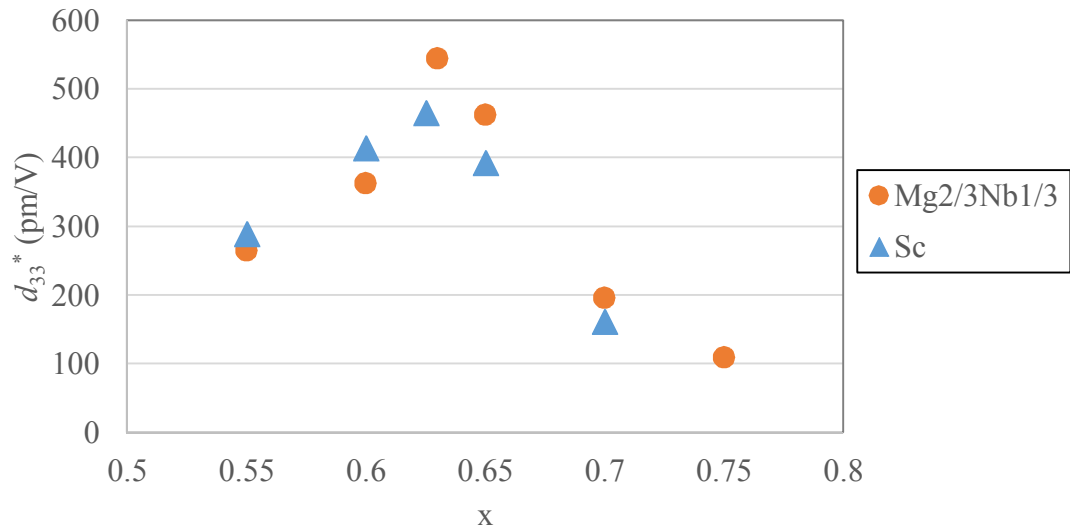


Fig. 7. 11  $d_{33}^*$  for poled BMN-BT-BF and BS-BT-BF ceramics.

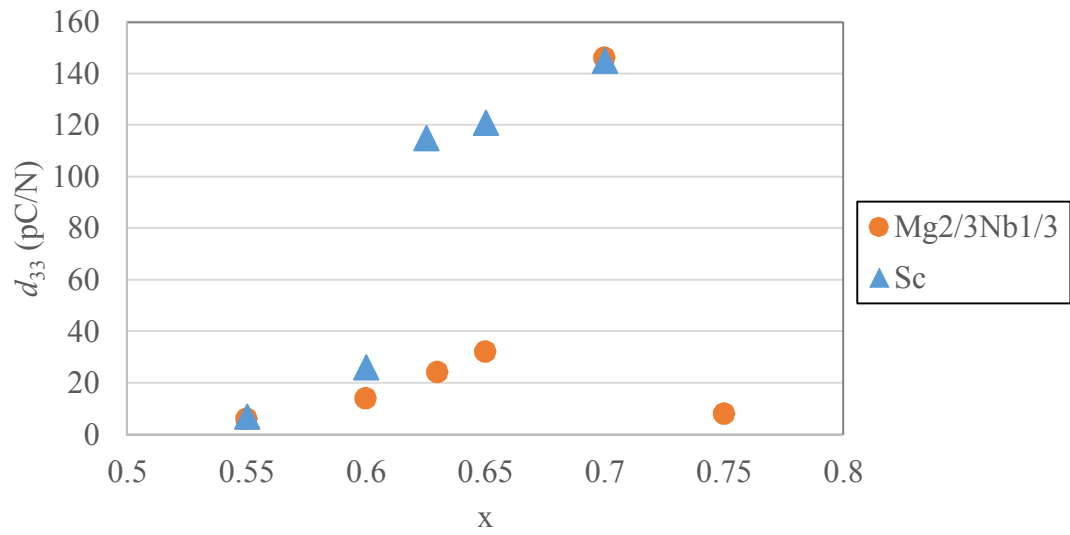


Fig. 7. 12  $d_{33}$  for poled BMN-BT-BF and BS-BT-BF ceramics.

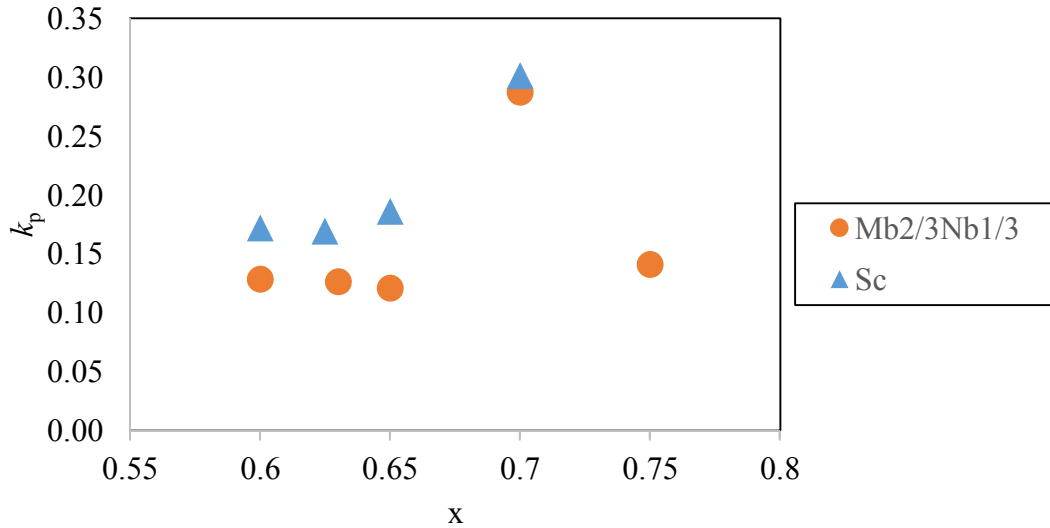


Fig. 7. 13  $k_p$  for poled BMN-BT-BF and BS-BT-BF ceramics.

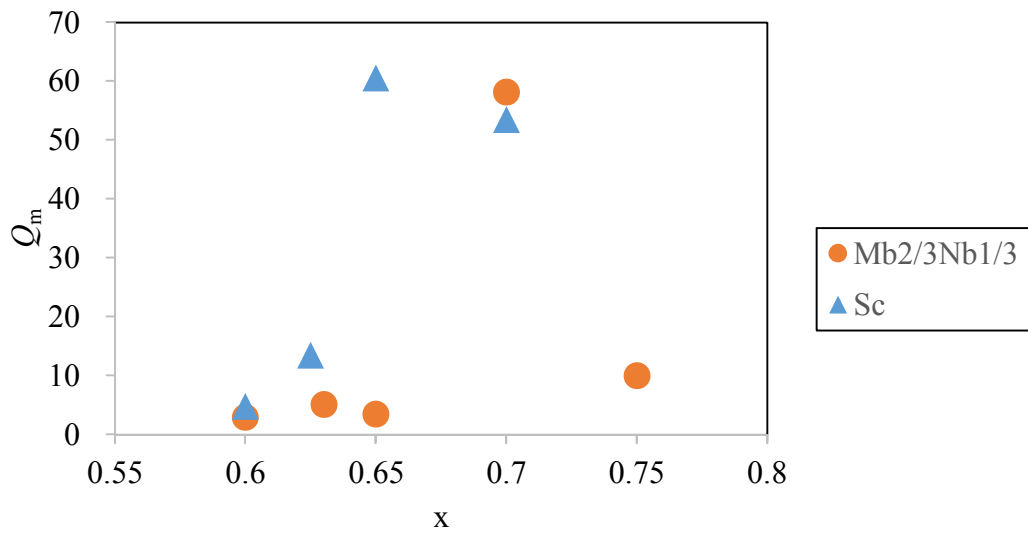


Fig. 7. 14  $Q_m$  for poled BMN-BT-BF and BS-BT-BF ceramics.

### 7.3 Conclusion

As predicted, XRD patterns and BSE images of Sc-doped compositions with  $0.55 \leq x \leq 0.70$  revealed a perovskite structure with no evidence of secondary phases. As  $x$  increased, the phase assemblage gradually changed from dominant pseudocubic ( $Pm-3m$ ) to rhombohedral ( $R3c$ ), consistent with the PE hysteresis loops and SE curves. The largest  $d_{33}^*$  of  $\sim 465$  pm/V was

measured for  $x = 0.625$  at 5 kV at the crossover from relaxor to ferroelectric behaviour. The temperature dependence for  $x = 0.625$  showed 0.35% strain under an electric field of 6 kV/mm at 175°C with a notable decrease in hysteresis with respect to room temperature. Compared the properties of BS-BT-BF with those of BMN-BT-BF, BMN-BT-BF shows slightly higher relative density and greater electrical homogeneity. As a result, BMN-BT-BF systems show greater electrostrictive behavior

## Chapter 8: Multilayer Actuator (MLA) for $0.05\text{Bi}(\text{Mg}_{2/3}\text{Nb}_{1/3})\text{O}_3\text{-}0.63\text{BaTiO}_3\text{-}0.32\text{BiFeO}_3$

### 8.1 Introduction

To determine the potential of ceramics, it is very important to demonstrate a prototype device of any target material. Here, a prototype multilayer actuator (MLA) is targeted to illustrate the potential of the BT-BF compositions developed in Chapters 6 and 7.<sup>28</sup> Multilayer devices can increase total capacitance, reduce the size, save electrical power but for MLAs greatest merit is lowering of the driving electric field, resulting in energy saving and accompanied by an increase in the total displacement. For an MLA with  $n$  ceramic layers (shown in Fig. 8.1), as the thickness of the ceramics layer reduce from  $t$  to  $t/n$ , driving voltage decreases from  $V$  to  $V/n$  to gain the same magnitude of strain as a monolithic ceramic achieves.<sup>28</sup>

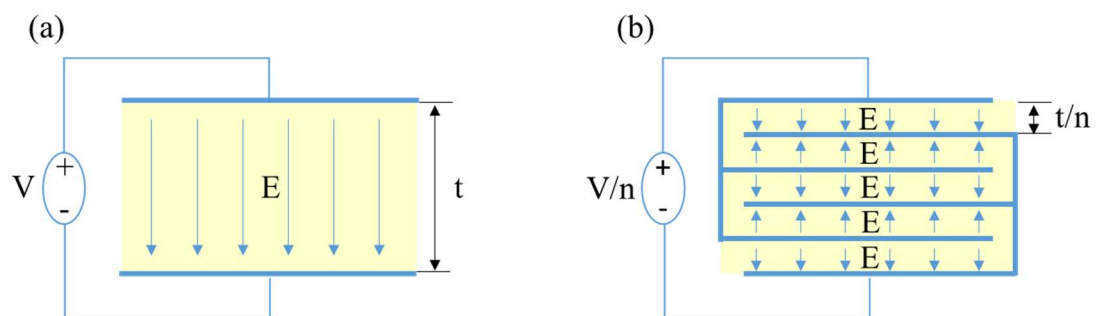


Fig. 8. 1 (a) monolithic piezoelectric component, (b) multilayer piezoelectric component.

The most efficient way of multilayering is the “co-fired method” where the laminated ceramics layers and internal electrodes are fired at the same time.<sup>130</sup> It makes it possible to save manufacturing time and meet the demand of large scale production.<sup>131</sup> In this project, the prototype manufacturing of an MLA was conducted using this co-fired method and the composition of  $0.05\text{Bi}(\text{Mg}_{2/3}\text{Nb}_{1/3})\text{O}_3\text{-}0.32\text{BaTiO}_3\text{-}0.63\text{BiFeO}_3$  was chosen since it had the highest strain, 0.41% at room temperature.

## 8.2 MLA processing

The schematic of MLA processing is shown in Fig. 8.2.<sup>132</sup> In brief, a slurry is first formed where the from a complex set of binders and solvents different from that of bulk ceramics. Second green sheets are fabricated using tape casting followed by printing of the internal electrodes on the green sheets. The electroded green sheets are stacked and laminated. Individual actuators are then cut from the laminate followed by binder burnout and sintering. Finally, the electrode terminations are added.

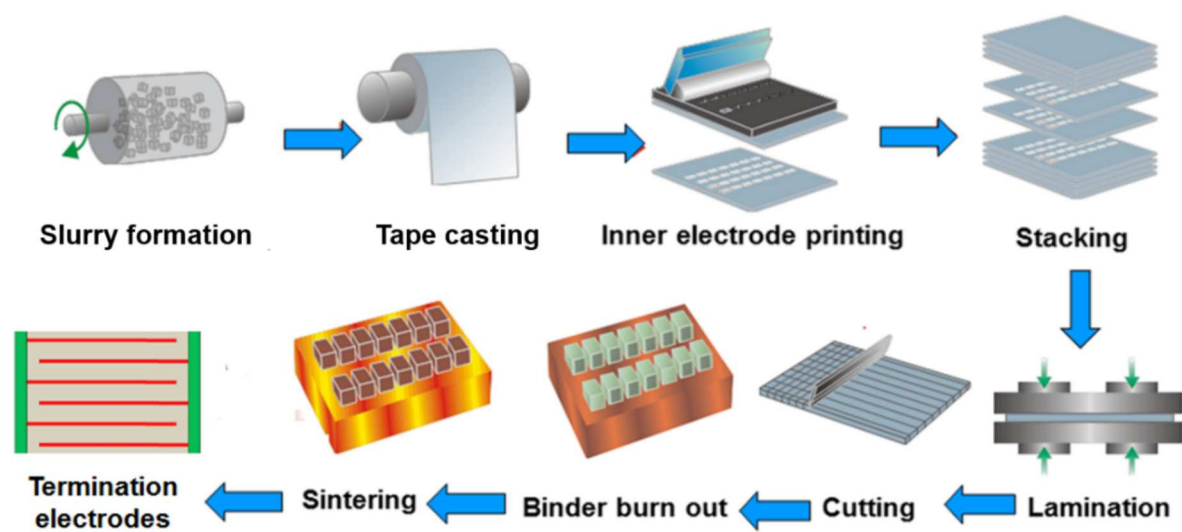


Fig. 8. 2 Schematic of MLA fabrication (Adapted from Ref. 5)

### 8.2.1 Slurry formation

Calcined and attrition milled powder are combined with a binder to form the slurry for MLAs. In this project, the following ingredients were used to optimize the MLA process in Table 8.1. The powder and those organic ingredients were mixed using Speed-mixer DAC 800 FVZ (Hauschild Engineering).

Table 8. 1 Organic contents for slurry.

Contents	Description	Weight (%) of powder
Solvent	Ethyl methyl ketone (Fisher Chemical)	54
Dispersant and Binder	Poly(propylene carbonate) (EMPOWER Materials)	9.0
Plasticizer	Butyl benzyl phthalate (Sigma-Aldrich)	1.4

### 8.2.2 Tape Casting

The slurry was cast onto silicon coated polyethylene terephthalate (PET) carrier film using a Mistler TCC-1200 with a single doctor blade and dried at room temperature for 1 h, which is called green sheets. A schematic illustration of tape casting process is shown in Fig. 8.3. The gap between the tip of the doctor blade and PET carrier film and the speed of moving the film are adjusted to make the target thickness of the ceramics layer of MLA. In this project they were adjusted to make the ceramics layer thickness  $\sim 100 \mu\text{m}$ .

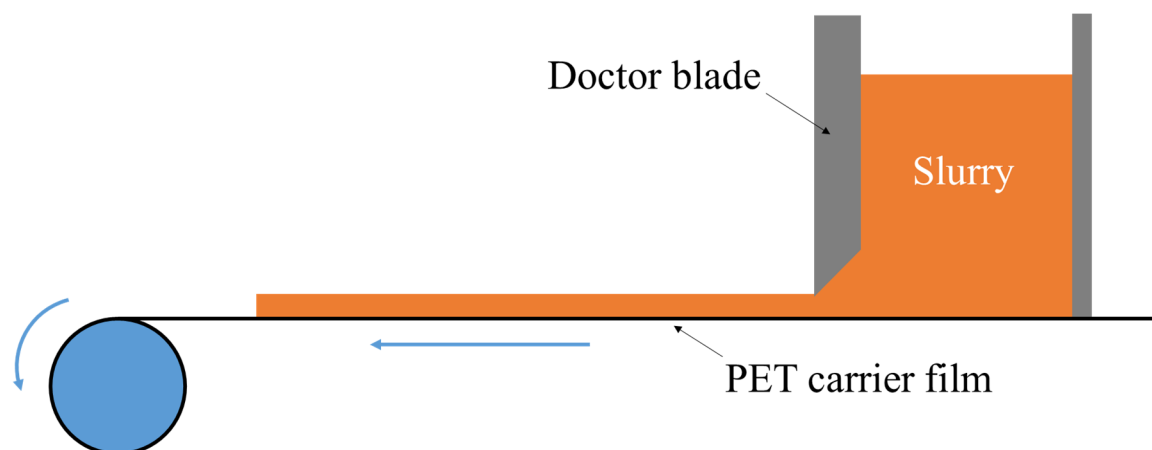


Fig. 8. 3 Schematic illustration of tape casting process.

### 8.2.3. Electrode printing

Forming electrodes on the green sheet was conducted using screen printing. A schematic diagram of the screen print process is shown in Fig. 8.4.<sup>133</sup> Electrode ink is squeezed through a mesh with permeable areas of defined geometry onto the green sheet. In this project, platinum ink (M637C, Heraeus) and a DEK 247 (DEK) screen printer were used. The area of the electrode is rectangular of  $9.2 \text{ mm} \times 7.2 \text{ mm}$ .

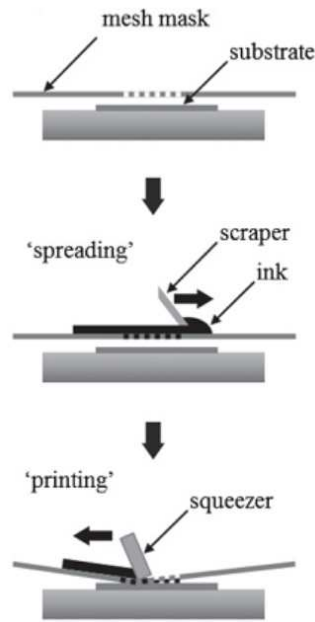


Fig. 8. 4 Schematic diagram of the screen-printing process.

### 8.2.4 Cutting and lamination

The green sheet with Pt electrode is separated into the square sheet of 30 mm × 30 mm including 4 areas of electrode using a sharp knife and peeled off the PET carrier film shown in Figure 8.5 (a). The peeled square sheets are adhered layer by layer as shown in Fig. 8.5 (b). In this project, 6 layers in total were adhered with 5 buffer layers both on top and bottom, which means that 5 ceramics layers are sandwiched by Pt electrodes in the MLA component. The adhered green sheets with electrodes were pressed at 10 MPa at 70°C for 20 min in a uniaxial press for lamination.

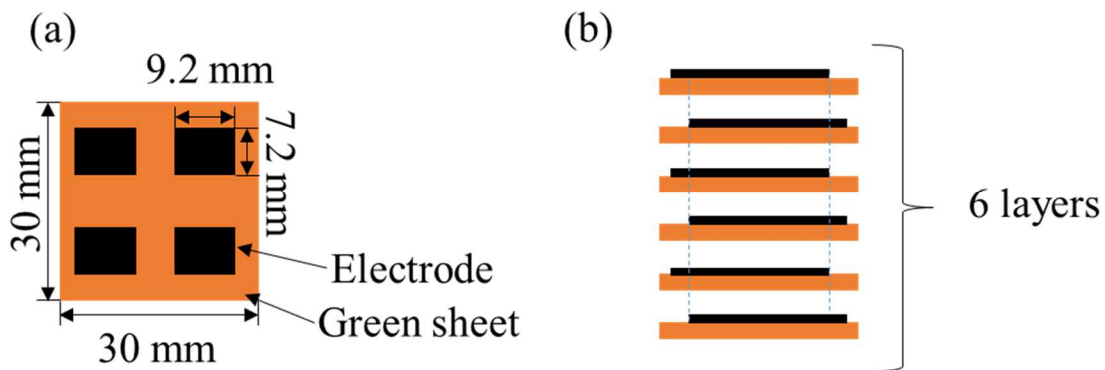


Fig. 8. 5 (a) a piece of green sheet with electrodes (30 mm × 30 mm) and (b) the schematic illustration of 6 stuck green sheets with electrode.

### 8.2.5 Binder burning out and sintering

Careful burn out the organic ingredients such as binder, solvent, dispersant, and plasticizer is required before sintering because they can cause pores or cracks in ceramics during the sintering process. Since the boiling temperature of ethyl methyl ketone is 80°C and the decomposition temperature of poly(propylene carbonate) is 250°C, binder burn out was conducted at 150°C and 300°C for 3h with a heating rate 1°C/min. Sintering temperature (1005 °C) was adjusted by deploying monolithic ceramics made from pieces of the laminated green sheet.

### 8.2.6 Termination of electrodes

By carefully grinding the sides of the MLA the electrodes are exposed. Silver paste (fired 2h at 500 °C) at was coated on the side and the top (or tail) of the MLA to terminate the electrodes, as illustrated in Fig. 8.6.

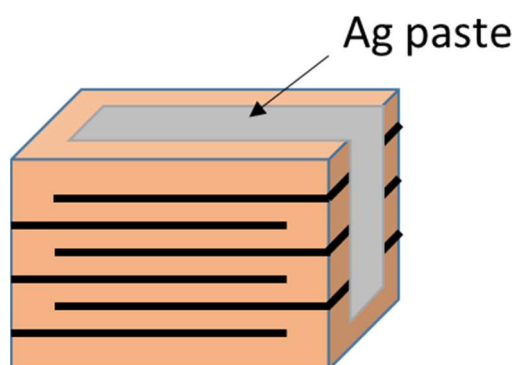


Fig. 8. 6 Schematic cross section of MLA.

## 8.3 Results and Discussion

To determine the appropriate ceramic thickness for the MLA, three kinds of MLA with different ceramic layer was fabricated and the bipolar SE curve and PE hysteresis loop were measured as shown in Fig. 8.7. The thinner the ceramic thickness, the smaller the strain measured. This tendency was previously reported by some researchers.<sup>134, 135</sup> Laurent mentioned it was attributed to the residual stress in ceramics due to mismatch between the electrodes and the ceramics. In this project, the ceramic thickness was optimized ~120 μm and the following assessments were carried out.

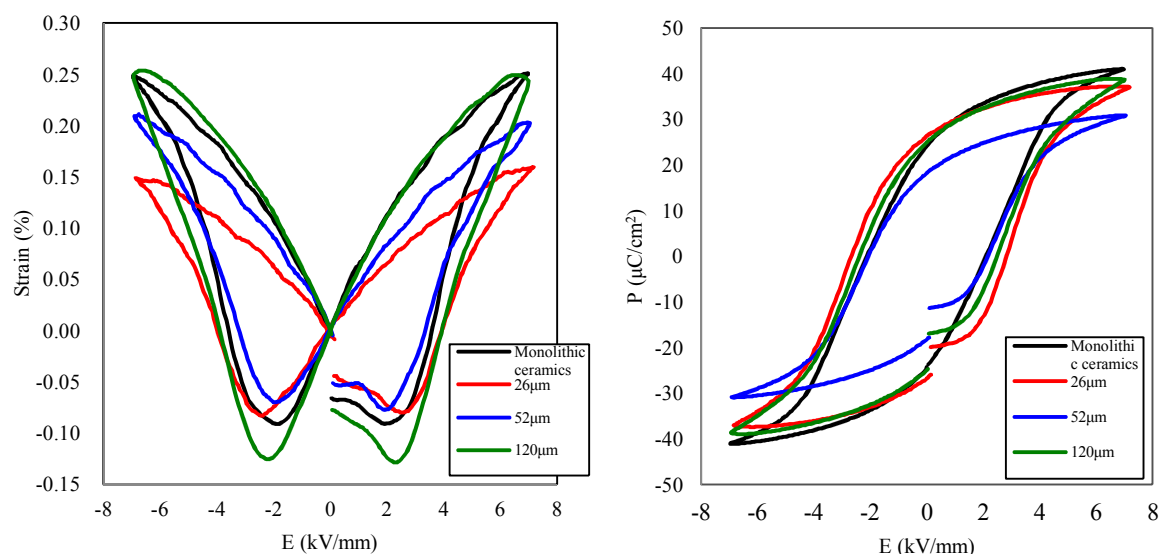


Fig. 8. 7 Ceramic thickness dependence of (a) SE curve and (b) PE hysteresis loop for the MLA.

Fig. 8.8 (a) and (b) show a scanning electron microscope image (SEM) of a cross section of the MLA and enlarged SEM image of the ceramics of the MLA. The thickness of each ceramic layer was  $\sim 120 \mu\text{m}$  and the active area of each electrode was  $34.34 \text{ mm}^2$ . No delamination or voids were observed and the grains are homogeneous. Fig. 8.9 shows frequency dependence of relative permittivity and  $\tan\delta$  vs temperature for the MLA. Compared to the monolithic ceramics, the  $\epsilon_r$  shifts to lower temperature by about  $30^\circ\text{C}$  and the onset temperature where  $\tan\delta$  increases also shifts to lower temperature. The dielectric anomaly shifts to lower temperature from  $100 \text{ kHz}$  to  $250 \text{ kHz}$ , consistent with monolithic ceramics where the dielectric anomaly displaces to lower temperature from  $10 \text{ kHz}$  to  $100 \text{ kHz}$  (Fig. 6.8). PE hysteresis loop and bipolar SE curve for a MLA measured at room temperature are shown in Fig 8.10 (a) and (b). The MLA gave a displacement of  $\sim 1.5 \mu\text{m}$  at  $882\text{V}$  ( $7 \text{ kV/mm}$ ) with a similar % strain to bulk compositions. The maximum polarization was  $38 \mu\text{C/cm}^2$ , slightly smaller than that of the bulk ceramics ( $41 \mu\text{C/cm}^2$ ). The *SE* and *PE* hysteresis loops are however a little wider in MLAs than in bulk ceramics, perhaps suggesting some influence of clamping from the presence of the internal Pt electrodes. Fig. 8.11 (a) and (b) show the temperature dependence of unipolar SE curve and PE loop for the MLA measured under an electric field of  $6 \text{ kV/mm}$  from  $25$  to  $150^\circ\text{C}$ . The temperature reliability of the MLA is lower than that of the monolithic ceramics, which is

supported by the results of temperature dependence of relative permittivity and  $\tan\delta$  (Fig. 8.9). The strain increases from a displacement of  $1.5\ \mu\text{m}$  to  $>3\ \mu\text{m}$  from room temperature to  $150^\circ\text{C}$ . Although strain increases in bulk ceramics with increase in temperature, the magnitude is significantly less (only 20% increase in bulk). The origin of this difference in the temperature dependence of strain between bulk and MLA remains to be elucidated but is likely to relate to un-pinning/clamping of domain walls as temperature increases.

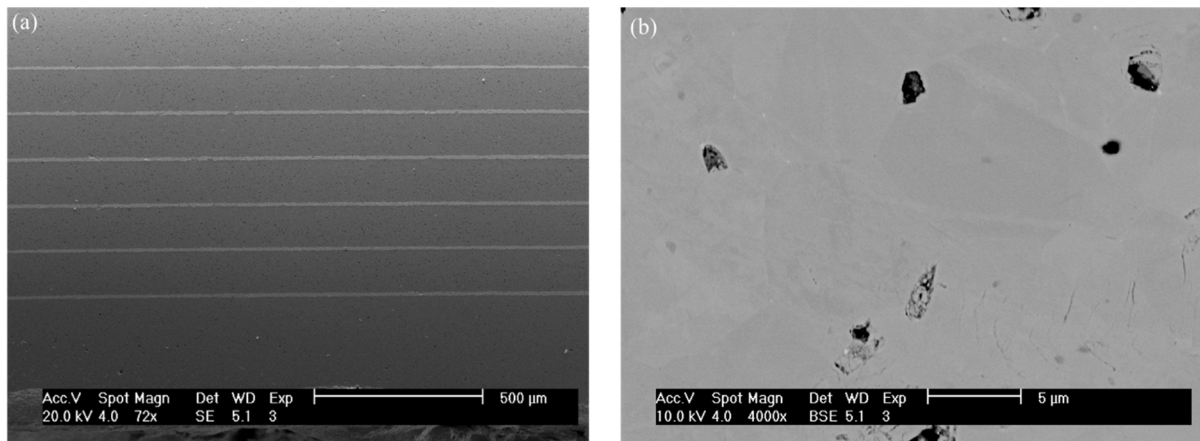


Fig. 8. 8 Cross-section image of SEM with (a) low magnification and (b) high magnification for the MLA.

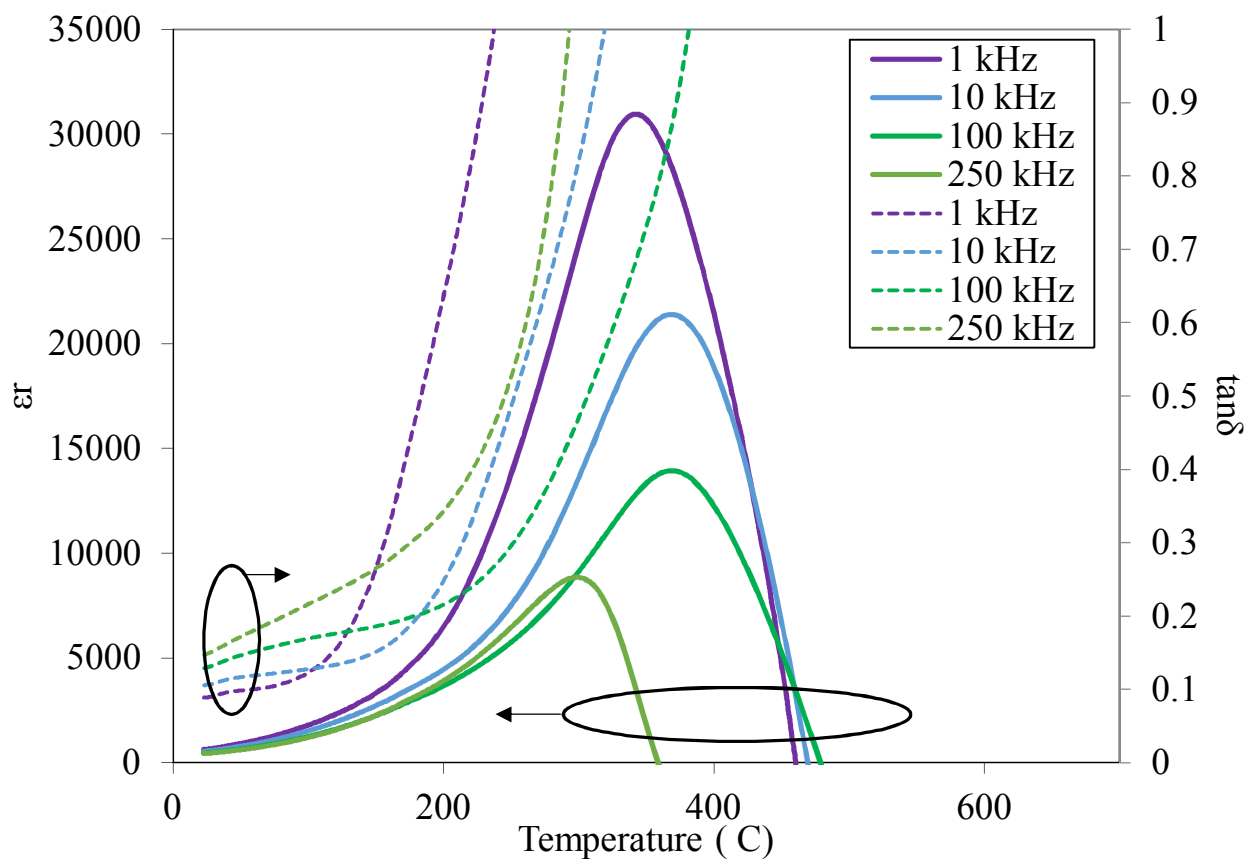


Fig. 8. 9 Temperature dependence of (a) relative permittivity and (b) dielectric loss,  $\tan\delta$  for the MLA.

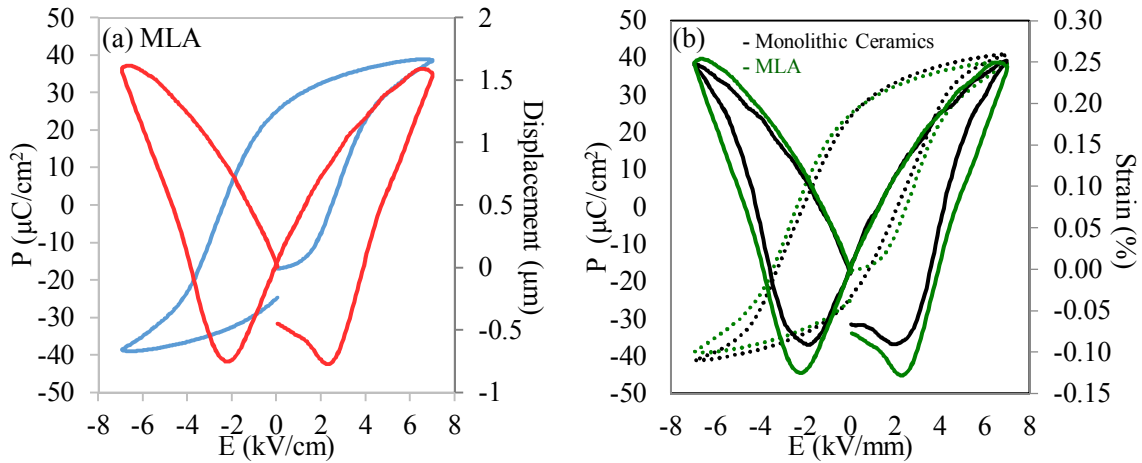


Fig. 8. 10 PE hysteresis loop and bipolar SE curve for (a) the MLA and (b) monolithic ceramics and the MLA.

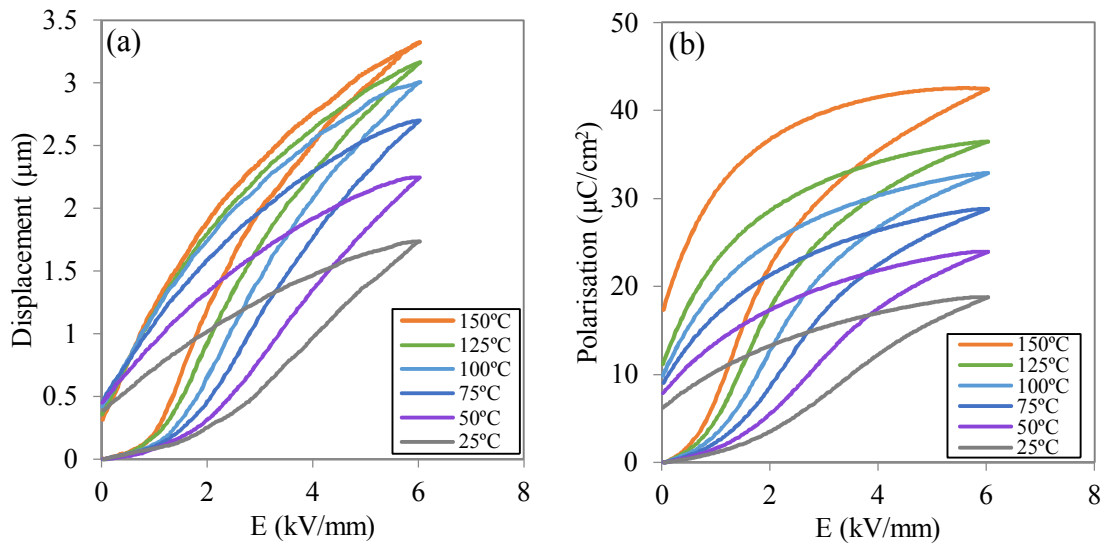


Fig. 8.11 Temperature dependence of (a) unipolar strain and (b) polarisation vs electric field for the MLA.

## 8.4 Conclusions

0.05BMN-0.32BT-0.63BF composition were successfully fabricated into MLAs with no voids or delamination. The microstructure of the grains were homogeneous and similar to monolithic ceramics. The strain and the polarization as a function of electric field are almost the same as monolithic ceramics but the curve has rounded shape, perhaps due to a greater leakage current or due to clamping from the presence of the internal Pt electrode. The frequency dependence of relative permittivity vs temperature shows the same tendency as monolithic

ceramics where the dielectric anomaly did not shift to higher frequency from 10 kHz to 100 kHz which requires further study. The strain increased as temperature increased more than that of the monolithic ceramics perhaps due to an increased leakage current.

## Chapter 9: Conclusions and Future work

### 9.1 Conclusions

The relationship between piezoelectric/dielectric/electric properties and structure/microstructure in BT-BF based ceramics was systematically investigated to develop lead-free piezoelectric materials with high piezoelectric properties and high temperature reliability.

#### 9.1.1 Optimising properties in $\text{BiMeO}_3$ doped lead-free $\text{BaTiO}_3$ - $\text{BiFeO}_3$ based ceramics.

The relationship between piezoelectric/ferroelectric properties and phase assemblage in  $0.05\text{Bi}(\text{Me})\text{O}_3$ - $(0.95-x)\text{BaTiO}_3$ - $(x)\text{BiFeO}_3$  ( $\text{Me} = \text{Y}, \text{Sc}_{1/2}\text{Y}_{1/2}, \text{Mg}_{2/3}\text{Nb}_{1/3}, \text{Sc}, \text{Zn}_{2/3}\text{Nb}_{1/3}, \text{Zn}_{1/2}\text{Ti}_{1/2}, \text{Ga}, \text{Al}, x = 0.70$ ) was investigated as a function of  $e_n$  and  $t$ . Only  $\text{Mg}_{2/3}\text{Nb}_{1/3}$  and  $\text{Sc}$  resulted in uniform ceramics of BT-BF system. Other dopants gave rise either secondary phases or core-shell structure in the ceramics.

#### 9.1.2 $0.05\text{Bi}(\text{Mg}_{2/3}\text{Nb}_{1/3})\text{O}_3$ - $(0.95-x)\text{BaTiO}_3$ - $(x)\text{BiFeO}_3$ based ceramics.

The relationship between the piezoelectric/electrostrictive properties, the structure and microstructure for  $0.05\text{Bi}(\text{Mg}_{2/3}\text{Nb}_{1/3})\text{O}_3$ - $(0.95-x)\text{BaTiO}_3$ - $(x)\text{BiFeO}_3$  ( $x = 0.55, 0.60, 0.63, 0.65, 0.70, \text{ and } 0.75$ ) ceramics was investigated. For  $x < 0.75$ , the microstructure inside the grains was homogeneous except for  $x = 0.75$  in which there was a core-shell structure which could be limited by quenching from the sintering temperature into liquid  $\text{N}_2$ . Piezoelectric properties, PE hysteresis loop and bipolar SE curve showed that BMN-BT-BF system changed from relaxor-like to ferroelectric-like behavior as  $x$  increased, consistent with the temperature dependence of relative permittivity, and TEM images in which only polar nano-regions were observed for  $x = 0.63$  and with macrodomains in  $x = 0.70$ . The highest strain was achieved at  $x = 0.63$  at the point of crossover from relaxor to ferroelectric behavior. For  $x = 0.63$ , the unipolar strain was gained 0.30% at 175°C and the variation of strain between room temperature and 175°C was 25%, competitive with PZT.

### **9.1.3 0.05BiScO<sub>3</sub>-(0.95-x)BaTiO<sub>3</sub>-(x)BiFeO<sub>3</sub> based ceramics.**

The relationship between the piezoelectric/electrostrictive properties, the structure and microstructure for 0.05BiScO<sub>3</sub>-(0.95-x)BaTiO<sub>3</sub>-(x)BiFeO<sub>3</sub> ( $x = 0.55, 0.60, 0.625, 0.65, 0.70,$  and  $0.75$ ) ceramics was investigated. Like Mg<sub>2/3</sub>Nb<sub>1/3</sub>, Sc-doped BT-BF systems showed the change from relaxor-like to ferroelectric behaviors in PE hysteresis loop, bipolar SE curve, temperature dependence of relative permittivity as  $x$  increases. The highest  $d_{33}^*$  was 465 pm/V for  $x = 0.625$ , similar to Mg<sub>2/3</sub>Nb<sub>1/3</sub>-doped BT-BF. IS measurements illustrated that optimised Sc-doped BT-BF ceramics were also electrically homogeneous, as with Mg<sub>2/3</sub>Nb<sub>1/3</sub>-doped BT-BF.

### **9.1.4 Multilayer actuator (MLA) for 0.05Bi(Mg<sub>2/3</sub>Nb<sub>1/3</sub>)O<sub>3</sub>-0.63BaTiO<sub>3</sub>-0.32BiFeO<sub>3</sub>.**

The fabrication of an MLA for 0.05Bi(Mg<sub>2/3</sub>Nb<sub>1/3</sub>)O<sub>3</sub>-0.63BaTiO<sub>3</sub>-0.32BiFeO<sub>3</sub> was successfully conducted with no void or delamination. The microstructure of the grains observed by BSE was homogeneous, resulting in high strain similar to monolithic ceramics. However, the bipolar SE curve implies that the ceramics were a leaky and the unipolar strain increased at high temperature more than that of the monolithic ceramics.

## **9.2 Future work**

One major aim of this project acquiring lead-free piezoelectric ceramics with high piezoelectric properties and high temperature reliability was achieved by 0.05Bi(Mg<sub>2/3</sub>Nb<sub>1/3</sub>)O<sub>3</sub>-0.32BT-0.63BF ceramics showing strain 0.41% at room temperature and 0.30% at 175°C. Moreover, a crystallochemical principle was demonstrated to optimize dopant types. However, there are some challenges left due to limited time of the PhD. They are classified into the following three aspects: i) fundamental investigations; ii) improving piezoelectric properties and iii) improving the MLA process.

### **i) Fundamental Investigations**

The first fundamental issue concerns conduction pathways in the ceramics. The complex IS measurements revealed that there are several contributions to the total conductivity of the ceramics but the precise number and kinds of the conduction paths remain speculative because the entire spectrum of  $M''$  as a function of frequency was not acquired between low and high temperature.

The second fundamental issue concerns the nature of the field-induced transition. It was concluded that high strain for  $0.05\text{Bi}(\text{Mg}_{2/3}\text{Nb}_{1/3})\text{O}_3\text{-}0.32\text{BT}\text{-}0.63\text{BF}$  originated from field-induced transition at the point of cross over from relaxor to ferroelectric associated with a transition from nano to macro-domain structure. This conclusion is supported by several data sets such as the temperature dependence of relative permittivity, PE hysteresis loop, bipolar SE curve, crystal structure from XRD refinement, and domain structure from TEM images. The nature of the induced transition warrants further investigation, potentially using in-situ X-ray as a function of field and temperature.

The third relates to the chemical bonding between cations and oxygen. In this project, several relationships between structure/microstructure and piezoelectric/dielectric properties, were revealed but information relating to  $V_{\text{O}}$  and O site structure was not determined. To improve the knowledge of the origin of the high strain, it is necessary to understand the role of  $V_{\text{O}}$  and possibly to determine local distortions of the O-octahedral network using neutron diffraction.

### **ii) Improving the Piezoelectric Response**

Although a high strain of 0.41% was achieved in this project,  $d_{33}$  was considerably lower (146 pC/N) than  $d_{33}$  that of quenched Ga-doped BT-BF ceramics reported to have 402 pC/N. This value is not likely to be high enough to compete commercially in the sensor market. The key factor is thought of to be the crystal structure which the above authors claim is an MPB between rhombohedral and tetragonal phases. However, we repeatedly observed combinations of rhombohedral and pseudocubic, albeit with higher dopant concentrations. Further studies are thus encouraged, particularly building on the crystallochemical principles defined in this thesis.

### **iii) Improving the MLA Process**

In this project, MLA was successfully fabricated using Pt inner electrodes but Pt is an expensive material and the ceramics showed an increase in leakage current. Therefore, to progress this material to industrial use, it is important to optimize the process using the cheaper inner electrodes such as Ag, Cu, and Ni.

## References

- [1] T. Stevenson, D. G. Martin, P. I. Cowin, A. Blumfield, A. J. Bell, T. P. Comyn, and P. M. Weaver, *J. Mater. Sci. Mater. Electron*, **26**, 9256-9267 (2015).
- [2] R. Müller-Fielder and V. Knoblauch, *Microelectron. Reliab*, **43**, 1085-1097 (2003).
- [3] An Introduction to Piezoelectric Materials and Applications, J. Holterman & P. Groen.
- [4] R. A. Goyer, *Environ Health Perspect*, **100**, 177-187 (1993).
- [5] G. Lockitch, *Clin Biochem*, **26**, 371-381 (1993).
- [6] J. Rödel, K. G. Webber, R. Dittmer, W. Jo, M. Kimura, and D. Damjanovic, *J Eur Ceram Soc*, **35**, 1659-1681 (2015).
- [7] A. Takahashi, *Nippon Gomu Kyokaishi*, **48**, 537-557 (1975).
- [8] Canadian Centre for Occupational Health and Safety. *Material and safety data sheet on lead oxide*, (1995).
- [9] K.H. Härdtl, H. Rau, *SolidState Commun*, **7**, 41-45(1969).
- [10] "DIRECTIVE 2002/95/EC OF THE EUROPEAN PARLIAMENT AND OF THE COUNCIL", *Official Journal of the European Union*, L37/19, (2003).
- [11] Y. Saito, H. Takano, T. Tani, T. Nonoyama, K. Takatori, T. Homma, T. Nagaya, and M. Nakamura, *Nature*, **432**, 84-87 (2004).
- [12] E. K. Akdogan, K. Kerman, M. Abazari, and A. Safari, *Appl. Phys. Lett.*, **92**, 112908 (2008).
- [13] E. Hollenstein, D. Damjanovic, N. Setter, *J. Eur. Ceram. Soc.*, **27**, 4093-4097 (2007).
- [14] R. Wang, K. Wang, F. Yao, J. Li, F. H. Schader, K. G. Webber, W. Jo, and J. Rödel, *J. Am. Ceram. Soc.*, **98** [7], 2177-2182 (2015).
- [15] S. Zhang, A. B. Kounga, E. Aulbach, T. Granzow, W. Jo, , H. Kleebe, and J. Rödel, *J. Appl. Phys.*, **103**, 034107 (2008).
- [16] W. Liu and X. Ren, *Phys. Rev. Lett.*, **103**, 257602 (2009).
- [17] M. H. Lee, D. J. Kim, J. S. Park, S. W. Kim, T. K. Song, M. Kim, W. Kim, D. Do, and I. Jeong, *Adv. Mater.*, **27**, 6976-6982 (2015).
- [18] M. M. Kumar, A. Srinivas, and S. V. Suryanarayana, *J. Appl. Phys.*, **87**, 855-862 (2000).

- [19] R. A. M. Gotardo, D. S. F. Viana, M. Olzon-Dionysio, S.D. Souza, D. Garcia, J. A. Eiras, M. F. S. Alves, L. F. Cótica, I. A. Santos, and A. A. Coelho, *J. Appl. Phys.*, **112**, 104112 (2012).
- [20] J. Chen, J. Chen, *J. Alloys and Compounds*, **589**, 115-119 (2014).
- [21] C. Zhou, A. Feteira, X. Shan, H. Yang, Q. Zhou, J. Cheng, W. Li, H. Wang, *Appl. Phys. Lett.*, **101**, 032901 (2012).
- [22] S. O. Leontsev and R. E. Eitel, *J. Am. Ceram. Soc.*, **92**, 2957-2961 (2009).
- [23] Y. Wei, X. Wang, J. Zhu, X. Wang, and J. Jia, *J. Am. Ceram. Soc.*, **96** [10], 3163-3168 (2013).
- [24] L. Cao, C. Zhou, J. Xu, Q. Li, C. Yuan, and G. Chen, *Phys. Status Solidi A* **213**, No. 1, 52-59 (2016).
- [25] A. Singh, A. Senyshyn, H. Fuess, S.e J. Kennedy, and D. Pandey, *Phys. Rev. B*, **89**, 024108 (2014).
- [26] H. Yabuta, M. Shimada, T. Watanabe, J. Hayashi, M. Kubota, K. Miura, T. Fukui, and S. Wada, *Jpn. J. Appl. Phys.*, **51**, 09LD04 (2012).
- [27] A.J. Moulson and J.M. Herbert, “Electroceramics second edition”, (2003).
- [28] J. Holterman and P. Groen, *An Introduction to Piezoelectric Materials and Applications*. Sticking Applied Piezo, (2013).
- [29] K. C. Kao, *Dielectric Phenomenon in Solids*. Elsevier Academic Press, (2004).
- [30] A. Safari and E. K. Akdogan, *Piezoelectric and acoustic materials for transducer*, Springer US, (2009).
- [31] G. H. Haertling, *J. Am. Ceram. Soc.*, **82**, 797, (1999).
- [32] V. M. Goldschmidt, *Naturwissenschaften*, **14**, no. 21, 477–485, (1926).
- [33] H. D. Megaw, *Crystal Structures: A Working Approach*, **10**. W. B. Saunders, (1973).
- [34] S.J. Kuang, X.G. Tang, L.Y. Li, T.P. Jiang, and Q.X. Liu, *Scripta Materialia*, **61**, 68-71, (2009).
- [35] C. A. Randall, A. S. Bhalla, T. R. ShROUT, and L. E. Cross, *J. Mater. Res.*, **5**, no. 4, 829–834, (1990).
- [36] A. Glazer, *Acta Crystallogr. Sect. B*, **28**, no. 11, 3384–3392, (1972).
- [37] I. M. Reaney, E. L. Colla, and N. Setter, *Jpn J. Appl. Phys.*, **33**, 3984-3990, (1994).

- [38] D. I. Woodward and I. M. Reaney, *Acta Crystallographica Section B*, **61**, Part 4, 387-399, (2005).
- [39] T. R. Shrout and A. Halliyal, *Am. Ceram. Soc. Bull.*, **66**, 704, (1987).
- [40] Z. C. Li and B. Bergman, *J. Eur. Ceram. Soc.*, **25**, 441-445, (2005).
- [41] B. Jaffe, W. R. Cook Jr., and H. Jaffe, “*Piezoelectric ceramic*”, Academic Press London and New York, (1971).
- [42] D. Damjanovic, *Reports Prog. Phys.*, **61**, no. 9, 1267 (1998).
- [43] G. A. Smolenskii and A. I. Agranovskaya *Sov. Physics-Solid State*, **1**, no. 10, 1429–1437, (1959).
- [44] G. A. Smolenskii, *J. Phys. Soc. Jpn*, **28**, 26-37, (1970).
- [45] Gene H. Haertling, *J. Am. Ceram. Soc.*, **82**, [4], 797–818, (1999).
- [46] L. E. Cross, *Piezoelectricity*. Springer Berlin Heidelberg, 2008.
- [47] G. A. Smolenskii and A. I. Agranovskaya, *Sov. Phys. Tech. Phys.* **3**, 1380 (1958).
- [48] V. V. Kirillov and V. A. Isupov, *Ferroelectrics* **5**, 3 (1973).
- [49] D. Viehland, S. J. Jang, L. E. Cross and M. Wuttig, *J. Appl. Phys.* **68**, 2916 (1990).
- [50] V. Westphal, W. Kleemann and M. Glinchuk, *Phys. Rev. Lett.*, **68**, 847 (1992).
- [51] M. A. Akbas and P. K. Davies, *J. Am. Ceram. Soc.*, **80**, 2933 (1997).
- [52] Z-Y. Cheng, R. S. Katiyar, X. Yao and A. Guo, *Phys. Rev. B*, **55**, 8165 (1997).
- [53] R. Pirc and R. Blinc, *Phys. Rev. B*, **60**, 13470 (1999).
- [54] G. Shirane, K. Suzuki, and A. Takeda, *J. Phys. Soc. Jpn.*, **7**, No. 1, 12-18, (1952).
- [55] E. Sawaguchi, *J. Phys. Soc. Jpn.*, **8**, No. 5, 12, 615-629, (1952).
- [56] T. R. Shrout, S. J. Zhang, *J. Electroceram.*, **19**, 111-124, (2007).
- [57] B. Jaffe, R. S. Roth, and S. Marzullo, *Journal of Applied Physics*, **25**, 809-810 (1954).
- [58] B. Noheda, J. A. Gonzalo, L. E. Cross, R. Guo, S.-E. Park, D. E. Cox, and G. Shirane, *Phys. Rev. B*, **61**, 8695 (2000).
- [59] W. J. Merz, *Phys. Rev.*, **76**, 1221, (1949).
- [60] Dragan Damjanovic, *Appl. Phys. Lett.* **97**, 062906, (2010).
- [61] J. Curie and P. Curie, *Bulletin de la Société minérologique de France*. **3**, 90–93. (1880).  
Reprinted in: J. Curie and P. Curie, *Comptes rendus (in French)*. **91**, 294–295, (1880).
- [62] G. Lippmann, *Annales de chimie et de physique (in French)*, **24**, 145 (1881).

- [63] J. Curie and P. Curie. *Comptes rendus (in French)*. **93**, 1137–1140 (1881).
- [64] D. Wang, Y. Fotinich, G.P. Carman, *J. Appl. Phys.* **83**, 5342–5350 (1998).
- [65] A. B. Schäufele, K. H. Härdtl, *J. Am. Ceram. Soc.*, **79**, [10], 2637-2640 (1996).
- [66] <http://eur-lex.europa.eu/LexUriServ/LexUriServ.do?uri=OJ:L:2003:037:0019:0023:EN:PDF>, ”DIRECTIVE 2002/95/EC OF THE EUROPEAN PARLIAMENT AND OF THE COUNCIL of 27 January 2003 on the restriction of the use of certain hazardous substances in electrical and electronic equipment”, visited on 22th of February 2018.
- [67] Y. Saito, H. Takano, T. Tani, T. Nonoyama, K. Takatori, T. Homma, T. Nagaya, and M. Nakamura, Lead-free piezoceramics, *Nature*, **432**, 84-87 (2004).
- [68] E. K. Akdogan, K. Kerman, M. Abazari, and A. Safari, *Appl. Phys. Lett.*, **92**, 112908 (2008).
- [69] E. Hollenstein, D. Damjanovic, N. Setter, *J. Eur. Ceram. Soc.*, **27**, 4093-4097 (2007).
- [70] H. Shi, J. Chen, R. Wang, S. Dong, *J. Alloys and Compounds*, **655**, 290-295 (2016).
- [71] S. Liu, A. B. Kounga, E. Aulbach, H. Ehrenberg, and J. Rödel, *Appl. Phys. Lett.*, **91**, 11, 112906 (2007).
- [72] X. Liu and X. Tan, *J. Appl. Phys.*, **120**, 034102 (2016).
- [73] L. Li, J. Hao, Z. Xu, W. Li, R. Chu, G. Li, *Ceramics International*, **42**, 14886-14893 (2016).
- [74] W. Liu and X. Ren, *Phys. Rev. Lett.*, **103**, 257602 (2009).
- [75] L. Cao, C. Zhou, J. Xu, Q. Li, C. Yuan, and G. Chen, *Phys. Status Solidi A* **213**, No. 1, 52-59 (2016).
- [76] W. Zhou, Q. Zheng, Y. Li, Q. Li, Y. Wan, M. Wu, and D. Lin, *Phys. Status Solidi A* **212**, No. 3, 632-639 (2015).
- [77] Y. Wan, Y. Li, Q. Li, W. Zhou, Q. Zheng, X. Wu, C. Xu, B. Zhu, and D. Lin, *J. Am. Ceram. Soc.*, **97** [6], 1809-1818 (2014).
- [78] C. Zhou, Z. Cen, H. Yang, Q. Zhou, W. Li, C. Yuan, H. Wang, *Physica B*, **410**, 13-16 (2013).
- [79] X. Liu, Z. Xu, X. Wei, and X. Yao, *J. Am. Ceram. Soc.*, **91** [11], 3731-3734 (2008).
- [80] X. Liu, Z. Xu, S. Qu, X. Wei, J. Chen, *Ceram. International*, **34**, 797-801 (2008)

- [81] Q. Zhou, C. Zhou, H. Yang, G. Chen, W. Li, and H. Wang, *J. Am. Ceram. Soc.*, **95** [12], 3889-3893 (2012).
- [82] Q. Zheng, Y. Guo, F. Le, X. Wu, D. Lin, *J. Mater. Sci.: Mater Electron*, **25**, 2638-2648 (2014).
- [83] Z. Cen, C. Zhou, H. Yang, Q. Zhou, W. Li, C. Yan, L. Cao, J. Song, and L. Peng, *J. Am. Ceram. Soc.*, **96** [7], 2252-2256 (2013).
- [84] T. Zheng, Z. Jiang and J. Wu, *Dalton Trans.*, **45**, 11277 (2016).
- [85] Q. Zheng, , L. Luo, K. H. Lam, N. Jiang, Y. Guo, and D. Lin, *J. Appl. Phys.*, **116**, 184101 (2014).
- [86] D. Wang, A. Khesro, S. Murakami, A. Feteira, Q. Zhao, I. M. Reaney, *Journal of the European Ceramic Society*, **37**, 1857–1860 (2017).
- [87] X. Wu, M. Tian, T. Guo, Q. Zheng, L. Luo, D. Lin, *J. Mater. Sci.: Mater. Electron*, **26**, 978-984 (2015).
- [88] R. Rai, I. Bdikin, M. A. Valente, A. L. Kholkin, *Mater. Chem. and Phys.*, **119**, 539-545 (2010).
- [89] D. Wang, M. Wang, F. Liu, Y. Cui, Q. Zhao, H. Sun, H. Jin, M. Cao, *Ceramics International*, **41**, 8768-8772 (2015).
- [90] T. Zheng and J. Wu, *J. Mater. Chem. C*, **3**, 11326-11334 (2015).
- [91] D. Wang, Z. Fan, D. Zhou, A. Khesro, S. Murakami, A. Feteira, Q. Zhao, X. Tan, I. M. Reaney, (Submitted to *J. Am. Ceram. Soc.*)
- [92] L. Luo, N. Jiang, X. Zou, D. Shi, T. Sun, Q. Zheng, C. Xu, K. H. Lam, and D. Lin, *Phys. Status Solidi A*, **212**, No. 9, 2012-2022 (2015).
- [93] E. K. Akdogan, K. Kerman, M. Abazari, and A. Safari, *Appl. Phys. Lett.*, **92**, 112908 (2008).
- [94] T. Wang, L. Jin, Y. Tian, L. Shu, Q. Hu, X. Wei, *Materials Lett.*, **137**, 79-81 (2014).
- [95] Y. Jun, W. Moon, C. Chang, H. Kim, H. S. Ryu, J. W. Kim, K. H. Kim, S. Hong, *Solid State Commun.*, **135**, 133-137 (2005).
- [96] M.S. Wu, Z.B. Huang, C.X. Han, S.L. Yuan, C.L. Lu, S.C. Xia, *Solid State Commun.*, **152**, 2142-2146 (2012).
- [97] Z. Yao, C. Xu, H. Hao, Q. Xu, W. Hu, M. Cao, and H. Liu, *Int. J. Appl. Ceram. Technol.*,

- 13** [3], 549-553 (2016).
- [98] Y. Guo, P. Xiao, R. Wen, Y. Wan, Q. Zheng, D. Shi, K. H. Lam, M. Liu and D. Lin, *J. Mater. Chem.*, **3** 5811-5824 (2015).
- [99] W. Zhou, Q. Zheng, Y. Li, Q. Li, Y. Wan, M. Wu, and D. Lin, *Phys. Status Solid A*, **212**, 632-639 (2015).
- [100] I. Fujii, R. Mitsui, K. Nakashima, N. Kumada, M. Shimada, T. Watanabe, J. Hayashi, H. Yabuta, M. Kubota, T. Fukui, and S. Wada, *Jpn. J. Appl. Phys.*, **50**, 09ND07 (2011).
- [101] X. Shan, C. Zhou, Z. Cen, H. Yang, Q. Zhou, Weizhou Li, *Ceramics International*, **39**, 6707-6712 (2013).
- [102] L. Zhu, B. Zhang, S. Li, L. Zhao, N. Wang, X. Shi, *J. Alloys and Compounds*, **664**, 602-608 (2016).
- [103] Q. Zhou, C. Zhou, H. Yang, G. Chen, W. Li, and H. Wang, *J. Am. Ceram. Soc.*, **95**, 3889-3893 (2012).
- [104] <https://www.malvern.com/en/products/product-range/mastersizer-range/mastersizer-3000>, “Mastersizer 3000”, visited on 22th of February 2018.
- [105] R. A. Young, “The Rietveld Method”, Oxford University Press, 1993.
- [106] P. J. Goodhew, J. Humphreys, R. Beanland, ” *Electron Microscopy and Analysis, Third Edition*”, Crc Press, 2000.
- [107] J. Goldstein and D. E. Newbury, “*Scanning electron microscopy and x-ray microanalysis: Third Edition*”, New York: Plenum Press, 2007.
- [108] An American and National Standard, “*An American National Standard IEEE standard on piezoelectricity*,” 176, 1987.
- [109] M. Stewart, M. G. Cain, and D. Hall, *NPL Rep. C.*, no. May, pp. 1–57, 1999.
- [110] D. C. Sinclair and A. R. West, *J. Appl. Phys.* **66**, 3850 (1989).
- [111] N. Zidi, A. Chaouchi, S. d’Astorg, M. Rguiti, C. Courtois, *Journal of Alloys and Compounds*, **590**, 557-564 (2014).
- [112] M. Li, M. J. Pietrowski, R. A. De Souza, H. Zhang, I. M. Reaney, S. N. Cook, J. A. Kilner and D. C. Sinclair, *Nat. Mater.*, 2014, **13**, 31.
- [113] M. Li, H. Zhang, S. N. Cook, L. Li, J. A. Kilner, I. M. Reaney, and D. C. Sinclair, *Chem. Mater.*, **27**, [2], 629–634, (2015).
- [114] J. S. Reed, “Principles of Ceramics Processing, 2nd Edition”.

- [115] H. Zhang, W. Jo, K. Wang, K. G. Webber, *Ceramics International*, **40**, 4759-4765, (2014).
- [116] S. Murakami, D. Wang, A. Mostaed, A. Khsro, D. C. Sinclair, I. M. Reaney, *J. Am. Ceram. Soc.* DOI: 10.1111/jace.15749, (2018).
- [117] E. A. Patterson, D. P. Cann, J. Pokorny, and I. M. Reaney, *J. Appl. Phys.*, **111**, 094105 (2012).
- [118] X. Liu, J. Zhai, B. Shen, F. Li, Y. Zhang, P. Li, B. Liu, *Journal of the European Ceramic Society*, **37**, 1437–1447 (2017).
- [119] A. Khesro, D. Wang, F. Hussain, D. C. Sinclair, A. Feteira, and I. M. Reaney, *Appl. Phys. Lett.*, **109**, 142907 (2016).
- [120] Y. Ehara, N. Novak, A. Ayrikyan, P. T. Geiger, and K. G. Webber, *J. Appl. Phys.*, **120**, 174103 (2016).
- [121] L. Li, J. Hao, R. Chu, Z. Xu, W. Li, J. Du, P. Fu, *Ceramics International*, **42**, 9419–9425 (2016).
- [122] W. Y. Pan, C. Q. Dam, Q. M. Zhang, and L. E. Cross, *J. Appl. Phys.*, **66**, 6014-6023 (1989).
- [123] M. Davis, D. Damjanovic, and Nava Setter, *J. Appl. Phys.*, **97**, 064101 (2005).
- [124] M. Davis, D. Damjanovic, and N. Setter, *Phys. Rev. B*, **73**, 014115 (2006).
- [125] A. Pramanick, D. Damjanovic, J. E. Daniels, J. C. Nino, and J. L. Jones, *J. Am. Ceram. Soc.*, **94**, [2], 293-309 (2011).
- [126] H. Ogihara, C. A. Randall, Susan Trolier-McKinstry, *J. Am. Ceram. Soc.*, **92** [1], 110-118, (2009).
- [127] X. Li, J. Zhu, M. Wang, Y. Luo, W. Shi, L. Li, J. Zhu, D. Xiao, *J. Alloys Compd.*, **499**, L1-L4, (2010).
- [128] R. E. Eitel, C. A. Randall, T. R. Shrout, P. W. Rehrig, *Jpn. J. Appl. Phys.*, **40**, 599-6002, (2001).
- [129] S. Zhang, X. Wang, H. Wang, L. Li, *J. Eur. Ceram. Soc.*, **34**, 2317-2323, (2014).
- [130] L. Gao, H. Guo, S. Zhang, and C. Randall, *Actuators*, **5**, [1], 8, (2016).
- [131] C. A. Randall, A. Kelnberger, G. Y. Yang, R. E. Eitel, and T. R. Shrout, *J. Electroceramics*, **14**, 177-191, (2005).

- [132] “<https://commons.wikimedia.org/wiki/File:MLCC-Manufacturing-Process.png>.” visited on 2nd of February 2018.
- [133] “[http://flow.kaist.ac.kr/bbs/board.php?bo\\_table=fluelcell&wr\\_id=29](http://flow.kaist.ac.kr/bbs/board.php?bo_table=fluelcell&wr_id=29).” visited on 2nd of February 2018.
- [134] M. Laurent, H. Bodinger, T. Steinkopff, *14th IEEE International Symposium on Applications of Ferroelectrics, 2004. ISAF-04*, 60-63, (2004).
- [135] W. A. Groen, K. Prijs, and S. Saeed, *Integrated Ferroelectrics*, **115**:132–141, 2010.
- [136] Handbook of Micromechanics and Nanomechanics 1st Edition, S. Li and X. Gao, Pan Stanford, Singapore, (2013).
- [137] A. Pramanick, D. Damjanovic, J. E. Daniels, J. C. Nino, and J. L. Jones, *J. Am. Ceram. Soc.*, **92**, 293-309, (2011).
- [138] G. W. Pabst, L. W. Martin, Y. Chu, and R. Ramesh, *Appl. Phys. Lett.*, **90**, 072902, (2006).
- [139] W. Li, J. Yang, Z. Wu, J. Wang, B. Li, S. Feng, Y. Deng, F. Zhang, and D. Zhao, *J. Am. Ceram. Soc.*, **134**, 11864-11867, (2012).